STUDIES OF YOUNG STELLAR OBJECTS AND THEIR ENVIRONMENT

A thesis submitted in partial fulfillment for the degree of
DOCTOR of PHILOSOPHY

in

The Faculty of Science
UNIVERSITY OF CALICUT

by

RUMPA CHOUDHURY

INDIAN INSTITUTE OF ASTROPHYSICS
Bangalore 560034, India
January, 2011

Declaration

I hereby declare that the matter contained in this thesis entitled "***Studies of Young Stellar Objects and their Environment***", is the result of the investigations carried out by myself, ***Rumpa Choudhury***, at Indian Institute of Astrophysics, Bangalore, under the guidance of ***Prof. H. C. Bhatt***. This thesis has not been submitted for the award of any degree, diploma, associateship, fellowship etc. of any university or institute.

Rumpa Choudhury   Prof. H. C. Bhatt

(Ph.D. Candidate)   **(Thesis Supervisor)**

Indian Institute of Astrophysics

Bangalore 560034, India

January, 2011

Certificate

This is to certify that the thesis entitled "***Studies of Young Stellar Objects and their Environment***" submitted to the University of Calicut by Ms. ***Rumpa Choudhury*** for the award of the degree of Doctor of Philosophy in the faculty of Science, is based on the results of the investigations carried out by her under my supervision and guidance, at Indian Institute of Astrophysics, Bangalore. This thesis has not been submitted for the award of any degree, diploma, associateship, fellowship etc. of any university or institute.

Prof. H. C. Bhatt

(Thesis Supervisor)

Indian Institute of Astrophysics

Bangalore 560034, India

January, 2011

Certificate

This is to certify that the following papers have been published by Ms. **_Rumpa Choudhury_** during the period of her research work.

- _Kinematics of the Young Stellar Objects associated with the Cometary Globules in the Gum Nebula_
  Choudhury, Rumpa., & Bhatt, H. C., 2009, MNRAS, 393, 959

- _Triggered star formation and Young Stellar Population in Bright-Rimmed Cloud SFO 38_
  Choudhury, Rumpa., Mookerjea, Bhaswati., & Bhatt, H. C., 2010, ApJ, 717, 1067

- _Variable circumstellar activity of V351 Orionis_
  Choudhury, Rumpa., Bhatt, H. C., Pandey, G., 2011, A&A, 526, A97

Monthly Notices of the Royal Astronomical Society (MNRAS), The Astrophysical Journal (ApJ) and Astronomy & Astrophysics (A&A) are peer reviewed/referred journals.

Prof. H. C. Bhatt
(Thesis Supervisor)

Indian Institute of Astrophysics
Bangalore 560034, India
January, 2011

"Hope is a good thing, maybe the best of things, and no good thing ever dies."

The Shawshank Redemption (1994)

Acknowledgments

This thesis arose, in part, out of years of research that I have done since I came to Indian Institute of Astrophysics, Bangalore. This thesis would not have been possible without the help and support of the kind people around me, to only some of whom it is possible to give particular mention here.

First and foremost, I owe my deepest gratitude to my supervisor, Prof. H. C. Bhatt, who has been a wonderful advisor with his great intuition on scientific problems. This thesis would not have come to the final stage without his support, useful advice and constructive feedback. I have learnt a lot from his guidance, which helped me to come up with new ideas, interesting scientific problems and most importantly to plan and carry out research by myself.

I would like to show my gratitude to the Director of Indian Institute of Astrophysics, Prof. S. S. Hasan for giving me the opportunity to work in this institute and providing all the support and facilities required for research work. I am grateful to all the faculty members of the Department of Physics, Calicut University, for their help and support to complete the required administrative procedures at College Development Council, Calicut University. I would like to thank the members of my doctoral committee, Prof. Chanda J. Jog, Prof. A. K. Pati, Prof. S. G. V. Mallik, Prof. M. V. Mekkaden, for useful comments, suggestions and insights which have been extremely useful for my research work. I am grateful to all the members of the Board of Graduate Studies for the help and support that have been provided throughout the course of my work. I would also like to thank all the staff members of Library and Administrative division of IIA for the required assistance in time at each steps during my fellowship period. I would also like to acknowledge the help and assistance of the staff members of the Vainu Bappu Observatory (VBO), Kavalur, Indian Astronomical Observatory (IAO), Hanle, and Centre For Research & Education in Science & Technology (CREST), Hoskote during the observations. My sincere thanks also go to Dr. A. Subramaniam and Dr. P. S. Parihar for the useful discussions which have been very helpful for this work.

This research work would not have been completed without the active involvement of a few people around me. Their help, support, inspiration and the time that they have spent for each of my *nitty-gritty* needs and thoughts, have guided me to be on the track during this journey. In this occasion, I want to convey my sincere regards to Dr. Maheshwar Gopinathan, Dr. Gajendra Pandey, and Dr. B. A. Varghese. I would also like to take this opportunity to express my warm regard and sincere thanks to Dr. Bhaswati Mookerjea, Tata Institute of Fundamental Research, Mumbai.

I wish to thank all of my friends at Siuri, Burdwan, Kharagpur, Bangalore and elsewhere for their support and encouragement throughout this work. Let me recall the splendid

memories of those always cheerful meetings with Ananta, Bharat, Girjesh, Ramya and Tapan, since the very beginning of this work.

Finally I would like to thank my sister, Reshmi and my friend, Ashutosh for that *Magic Box* that constantly provides a positive and optimistic attitude towards life. Thanks !

Last but not the least, I would like to mention about the pillar of my life: my parents Ms. Nilima Choudhury and Mr. Asoke Kumar Choudhury. I cannot dare to thank them for anything ! It will always remain the best fact of my life that I am so lucky to have the most wonderful parents in this world.

For any errors or inadequacies that may remain in this work, of course, the responsibility is entirely my own.

Rumpa Choudhury

Contents

Resources   **107**

Bibliography   **109**

List of Figures

List of Tables

List of Publications

Papers Published in Refereed Journals:

- *Kinematics of the Young Stellar Objects associated with the Cometary Globules in the Gum Nebula*
  Choudhury, Rumpa., & Bhatt, H. C., 2009, MNRAS, 393, 959

- *Triggered star formation and Young Stellar Population in Bright-Rimmed Cloud SFO 38*
  Choudhury, Rumpa., Mookerjea, Bhaswati., & Bhatt, H. C., 2010, ApJ, 717, 1067

- *Variable circumstellar activity of V351 Orionis*
  Choudhury, Rumpa., Bhatt, H. C., Pandey, G., 2011, A&A, 526, A97

Papers Published/Submitted in Conference Proceedings:

- *Star formation in the bright rimmed cloud SFO 38 in IC 1396*
  Choudhury, Rumpa., & Bhatt, H. C., 2009, XXVII Meeting of the Astronomical Society of India, submitted to Bulletin of Astronomical Society of India (BASI)

- *Bright-Rimmed Clouds and Young Stellar Objects in IC 1396*
  Choudhury, Rumpa., & Bhatt, H. C., 2010, Interstellar Matter and Star Formation: A Multi-wavelength Perspective, ASI Conference Series, 2010, Vol. 1, pp 225-227 Edited by D. K. Ojha, 1, 225

Papers Presented in Conferences:

- *Kinematic signatures of triggered star formation in BRCs,*
  Choudhury, Rumpa. & Bhatt, H. C., National Space Science Symposium (NSSS-2008), RAC, Ooty, India

- *Kinematics of the Young Stellar Objects associated with the Cometary Globules in the Gum Nebula*

  Choudhury, Rumpa., Young Astronomers' Meet 2009, Kharagpur, India

- *Triggered Star Formation and Young Stellar Population in IC 1396 : A view of SFO 38 & SFO 37*

  Choudhury, Rumpa., Mookerjea, Bhaswati., & Bhatt, H. C.,

  IAU Symposium 270: Computational Star Formation, Barcelona, Spain, May 31–June 4, 2010

- *Triggered Star Formation and the Young Stellar Population in Bright-Rimmed Clouds*

  Choudhury, Rumpa., Mookerjea, Bhaswati., & Bhatt, H. C.,

  The Origin of Stellar Masses, Tenerife, Canary Island, Spain, Oct 18-22, 2010

Dedicated to my parents

Abstract

The interaction of high and low mass stars, with their large and small scale environments respectively, can be destructive as well as constructive. The aim of this thesis work is to understand some aspects of interaction of high and low mass stars with their environment. Massive stars interact with their parent Giant Molecular Clouds (GMCs) and also affect the large scale structure of the galaxies. Observational evidences of radiative and mechanical feedbacks of massive stars, (e.g. *Radiation Driven Implosion (RDI)*, *Rocket Effects*, supernova explosion etc.) on their parent GMCs have been studied in two Galactic H II regions IC 1396 and Gum Nebula. Low to intermediate mass Pre-Main Sequence (PMS) stars interact with their circumstellar environments through accretion and outflow processes. Low mass stars disrupt their circumstellar environment by accreting circumstellar material, radiation and energetic outflows. Accretion rates seem to decrease with the age of the PMS stars. Long term variation of $H\alpha$ profiles of Herbig Ae star V351 Ori has been investigated to study the interaction of a relatively evolved PMS star with its circumstellar environment. In order to make the observations with appropriate resolution, observational techniques used for this work include broad-band to narrow-band optical imaging and photometry, infrared photometry, and medium to high resolution optical spectroscopy.

Constructive feedback of massive stars in the form of triggered star formation has been studied in Bright-Rimmed Cloud (BRC) SFO 38 in IC 1396. The young stellar population in and around SFO 38, one of the massive globules located in the northern part of the Galactic H II region IC 1396, has been investigated using the *Spitzer* IRAC and MIPS observations (3.6-24 μm), and followed up with ground-based optical photometric and spectroscopic observations. Spectral types, effective temperatures, masses, accretion rates and individual extinction of the relatively bright and optically visible Class II objects are determined from medium resolution spectroscopy. Continuum-subtracted $H\alpha$ line image is used to detect the ionizing sources of the globule. Two OB type stars e.g. HD 206267 (O6.5) and HD 206773 (B0V) are proposed as the potential ionizing sources for the globule. We also find that Class II to Class 0/I objects are distributed, in a systematic pattern, from the rim to the core part of the globule respectively. The spatio-temporal gradient in the distribution of YSOs along two different axes that are aligned with either of the ionizing stars indicates triggered star formation due to Radiation Driven Implosion.

Disruption of remnant molecular clouds by the massive stars has been studied in southern Galactic H II region Gum Nebula. An analysis of the proper motion measurements of the

Young Stellar Objects (YSOs) associated with the Cometary Globules (CGs) in the Gum Nebula is presented to measure the expansion of the system of the CGs. In particular, the kinematics of two YSOs embedded in CGs are investigated to check the consistency with the supernova explosion of the companion of ζ Pup, about 1.5 Myr ago being the cause of the expansion of the system of the CGs. Our analysis does not support the value of Rocket Effect velocity of ~ 40 km/s, and indicate a lower value of the velocity less than 5 km/s. We suggest that the nearly circular distribution of CGs with an average radius of ~ 70 pc is created due to the photoevaporation by massive stars of the nearest OB associations.

The patterns and timescales of temporal variability of emission line profiles have been investigated in order to study the circumstellar environment of the PMS Herbig Ae star V351 Ori. 45 high-resolution (R$\sim$ 28 000) spectra of V351 Ori were obtained on timescales of hours, days, and months to analyze the Hα line profiles and also to examine the $H\beta$, $NaD1$ and $NaD2$ line profiles to explore the nature of the spectroscopic variability. Average Hα line profiles of V351 Ori have been compared with the synthetic line profile to detect variations. Transient absorption features, that originate due to the time-dependent interaction of young star and its circumstellar environment, are analyzed. Both infalling and outflowing material detected in our observations are found to be decelerated with a rate of a few to fractions of m s^{-2}. The presence of elongated red-shifted components at some epochs supports the episodic nature of accretion. Variable emission and absorption components detected in Hα line profiles show the dynamic nature of interaction between V351 Ori and its circumstellar environment. Dynamic magnetospheric accretion and disk wind emerge as the most satisfactory model for interpreting the observed line profile variations of V351 Ori.

Young Stellar Objects and their Environment

Chapter 1

Introduction

Stars are the basic building blocks of the galaxies. Diffuse matter that pervades the space between stars in galaxies is known as interstellar medium (ISM). The ISM consists of gas (atoms, molecules, ions), larger dust grains, high-energy particles (cosmic rays) and radiation field. Major portion, almost 99% of ISM by mass, is gaseous in nature and nearly 1% is contributed by dust. The density of ISM varies over a range of 0.0001 to 10^6 atoms/cc. Variation in temperature in ISM ranges from 10 to 10^7 K. The diversity of density and temperature originate from various processes (e.g. formation of cold molecular cloud to hot ionized medium) that take place in the dynamic and active ISM. ISM is divided into different sub-components (McKee & Ostriker, 1977) e.g.

- Hot Ionized Medium (HIM) $\Rightarrow$ temperature: $\geq 10^6$ K, density: 10^{-4}–10^{-2} atoms/cc

- Warm Ionized Medium (WIM) $\Rightarrow$ temperature: ~ 8000 K, density: 0.2–10^4 atoms/cc

- Warm Neutral Medium (WNM) $\Rightarrow$ temperature: ~ 6000 K, density: 0.2–0.5 atoms/cc

- Cold Neutral Medium (CNM) $\Rightarrow$ temperature: ~ 80 K, density: 20–50 atoms/cc

- Molecular Clouds $\Rightarrow$ temperature: ~ 10–20 K, density: 10^2–10^6 atoms/cc

Stars form deep inside the relatively dense concentrations of interstellar gas and dust known as molecular clouds. Stars with masses up to $2 M_\odot$ are considered as low-mass stars, between 2 to 8 $M_\odot$ as intermediate mass stars and beyond 8 $M_\odot$ stars as high-mass or massive stars. Low-, intermediate- and high-mass star formation depend on the physical conditions in the ISM and the masses of the parent molecular clouds. Massive stars (≥ 20 $M_\odot$) dominate the energy feedback in ISM, produce all the heavy elements, contribute virtually to all the visible light come from the distant galaxies. Massive stars are also the source of powerful winds, and at the end of their lives undergo supernova explosions that inject significant energy and momentum in addition to newly synthesized nuclei into their surroundings. The mixing of ejecta from the massive stars into interstellar medium is an important process that control the chemical evolution of galaxies. Low mass stars are the dominant stellar

component of the spiral galaxies and contain nearly half the stellar mass of the galaxies. The long life-cycle of low-mass stars compared to their higher mass counterparts, make these stars as the ideal diagnostic to study the structure and history of our home galaxy the Milky Way. Interaction of the young low-mass stars with their ambient ISM through energetic outflows, is considered as one of the main source of turbulence in star forming regions. Some aspects of interaction of both high- and low- mass stars with their environment are discussed in the following sections.

1.1 Interaction of Massive Stars with Interstellar Medium

The mechanical feedback of massive stars in form of wind, supernova explosion etc. serve as the energy and momentum input to ISM causing interstellar medium turbulence and the formation of shells and cavities and thus lead to disruption of parent molecular clouds which prevents further star formation. At the same time, massive stars also play a constructive role in the next generation star formation by compression of nearby dense molecular gas. Among the various feedback processes of massive stars to ISM, only a few can cause compression of the remnant gas of the molecular cloud and trigger star formation. The essential condition is that the compressive force has to last for a time comparable to the collapse time in the compressed region. Individual supernova seem too short-lived to trigger star formation in the ambient ISM (e.g., Desai et al., 2010). Most important effects of massive stars that lead to constructive output (e.g. star formation) are the H II regions, stellar winds bubbles etc. that occur in OB associations and star complexes. The complex and intimate interaction of massive stars and ISM play an important role in the cycling of matter in the galactic environment.

1.1.1 Evolutionary Stages of Massive Star Formation

Massive stars are born in relatively large groups, known as OB association, in dense, and dusty Giant Molecular Clouds (GMCs). GMCs mainly consist of H_2 and CO molecules and are the largest gravitationally bound structures in the galaxies where massive to low mass stars are formed. The typical sizes of GMCs in the Galaxy vary from 50 pc to several hundred parsecs, and their masses vary from 10^4 $M_\odot$ to 10^7 $M_\odot$ (Blitz, 1993). High-mass stars can be on the main sequence while they are still deeply embedded and actively accreting as well as after they cease accreting and reach the final stage of their formation. A comprehensive theory of formation and evolution of high-mass stars is not well-established in the literature. Different formation scenarios have been proposed e.g. massive stars can form via collapse in isolated cores, physical collisions and mergers of protostars in very dense systems or via competitive accretion in a proto-clustered environment (e.g. Zinnecker & Yorke, 2007 and references therein). Though it is not clear which scenario is close to reality,

but observational studies of the earliest stages of high-mass star formation hint towards the formation of massive stars through gravitational collapse of massive cores with ongoing accretion from its surroundings (e.g. Beuther et al., 2007 and references therein). Beuther et al. (2007) proposed that the evolutionary sequence of high-mass star formation can be represented by the following phases

- High-mass Starless Cores (HMSCs)

- High-mass Cores harboring accreting Low/Intermediate- Mass Protostar(s) destined to become a high-mass star(s)

- High-mass Protostellar Objects (HMPOs)

- Final high-mass stars

Massive starless clumps can harbor only HMSCs (and low-mass starless cores) but massive proto-clusters can harbor low- and intermediate-mass protostars, HMPOs, HMCs, HCHIIs, UCHIIs and even HMSCs. HMPOs are accreting high-mass protostars and HMPO groups generally consist of protostars >8 M$_\odot$, which have not formed a detectable Hot Molecular Core (HMC) and/or Hypercompact H II region (HCH IIs, size < 0.01 pc). Ultracompact H II regions (UCH IIs, size < 0.1 pc) either harbor accreting protostars or protostars with already ceased accretion. High-Mass Cores harboring accreting Low/Intermediate- Mass Protostars are the stages between the HMSCs and the HMPOs, consisting of high-mass cores with embedded low/intermediate-mass objects. At the final stage, the massive stars are observed as an OB association inside the H II regions. The journey of the massive stars begins in the cold molecular cloud, they destroy their ambient medium and transform it into a hot H II region and finally, during their end phase as supernova explosions, change the surroundings as Hot Ionized Medium (HIM). Thus massive stars influence dynamically the shape, structure and energetics of almost all the phases of the ISM on timescales of a few Myr.

1.1.2 Feedback of Massive Stars to their Parent Giant Molecular Clouds

High-mass stars experience a short but exciting life because they play an important role in the galaxy's energy budget and thus have a major influence on the structure and evolution of galaxies. Massive stars of spectral types O or B emit most of their energy as ultraviolet radiation (beyond the Lyman limit), and convert the surrounding gas of the GMCs to ionized medium. The volume of ionized gas surrounding the massive stars is referred to as H II region because the principal constituent of the region is ionized hydrogen. But OB- type stars cannot ionize an indefinitely large amount of surrounding material because recombination occurs continuously within the gas and as a result photons are continuously

absorbed. OB- type stars can ionize a net volume of gas in which the total recombination rate is equal to the rate at which the OB- type stars emit the Lyman photons. The volume is known as Strömgren sphere and the radius is called Strömgren radius (R_s) defined as,

$$R_s = \left(\frac{3}{4\pi} \frac{S_\star}{n^2 \beta_2} \right)^{1/3}$$

where $S_\star$ is the rate at which the OB- type stars emit the Lyman photons, n is the number density of hydrogen and β_2 is the total recombination coefficient. The typical temperature of H II region is 10^4 K. The resulting high pressure region, produced by high temperature and increased number density (due to ionization), expands into surrounding remnant molecular cloud at roughly the speed of sound in the hot gas. This pressure-driven expansion typically continues until the H II region breaks free of the confining molecular cloud, at which point the gas in the interior of the region rapidly vents into the inter-cloud ISM. Of the ionizing radiation that does not escape the cavity altogether, reaches the wall of the cavity where it is absorbed in a very thin zone called an ionization front. This ionization front interacts with the pre-existing dense clumps (also known as globules) of the GMCs which are also potential sites for star formation. Due to this interaction, the exterior surface of the pre-existing globules, facing the massive stars, turns into dense shell of ionized gas, known as the bright-rim, observed on the head of the globules. The high pressure at the surface of the globules also drives a photoevaporative flow of photoionized material away from the surface of the globule into the interior of the H II regions. Due to momentum conservation the globules also get a relative velocity in the radially outward direction from the central star. This mechanism is known as *Rocket Effect* (Oort & Spitzer, 1955). The rocket effect pushes the loosely bound gaseous envelope much more effectively than the dense core and forms tail-like structures behind the dense head of the globules. These globules with bright-rim, facing the ionizing sources, and tail-like features, in radially outward direction from the massive stars, are known as Bright-Rimmed Clouds (BRCs) and Cometary Globules (CGs). Influence of the *Rocket Effect* on the distribution of CGs in Galactic H II region Gum Nebula has been discussed in Chapter 3.

The H II cavity in the molecular cloud with BRCs and CGs is referred to as a blister H II region (Figure 1.1). The pressure at the ionization front drives a shock into the interior of the BRCs/CGs, compressing that gas and driving up the pressure. The ionization front and its shock typically move into the BRCs/CGs at velocities of order a few km/sec. Ionization fronts are apparent in Figure 1.1 as the bright-rims seen at the edge of the H II region. Shocks driven in advance of ionization fronts compress the dense molecular gas in the BRCs/CGs. The neutral gas ahead of the shock front is then compressed which leads to formation of dense cores. Eventually these dense cores collapse to form a new generation of
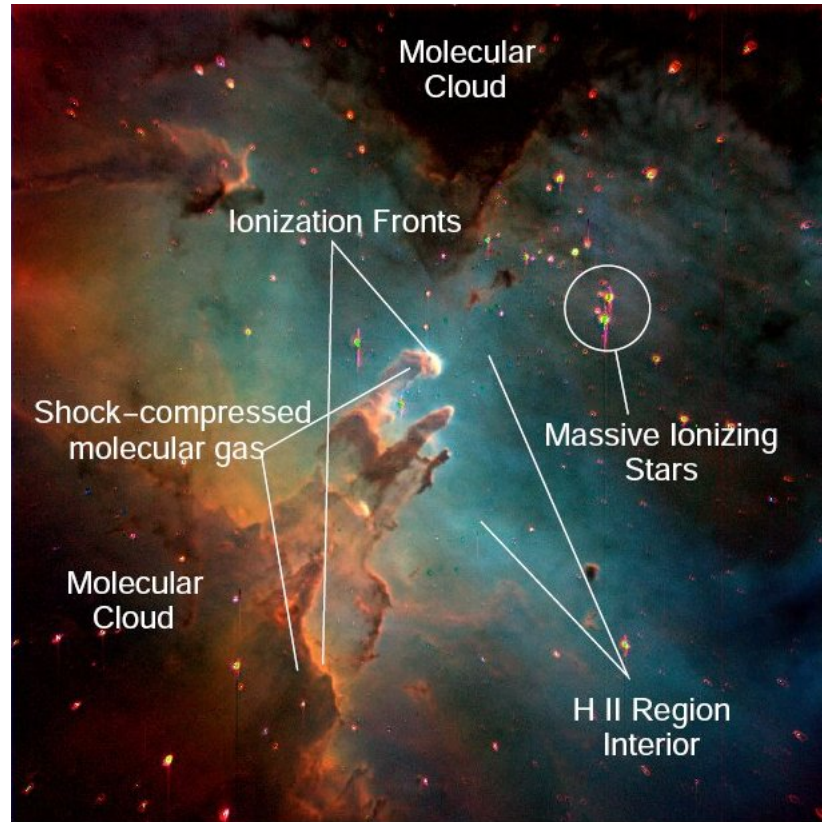
Figure 1.1 The structure of a blister H II region. Fig. from Hester & Desch (2005).

stars. This is known as Triggered Star Formation by Radiation Driven Implosion. Triggered star formation in the dense heads of BRCs has been predicted (e.g., Klein et al., 1980) and observed for many years (e.g., Sugitani et al., 1989). Detail study of triggered star formation in BRCs in IC 1396 is presented in Chapter 2.

1.1.3 Characteristics and Evolution of Bright-Rimmed Clouds and Cometary Globules

Bright-Rimmed Clouds and Cometary Globules are found at the borders of H II regions. Sugitani et al. (1991) and Sugitani & Ogura (1994) prepared a catalog of 89 BRCs from the whole sky Palomar Sky Survey prints. They classified the BRCs in three sub-groups based on the curvatures e.g. type A, B and type C (Fig 1.2). Cloud with a rim displaying moderate curvature is termed as A type, cloud with a rim of a high degree of curvature is termed as B type and finally cloud with a tightly curved rim and a tail is termed as C type, which is also known as cometary globule.

Zealey et al. (1983) also listed the cometary globules in the southern Galactic H II region Gum Nebula. Though it is thought that Type A →B →C are connected through evolutionary sequence, but recent numerical simulation by Miao et al. (2009) suggested that depending on its initial gravitational state, a cloud could evolve to any one of the
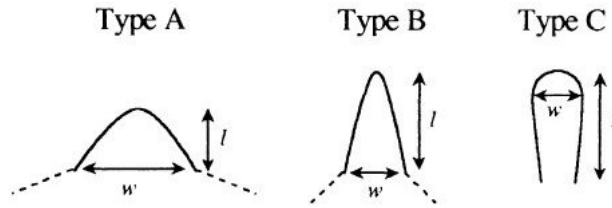
Figure 1.2 Classification of the rim-shape and definition of the rim-size. Fig. from Sugitani et al. (1991)

three type BRCs. Their simulation also showed that triggered star formation by radiation driven implosion could occur within any of BRCs including the type A BRCs. According to Miao et al. (2009), the globules closest to the central star could possibly evolve into a quasi-equilibrium type A BRC because they have highest initial self-gravitational potential energies, while for those globules farther away, they evolve from type A to a quasi-equilibrium type B BRC because of their moderate initial self-gravitational potential energies. For the globules farthest away from the OB- type stars, they evolve to pass type A and B morphologies, then to a cometary type C morphology due to their lowest initial self-gravitational potential energies. So the spatial sequence of type A-B-C BRCs with their distances to the central star can be seen as a manifestation of the mass density distribution of the very clumpy giant molecular clouds. The projected distances of three star forming BRCs from the O-type star HD 206267 in northern Galactic H II region IC 1396, SFO 36 (type A), SFO 38 (type B) and SFO 37 (type C) are 4.9, 10.7, 12 pc, are also consistent with the proposed model.

1.2 Interaction of Low-mass Stars with Circumstellar Environment

The region of influence of the stars on their surrounding environment decreases as their mass decrease. Low to intermediate mass stars mostly affect and interact with their circumstellar environment whereas high mass stars not only affect the whole natal environment but these stars also control the evolution of their parent molecular clouds. Interaction between young Pre-Main Sequence (PMS) stars and their circumstellar disks is one of the most important processes in the early stellar evolution. In the initial phases, protostars may directly accrete low angular momentum material radially infalling from their parental cloud. But most of the stellar mass buildup occurs through disk accretion. Disk accretion regulates the final stellar mass, removing angular momentum via viscous dissipation and loosing mass through collimated outflows (e.g., Hartmann 2009). Disk accretion process becomes less significant as the young star ages (Hartmann, 2009), and, for low-mass stars (M $<1M_\odot$), accretion terminates within the disk lifetime (6–10 Myr; e.g. Manoj et al., 2006; Hernández et al.,

2009), well before the star reaches the main sequence. Evolutionary stages of the low-mass stars are briefly described in the next section.

1.2.1 Evolutionary Stages of Low-mass Star Formation

In contrast with the massive stars, formation and evolutionary scenario of low mass stars are better understood. Low-mass star formation can take place in GMCs as well as small molecular globules of sizes of few pc. Historically, small dark globules were first identified as the probable sites for star formation. The existence of dense clouds as the dark, starless patches was first established by Barnard (1919). Whipple (1946) and Spitzer (1948) first suggested that dense clouds which could form due to the compression of dust grains by interstellar radiation, could form stars through gravitational contraction. Bok & Reilly (1947) also hypothesized that these clouds are undergoing gravitational collapse to form new stars and star clusters. Stars in the earliest stages of development are called as Young Stellar Objects (YSOs). YSOs form from the "clumps" ($\sim$1 pc) or "cores" ($\sim$0.01 pc) of GMCs or Bok Globules. Shu et al. (1987) gave a detailed description of low-mass star formation in their seminal paper.

Star formation begins when slowly rotating cloud cores form inside the denser parts of the cloud clumps. Core formation happens due to the fragmentation of the clumps. Clumps may produce a single star, or a multiple stellar system depending on the mass of the clumps and nature of fragmentation. The cores slowly approach the centrally concentrated state, more like a singular isothermal sphere. This phase is known as pre-stellar phase and lasts for $\sim 10^6$ yr.
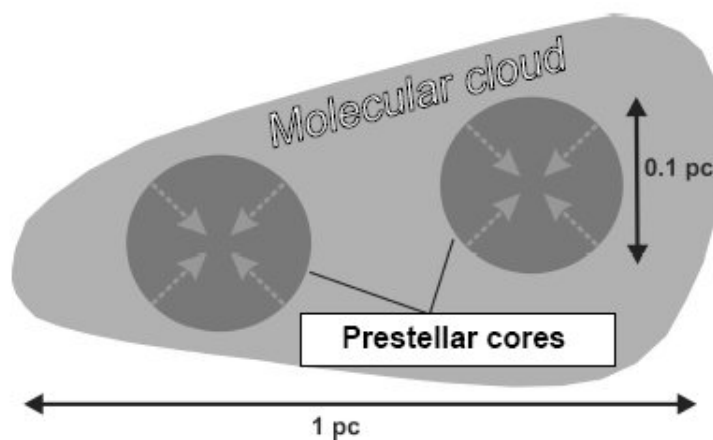
Figure 1.3 Fragmentation and collapse phase of low-mass star formation. Fig. from `http://www.arcetri.astro.it/~elba03/Andre.pdf`

The minimum mass of a gas cloud of temperature T and density ρ that will collapse under gravity is known as Jeans mass and is given by

$$M_J = \left(\frac{5kT}{Gm}\right)^{3/2}\left(\frac{3}{4\pi\rho}\right)^{1/2}$$

The cores which have masses greater than Jeans mass (M_J) (i.e. gravitational energy > thermal energy of the volume of the cores), collapse dynamically "inside-out" i.e. center will collapse faster than exterior. For typical mean density ($n \sim 10^4$ cm^{-3}) and assuming free-fall collapse, the effective timescales for this phase would be $\sim 4\times10^5$ yr. Once core density reaches $\sim 10^{13}$ g cm^{-3}, the region becomes optically thick and the collapse becomes adiabatic rather than isothermal. In this stage, gravitational energy cannot escape the core and core contracts slowly and temperature also rises. When the core is in hydrostatic equilibrium with radius ~ 5 AU, it is called a protostars or Class 0 source (Andre & Montmerle, 1994). The main characteristic of this phase is a central protostar surrounded by an infalling envelope of gas and dust and a circumstellar disk. Extended envelopes of Class 0 sources can be observed in sub-mm and millimeter maps. The main accretion phase is always accompanied by a powerful ejection of a small fraction of the accreted material in the form of prominent bipolar molecular outflow. Class 0 sources are identified either by free-free emission at cm wavelength or by molecular outflows. Typically for Class 0 sources $L_{smm}/L_{bol} > 0.005$, $M_\star < M_{env}$ and $T_{bol} < 80$ K [1] i.e. not much hotter than parent molecular cloud cores.

Above the adiabatic protostar-cores, isothermal free-fall accretion of circumstellar material continues and core density and temperature continue to increase. The YSOs in this phase is known as Class I source (Adams et al., 1987). In this phase, the typical sizes of infalling envelope and optically thick disk are $\sim$100 AU and a few 100 AU respectively. In Class I sources, primary stellar winds increase and bipolar outflows start to sweep-up surrounding material with hypersonic velocity. These jets extend up to $\sim$1 pc, and this interaction with ambient cloud medium create clumpy shock-excited gas, known as Herbig-Haro objects. Class I sources shows excess near infrared (NIR) and mid infrared (MIR) emission, arising due to large amounts of circum-protostellar dust. Other important characteristics of Class I sources are 10μm silicate absorption feature, H_2O masers etc. Masers originate from small dense areas where microwave transitions in H_2O are non-linearly amplified by stimulated emission. It is also observed that $\sim$50% of Class I sources exhibit atomic emission lines in NIR, but otherwise spectra are featureless and heavily veiled.

Due to accretion and stellar winds, Class I sources clear the remnant envelope and as a result accretion rate slows due to lack of infalling matter. Optically thick circum-protostellar disk also become optically thin protoplanetary disk (Proplyd) and probably planet formation starts in these disk. The stars also become optically visible (transition from protostar to

---

[1]Bolometric temperature: The temperature of a black body with the same mean frequency as the observed spectral energy distribution.
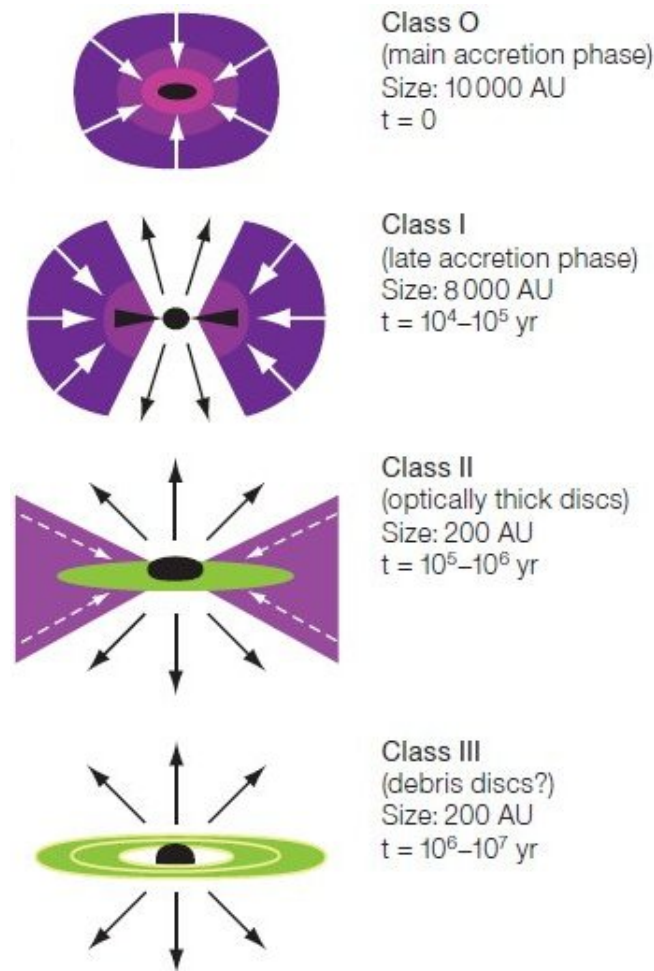
Figure 1.4 Evolutionary stages of low-mass star formation. Fig. from Andreani & Wilson (2006)

pre-main sequence star) at an age of few 10^6 yr and known as Class II sources or Classical T Tauri Stars (CTTS) (Joy, 1945). CTTSs show emission from H-Balmer series, Ca II, iron, absorption lines in Li, and forbidden lines of [O I] and [S II] (originate from low density gas). Spectral Energy Distributions (SEDs) peak in visible or NIR, with some UV excess, but broader than single black body function and fall in power-law fashion beyond 2μm. In this phase IR excess arises due to circumstellar disk only.

The last phase of the evolution of low-mass stars corresponds to that of Class III sources (age: 5×10^6 yr), also known as Weak-lined T Tauri Star (WTTS). SEDs of Class III sources peak in visible and NIR and drops more steeply than Class II beyond 2μm. The SED also approach toward single temperature black body i.e. photosphere of young stars. However visual light could still be substantially extinguished by dust. Hα emission of Class III sources also drops substantially (Hα equivalent width > 10Å CTTS and <10 Å WTTS). Class III sources also show strong and variable X-ray emission. When the temperature at core reach $\sim$10 MK, hydrogen fusion begins and the stars appear on the Main-Sequence.

1.3 Scope and Plan of the Thesis

The interaction of high and low mass stars, with their large and small scale environments respectively, can be destructive as well as constructive. Massive stars can terminate nearby star formation by destroying the molecular clouds and also can trigger star formation by the compression of the leftover molecular clouds. H II regions are the most spectacular examples of destructive and creative effects of massive stars on their parent molecular clouds. On the other hand, low mass stars disrupt their circumstellar environment by accreting circumstellar material, radiation and energetic outflows. At the same time, planet formation can takes place in the circumstellar disks of low mass stars.

The aim of this thesis work is to understand some aspects of interaction of high and low mass stars with their environment. Radiative and mechanical feedbacks of massive stars to their parent molecular clouds, e.g. *Radiation Driven Implosion*, *Rocket Effect*, mechanical feedback of supernova explosions etc., have been investigated. For this purpose, Young Stellar Objects associated with the Bright-Rimmed Clouds and Cometary Globules of the two Galactic H II regions IC 1396 and Gum Nebula have been used as the diagnostic tools. Herbig Ae star V351 Ori has been investigated to study the interaction of circumstellar environment and a Pre-Main Sequence star. In a nutshell, we have used the various properties of the embedded YSOs to understand some aspects of the large scale environment of BRCs/CGs which are the integrated components of H II regions and OB association and we also explore the small scale environment around the PMS stars by investigating their interaction with the circumstellar environment. The size-scales involved in specific observations of these targets range from a fraction of an AU to tens of pc. In order to make the observations with appropriate resolution, observational techniques used for this work include broad-band to narrow-band optical imaging and photometry, infrared photometry, and medium to high resolution optical spectroscopy.

The plan of the different chapters of the thesis is as follows.

In Chapter 2, constructive feedback of massive stars in the form of triggered star formation has been studied. The young stellar population in and around SFO 38, one of the massive globules located in the northern part of the Galactic H II region IC 1396, has been investigated using the *Spitzer* IRAC and MIPS observations (3.6-24 μm), and followed up with ground-based optical photometric and spectroscopic observations. Spectral types, effective temperatures, masses, accretion rates and individual extinction of the relatively bright and optically visible Class II objects are determined from medium resolution spectroscopy. Continuum-subtracted Hα line image is used to detect the ionizing sources of the globule. Spatial distribution of YSOs is used to identify the signatures of sequential star formation. Shock propagation speed inside the globule is calculated using the spatial and temporal properties of the YSOs.

In Chapter 3, disruption of remnant molecular clouds by the massive stars has been studied. An analysis of the proper motion measurements of the YSOs associated with the CGs in the Gum Nebula is presented to measure the expansion of the system of the CGs. In particular, the kinematics of two YSOs embedded in CGs are investigated to check the consistency with the supernova explosion of the companion of ζ Pup, about 1.5 Myr ago being the cause of the expansion of the system of the CGs.

In Chapter 4, the patterns and timescales of temporal variability of emission line profiles have been investigated in order to study the circumstellar environment of the pre-main sequence Herbig Ae star V351 Ori. 45 high-resolution (R$\sim$ 28 000) spectra of V351 Ori were obtained on timescales of hours, days, and months to analyze the Hα line profiles and also to examine the $H\beta$, $NaD1$ and $NaD2$ line profiles to explore the nature of the spectroscopic variability. Average Hα line profiles of V351 Ori have been compared with the synthetic line profile to detect variations. Transient absorption features, that originate due to the time-dependent interaction of young star and its circumstellar environment, are analyzed. The kinematics of these features are used to measure the rate of change in velocity of the infalling and outflowing material of the star-disk system. Possible explanation of the Hα line profile variation is also discussed based on the available models of star-disk interaction.

In Chapter 5, the important results of this work have been summarized. Some future steps for further investigation of the interaction of the young stars and their environment are also given.

Feedback of Massive Stars to Giant Molecular Clouds

Part I. Radiation Driven Implosion

Chapter 2

Sequential Star Formation in Bright-Rimmed Cloud SFO 38 of H II Region IC 1396

2.1 Introduction

Once a single massive star forms, the combined energy and momentum input from that star quickly reshapes its environment, dominating all that goes on in its surroundings, including the formation of bubble like structures. Observational and theoretical studies of star formation over the last decade have increasingly strengthened the idea that massive young stars also play an important role in triggering the formation of subsequent generations of stars. The triggers of star formation which are typically in the form of stellar winds, radiation and supernova explosions of the massive stars or expansion of H II regions essentially involve shock compression of a molecular cloud externally. Among several proposed theories, two models have gathered sufficient observational support in order to be regarded as the most plausible models for triggered star formation. In the first model known as the *Collect and Collapse* (Elmegreen & Lada, 1977; Hosokawa & Inutsuka, 2006) model, an expanding H II region sweeps up material into a dense bordering layer between the H II region and the molecular cloud. The compressed shell of gas and dust undergoes fragmentation and gravitational collapse to form new stars. Observational evidence supporting the "collect and collapse" model includes detection of a dense, fragmented shell of gas with newly formed stars surrounding the H II region (Deharveng et al., 2003, 2009; Zavagno et al., 2006, 2007). The *collect and collapse* model was proposed primarily to explain the triggered formation of massive stars. An equally likely model based on *Radiation Driven Implosion (RDI)* (Bertoldi, 1989; Bertoldi & McKee, 1990), involves the creation of shock front at the surface of molecular clouds due to photoevaporation from the cloud-surfaces exposed to the UV radiation of nearby massive young stellar clusters. The enhanced inward pressure triggers the formation of new protostellar cores or compresses pre-existing ones to

form a new generation of stars. Observational evidence for the RDI model includes typical spatial distribution and gradient in evolutionary ages of young stellar objects (Ikeda et al., 2008). There is however considerable ambiguity regarding whether RDI actually induces the gravitational collapse or merely exposes the young stars by photoevaporation, since these two scenarios have been hard to distinguish observationally. Therefore, more observations and detailed studies of triggered star formation in different environmental settings and evolutionary stages, are required for a better understanding of this mode of star formation.

Bright-Rimmed Clouds (BRCs) are isolated molecular clouds located on the edges of evolved H II regions and remnant molecular material of the parent GMCs, which are found to have many signposts of star formation, i.e., *IRAS* point sources, molecular outflows, HH objects etc. Sugitani et al. (1999) and Sugitani et al. (2000) observed a sample of 89 BRCs and found an excess in the luminosities and luminosity-to-cloud mass ratios of embedded *IRAS* sources when compared with sources in isolated globules, which is an indication of enhanced star formation in the BRCs. Young stellar objects seemingly aligned along the axis towards the ionizing cluster were detected via near-infrared (NIR) imaging of 44 of these BRCs. There is also evidence for an age gradient, with older stellar objects closer to the OB cluster and the younger objects well inside the globules, aligned with the IRAS sources. These results are consistent with sequential formation of stars while the shock front advances further and further into the molecular cloud. Thus BRCs are ideal objects for studying and verifying the different models of triggered star formation.

The aim of this chapter is to look for the observational evidence of interaction of massive stars with their parent Giant Molecular Clouds, in particular, triggered star formation in BRCs, by RDI mechanism. We planned to use the various properties of the young stellar population in BRCs to recover the star formation history and the signatures of the external forces on the characteristics of the YSOs in BRCs, if any. To facilitate this kind of study, well-resolved multiwavelength observations of young stellar population of BRCs are required. We selected the BRC SFO 38 in H II region IC 1396 and used the observed properties of the YSOs to diagnose the effect of the massive stars on next generation star formation.

2.2 Star Formation in Bright-Rimmed Cloud SFO 38 in IC 1396

The H II region IC 1396, powered by the O6.5V type (Stickland, 1995) star HD 206267 in the Trumpler 37 cluster, appears to sweep up a molecular ring of radius 12 pc (Patel et al., 1998) and is surrounded by 11 Bright-Rimmed clouds with embedded IRAS point sources (Sugitani & Ogura, 1994; Sugitani et al., 1991). In Fig. 2.1, major star forming regions of Cepheus including IC 1396 are shown, which indicate that IC 1396 bubble is situated at
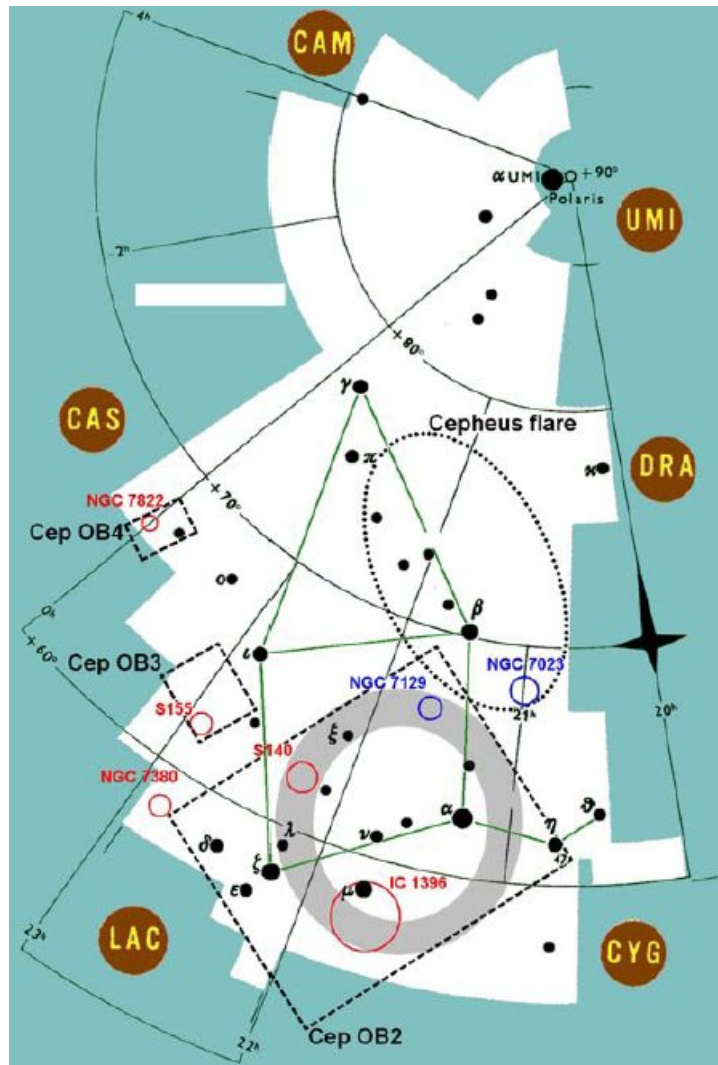
Figure 2.1 Positions of the major star forming regions of Cepheus, overplotted on a schematic drawing of the constellation. Fig. from Kun et al. (2008)

the border of a bigger shell. There are other star forming regions (e.g. S140, NGC 7129) at the border of the same shell. It may be possible that this bigger shell was produced by the feedback of first generation of massive stars in this region.

In this chapter we concentrate on the star formation in Bright-Rimmed Clouds of IC 1396. The BRCs in IC 1396 are situated in a circular pattern with the bright rim corresponding to the ionization front facing the central ionizing star. SFO 38 (Sugitani et al., 1991) also known as IC 1396N, is located at a projected distance of $\sim$11 pc to the north of HD 206267. IC 1396 is located in the Cep OB2 association at a distance of 750 pc (Matthews, 1979).

More recent *Hipparcos* parallax based measurements estimate the distance to Cep OB2 association to be 615 pc (de Zeeuw et al., 1999). However in order to make comparison of our results with most of the other published results, in this chapter we adopt a distance of 750 pc for SFO 38. The derived luminosities may therefore be overestimated by more than
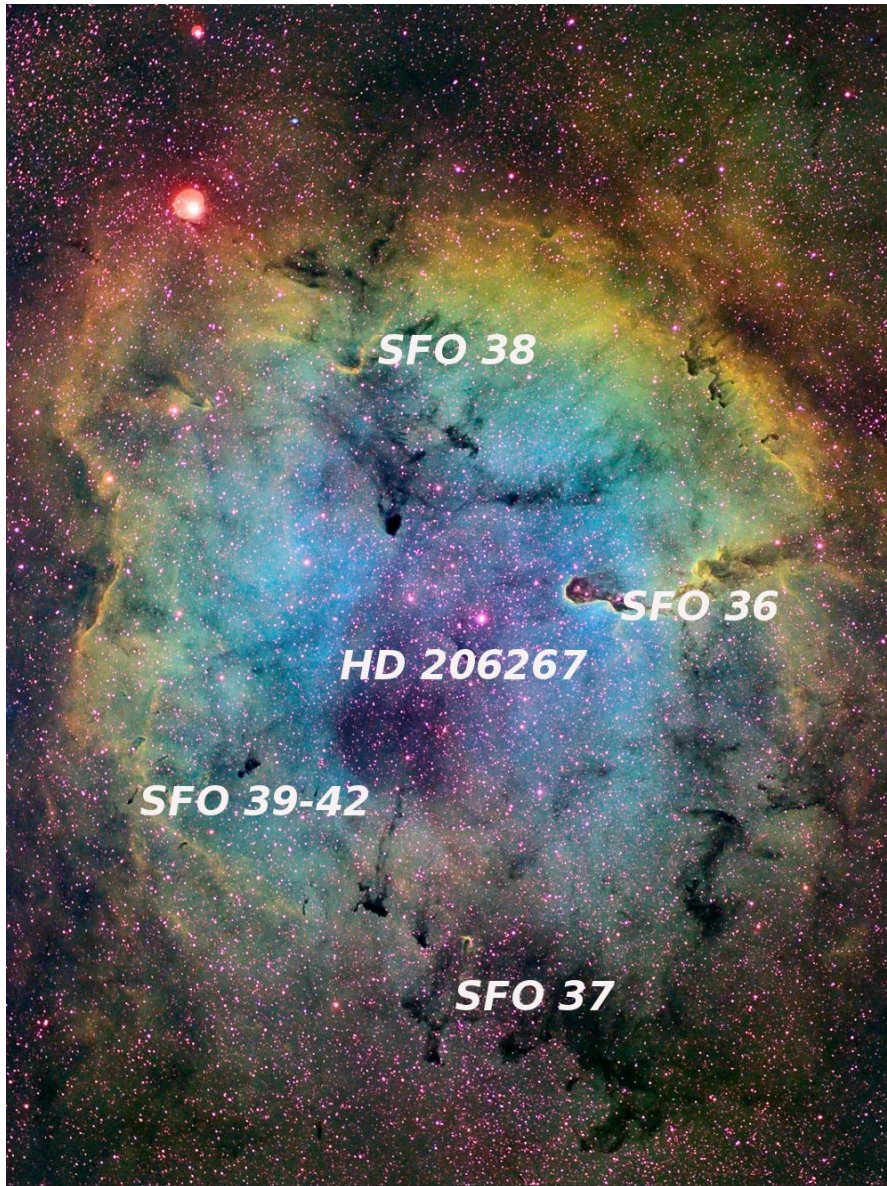
Figure 2.2 Color-composite image of H II region IC 1396. Bright-Rimmed Clouds and the O-type star HD 206267 are marked in the image. North is up, east is to the left. Fig. from `http://www.rc-astro.com/photo/id1031.html`

40% and physical sizes by 20% if a distance of 615 pc were used. The region is associated with IRAS 21391+5802, a very young intermediate-mass object, with a luminosity of 235 $L_{\odot}$ (Saraceno et al., 1996), which powers an extended bipolar outflow (Sugitani et al., 1989). Based on millimeter observations Beltrán et al. (2002) resolved IRAS 21391+5802 into an intermediate-mass source named BIMA 2 surrounded by two less massive and smaller objects, BIMA 1 and BIMA 3. Valdettaro et al. (2005) detected H_2O maser emission at 2.2 GHz towards SFO 38 which is consistent with an intermediate-mass object. Neri et al. (2007) used still higher angular resolution millimeter interferometric observations to reveal that the intermediate-mass protostar BIMA 2 itself consists of multiple compact

sources. The gas emission surrounding IRAS 21391+5802 traces different molecular out-flows (Codella et al., 2001; Beltrán et al., 2002, 2004). NIR images of the region have also revealed a number of small scale molecular hydrogen and Herbig-Haro (HH) flows (Nisini et al., 2001; Sugitani et al., 2002; Reipurth et al., 2003; Caratti o Garatti et al., 2006; Beltrán et al., 2009). These observations confirm the on-going star formation in the dense core of SFO 38.

Getman et al. (2007) identified the mid-infrared (MIR) (*Spitzer*) counterparts of X-ray sources detected in *Chandra* observations and found that the spatial distribution of Young Stellar Objects (YSOs) is aligned toward the ionizing star HD 206267 and shows an age gradient consistent with the RDI model for triggered star formation. Recently Beltrán et al. (2009) studied the YSO population of SFO 38 by obtaining deep J, H, K′ broadband images and deep high-angular resolution observations in the H_2 narrow-band filter (2.12 μm). Beltrán et al. (2009) did not detect any clear NIR excess close to the rim, which is in contrast to the age 1 Myr of the stellar population concluded by Getman et al. (2007). Beltrán et al. (2009) suggest that the YSOs closer to HD 206267 could actually be younger than the Class II objects they appear to be since their circumstellar environment were disrupted completely by intense UV radiation field from the OB association. Beltrán et al. thus suggest that in general the apparent age sequence seen close to OB associations need not necessarily be the actual evolutionary sequence and in the case of SFO 38 there is no concrete evidence of star formation triggered by the nearby OB association.

In this chapter we address the controversial issue of the distribution of YSOs by making use of the more sensitive *Spitzer* IRAC (3.6 to 8.0 μm) & MIPS (24 μm) observations in order to probe *all* embedded YSOs and protostars in SFO 38 and together with our optical broadband *BVRI* and narrow band Hα images to make a multiwavelength study of star formation in SFO 38 and structure of the bright-rim. This thus extends the work by Getman et al. (2007), who had considered the 3.6–5.8 μm characteristics only of those MIR sources from which X-ray emission had been detected. Our approach also complements the work by Beltrán et al. (2009) which makes use of only the NIR observations to decipher any age gradient of the YSOs.

In this work we shall show that most of the Class 0/I sources identified in the MIR are either barely detected (with large uncertainties in fluxes) or not detected at all in the NIR and in the X-rays. Further in order to confirm the "*youth*" of the YSOs identified in the MIR we have made use of medium resolution spectroscopy of the optically visible YSOs in Hα line emission. Observational details of *Spitzer* and optical *BVRIH*α imaging and medium resolution spectroscopy are presented in § 2.3. We describe the selection of YSO candidates based on MIR color-color diagram (CCD) and the detailed analysis of optical–MIR data in section § 2.4. In § 2.5 we discuss the probable star formation scenarios.

2.3 Observations and Data Reduction

2.3.1 *Spitzer* IRAC & MIPS Observations

The Spitzer Space Telescope (Werner et al., 2004) is the largest infrared telescope ever launched into space by National Aeronautics and Space Administration (NASA), USA. Its highly sensitive instruments are Infrared Array Camera (IRAC), Multiband Imaging Photometer for Spitzer (MIPS) and Infrared Spectrograph (IRS). IRAC operates simultaneously at four wavelengths (3.6, 4.5, 5.8 and 8 μm). Each module uses a 256×256 pixel detector. The short wavelength pair use indium antimonide technology, the long wavelength pair use arsenic-doped silicon impurity band conduction technology. Three detector arrays of MIPS use 128×128 pixels at 24μm, 32×32 pixels at 70μm, and 2×20 pixels at 160μm. We have extracted IRAC (3.6, 4.5, 5.8, & 8 μm) and MIPS (24 & 70 μm) observations from the Spitzer Space Observatory archive (Program ID 30050: Star Formation in Bright Rimmed Clouds by Fazio et al.). The IRAC data were taken in the High Dynamic Range (HDR) mode using a single AOR (Astronomical Observation Request) with a five-point dither pattern. We have processed both the short (0.6 sec) and the long (12 sec) integration Basic Calibrated Data (BCD) frames in each channel using the Artifact mitigation software developed by Sean Carey [1] and created mosaics using MOPEX. In all IRAC bands we detect point-sources down to 70 μJy. We have also created mosaics of the MIPS 24 and 70 μm BCDs using MOPEX. Both data sets are of reasonably good quality. The 70 μm-image, due to the lower angular resolution and smaller area mapped, shows only one bright point-like source embedded in the globule.

We have carried out multiframe PSF photometry using the tool APEX developed by Spitzer Science Center (SSC) on all the *Spitzer* IRAC images and on the MIPS images. The long integration 3.6 and 4.5 μm IRAC images show signs of saturation on bright stars. For the saturated sources, the photometry derived from the short integration images were used. It is difficult to disentangle the sources in regions of strong emission from the associated Photon Dominated Regions (PDRs) from the surrounding clouds and to derive their accurate photometry. We have used a combination of automated routines and eye-inspection to detect sources and extract photometry of these sources from the IRAC and MIPS images. For sources, which APEX failed to detect automatically at one or several wavelengths, we have used the user list option in APEX to supply the coordinates for the source to successfully derive a PSF fit. This enabled us to derive photometry for every source which we could visually identify on any image. Following the IRAC and MIPS Data Handbooks we have adopted the zero-points for conversion between flux densities and magnitudes to be 280.9, 179.7, 115.0, 64.1 and 7.14 Jys in the 3.6, 4.5, 5.8, 8.0, and 24 μm bands, respectively.

---

[1] `http://web.ipac.caltech.edu/staff/carey/irac_artifacts/index.html`

2.3.2   Optical $BVRI$ Photometry

SFO 38 was observed on 17th July, 23rd August and 15th September 2009 using Bessell's broad band filters VR (300×8 s, 300×8 s), BVI (900×8 s, 300×8 s, 150×8 s) and BI (900×8 s, 120×12 s) respectively and on 4th November 2008 using the narrow band $H\alpha$ (900 s) with the Himalayan Faint Object Spectrograph Camera (HFOSC) mounted on the Himalayan Chandra Telescope (HCT) of the Indian Astronomical Observatory (IAO), Hanle, India[2]. HCT is a 2-m aperture optical-infrared telescope and remotely operated from CREST, Hosakote, near Bangalore, India, via a dedicated satellite link. The Himalayan Faint Object Spectrograph (HFOSC) is mounted on an instrument mount cube at the cassegrain focus of the telescope. HFOSC uses the central 2K×2K region of the 2K×4K CCD in imaging mode and covers a field of $10^{'}\times10^{'}$ with a plate scale of $0.''296$ $pixel^{-1}$. The nights were photometric with an average seeing of $1.''5$ to $1.''8$. Landolt (1992) photometric standard stars were observed on all the nights to calibrate the target stars. Data were reduced using standard tasks available within Image Reduction and Analysis Facility (IRAF)[3]. Bias subtracted, flat field corrected and aligned frames were combined to make the master frame for each filter. Astrometric calibration was applied to the master frames using the IDL procedure $STARASTT$ of IDL Astronomy User's Library[4]. Photometric magnitudes were calculated by aperture photometry with the optimal aperture adopted as the radius where the difference in magnitudes between two consecutive apertures is less than 1%. The limiting magnitude is defined as the magnitude at which the mean magnitude error of the star becomes 0.1 mag which implies a 10σ detection corresponds to a signal-to-noise ratio (S/N) of 10. The limiting magnitudes were V: 21, R: 21 on 17th July , B: 22, V: 22, I: 19.5 on 23rd August and B: 22.2, I: 20.2 on 15th September. Aperture corrections for each frame were derived from the bright and isolated stars and applied to the faint stars. The standard deviation of residuals of observed and transformed magnitudes and colors of the standard stars are within the range of 0.01-0.02 mag. We used the broadband R filter image for continuum subtraction from the narrow band Hα image of SFO 38. Based on the recipe of Waller (1990), the point spread functions of the R-band and the narrow band Hα images were matched and the images were scaled before subtraction to get the Hα emission line image of SFO 38.

2.3.3   Medium Resolution Spectroscopy

Medium resolution ($\sim$7 Å) spectra were obtained for relatively bright and optically visible YSOs during July–November of both 2008 and 2009 in the wavelength range (5200–9200 Å) with the Himalayan Faint Object Spectrograph Camera (HFOSC) mounted on

---

[2] http://www.iiap.res.in/centers/iao

[3] The IRAF software is distributed by the National Optical Astronomy Observatory under contact with National Science Foundation. http://iraf.noao.edu/

[4] http://idlastro.gsfc.nasa.gov/

the Himalayan Chandra Telescope (HCT). Typical exposure time of each spectrum was 3600 s. The spectra were bias subtracted, flat fielded and the one-dimensional spectra were extracted using the standard tasks of Image Reduction and Analysis Facility (IRAF). The arc lamp spectra of FeNe were used for wavelength calibration. We further used the strong night sky emission lines e.g. [OI] $\lambda5577$ Å, $\lambda6300$ Å lines and rotational and vibrational bands of OH in the red region of the individual target spectrum to improve the wavelength calibration and achieved an accuracy of $\pm$ 0.5 Å for each target star.

2.4 Results and Analysis

2.4.1 Mid-Infrared (3.6 to 24 μm) View of SFO 38

Figure 2.3 presents the three-color image of SFO 38 using the IRAC 3.6, 8.0 and the MIPS 24 μm bands. The image shows that the emission from the front side of the globule is dominated by strong polyaromatic hydrocarbon emission (PAH-emission), and is rather clumpy. This could in part be due to Rayleigh-Taylor instabilities at the ionization front, and also due to the outflows from the young stars. The cometary shape of the globule is quite apparent with the head pointed towards the O star HD 206267 and the eastern edge appears to be more abruptly truncated to the south. This indicates that the south-eastern edge of the globule has most likely experienced intense ionizing radiation field, which has eroded the cloud material more than on the western side. Comparison with the Hα emission line image (Fig. 2.5) also confirms the presence of a more pronounced ionization front to the south-east and a rather tenuous layer of ionized gas to the west of SFO 38.

The aim of this chapter is to identify the young and embedded stellar population in SFO 38. While the 3.6 and 4.5 μm IRAC data is particularly sensitive, a large number of stellar objects in addition to the YSOs also detected in these bands. We have thus used all sources detected either at 5.8 or at 8.0 μm or at both wavelengths to create a list of MIR sources in SFO 38. Photometry for all these sources, if detected, are then extracted from the 3.6 & 4.5 μm images. We thus detect 98, 106, 106 and 98 sources respectively in the IRAC 3.6, 4.5, 5.8 and 8.0 μm images and 14 and 1 sources respectively in the MIPS 24 & 70 μm images. All the sources detected at 24 μm are found to have been detected in the IRAC bands. In all we identify a total of 110 MIR sources. We have cross-correlated the MIR sources with the NIR sources in our mapped region from the 2MASS point source catalog, as well as the sources detected in the NIR by Nisini et al. (2001) and Beltrán et al. (2009). We have used the following association radii : 1″ for the IRAC images, 2″5 for the MIPS 24 μm image and 2″ for NIR data. Table 2.1 gives the coordinates of the 110 sources identified in SFO 38 together with their NIR magnitudes, *Spitzer* IRAC and MIPS flux densities and a preliminary classification based on selected color-color plots and other criteria described in Sec. 2.4.2. In Table 2.1 we have used the prefix SFO38, but throughout the chapter
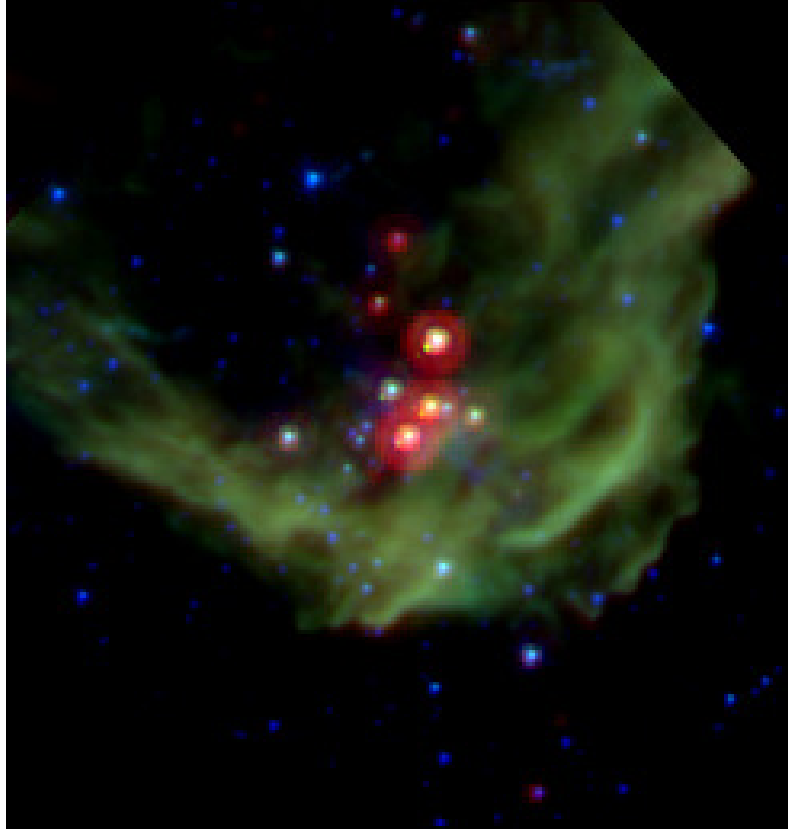
Figure 2.3 IRAC-MIPS color-composite image of SFO 38 using 3.6 μm (Blue), 8 μm (Green) and 24 μm (Red). The image is centered at $\alpha_{2000} = 21^h 40^m 42^s$ and $\delta_{2000} = 58°16'10''$ and extends over $5' \times 5'$ ($\alpha \times \delta$).

we refer to them as MIR-nn, where nn is the identification number of the source. Out of the 110 sources 80 were found to have NIR counterparts. However 10 sources out of the 80 sources with NIR counterparts were found to coincide with the H_2 knots identified by Beltrán et al. (2009).

Additionally in order to identify the stellar and Pre-Main Sequence (PMS) stars we used photometry extracted from the IRAC 3.6 and 4.5 μm long integration images. The 3.6 and 4.5 μm images are more sensitive, have a cleaner PSF, and appear to be less affected by nebular emission than the 8 μm image. We identified 161 additional sources, which are detected in both the 3.6 and 4.5 μm wavebands. Of these sources 113 are found to have NIR counterparts, and 6 sources are coincident with H_2 emission knots.

Table 2.1. Results of Near- & Mid-IR photometry of the Mid-infrared sources in SFO 38

Source SFO38	α_{2000} hh:mm:ss	δ_{2000} °:′:″	J mag	H mag	K_s mag	$F_{3.6}$ mJy	$F_{4.5}$ mJy	$F_{5.8}$ mJy	$F_{8.0}$ mJy	F_{24} mJy	Class	Comments
MIR-1	21:40:24.97	58:16:10.5	14.48±0.04	13.72± 0.05	13.42± 0.05	1.67±0.01	1.10±0.01	0.96±0.02	1.03±0.02	...	Trans.	JHK_s [c]
MIR-2	21:40:25.39	58:15:47.3	15.35±0.06	14.51± 0.07	14.15± 0.07	0.94±0.01	0.63±0.01	0.68±0.02	0.98±0.02	...	Trans.	...
MIR-3	21:40:25.84	58:15:26.1	15.62±0.07	14.80± 0.07	14.62± 0.10	0.52±0.01	0.31±0.00	0.23±0.02	0.07±0.02	...	III/S	...
MIR-4	21:40:26.84	58:14:51.8	16.26±0.10	15.67± 0.15	15.06± 0.15	0.32±0.00	0.20±0.00	0.17±0.02	0.11±0.02	...	III/S	...
MIR-5	21:40:27.29	58:14:21.14	14.30±0.04	13.30± 0.04	12.88± 0.04	6.22±0.05	...	...	...	...	II	Hα, X-ray
MIR-6	21:40:27.38	58:16:21.3	...	...	...	0.07±0.00	0.03±0.00	0.51±0.02	2.00±0.03	...	I/II	
MIR-7	21:40:27.97	58:15:14.1	14.51±0.04	13.41± 0.04	12.94± 0.04	3.89±0.02	3.52±0.02	3.44±0.03	4.33±0.03	...	II	Hα, J
MIR-8	21:40:28.35	58:16:42.3	11.59±0.03	10.78± 0.03	10.43± 0.02	23.62±0.07	14.18±0.04	10.94±0.06	6.63±0.04	...	III/S	
MIR-9	21:40:30.63	58:15:00.0	15.31±0.05	14.90± 0.07	14.70± 0.11	0.49±0.01	0.32±0.01	0.28±0.01	0.22±0.02	...	Trans.	
MIR-10	21:40:31.00	58:15:09.2	13.44±0.03	12.97± 0.04	12.79± 0.04	2.61±0.02	1.63±0.01	1.29±0.02	...	...	III/S	
MIR-11	21:40:31.56	58:17:55.1	14.03±0.03	12.89± 0.03	12.39± 0.03	6.93±0.03	6.93±0.03	9.15±0.06	15.17±0.12	20.46±0.08	II	Hα, X-ray, JHK_s
MIR-12	21:40:31.97	58:14:56.0	16.72±0.16	15.78± 0.15	15.41± 0.21	0.41±0.00	0.28±0.00	0.26±0.01	...	...	III/S	
MIR-13	21:40:32.23	58:16:53.6	14.13±0.03	12.44± 0.03	11.71± 0.03	10.82±0.04	6.39±0.02	6.54±0.05	7.36±0.05	...	Trans.	
MIR-14	21:40:32.46	58:13:47.2	13.40±0.03	12.83± 0.03	12.63± 0.03	2.78±0.03	...	1.30±0.05	...	...	III/S	
MIR-15	21:40:32.71	58:17:23.5	12.19±0.03	11.55± 0.03	11.36± 0.03	9.21±0.04	5.50±0.02	4.04±0.04	1.71±0.04	...	III/S	
MIR-16[b]	21:40:32.84	58:15:47.8	17.42±0.01	16.61±0.01	16.09±0.01	1.42±0.01	0.73±0.01	9.50±0.05	32.10±0.11	...	I/II	
MIR-17	21:40:33.64	58:14:44.6	16.54±0.14	15.81± 0.18	15.07± 0.00	0.21±0.00	0.13±0.00	0.11±0.01	0.16±0.02	...	Galaxy	
MIR-18	21:40:33.69	58:14:59.5	13.06±0.03	12.09± 0.03	11.75± 0.02	8.13±0.03	4.82±0.02	4.72±0.04	5.60±0.03	...	Trans.	
MIR-19	21:40:34.05	58:18:08.1	15.70±0.06	13.40± 0.04	12.30± 0.02	7.41±0.03	5.16±0.02	4.95±0.04	4.03±0.04	...	Trans.	
MIR-20	21:40:34.30	58:18:23.6	...	...	...	0.31±0.00	0.84±0.01	1.03±0.02	1.24±0.04	...	H$_2$	
MIR-21	21:40:34.59	58:16:11.4	...	...	...	0.08±0.00	0.05±0.00	1.33±0.03	...	...	III/S	
MIR-22[b]	21:40:34.76	58:15:20.9	17.70±0.01	16.68±0.01	16.04±0.01	0.25±0.01	0.34±0.01	...	...	...	III/S	
MIR-23	21:40:34.79	58:16:10.8	...	...	...	...	...	...	...	...	...	
MIR-24	21:40:35.02	58:18:22.2	16.48±...	15.72±...	14.90± 0.21	0.62±0.01	2.68±0.01	1.84±0.03	4.47±0.05	...	H$_2$	
MIR-25[b]	21:40:35.11	58:15:30.9	18.21±0.02	16.85±0.01	16.16±0.02	0.92±0.01	0.48±0.01	5.32±0.04	18.26±0.08	...	I/II	
MIR-26	21:40:35.20	58:14:05.0	13.11±0.03	12.61± 0.03	12.45± 0.03	3.55±0.02	2.40±0.01	1.59±0.02	0.84±0.02	...	III/S	

Table 2.1 (cont'd)

Source SFO38	α_{2000} hh:mm:ss	δ_{2000} °:′:″	J mag	H mag	K_s mag	$F_{3.6}$ mJy	$F_{4.5}$ mJy	$F_{5.8}$ mJy	$F_{8.0}$ mJy	F_{24} mJy	Class	Comments
MIR-27	21:40:35.68	58:18:21.3	16.55±…	15.73±…	14.79± 0.17	0.77±0.01	3.61±0.02	2.20±0.03	1.91±0.03	…	H$_2$	
MIR-28	21:40:36.46	58:15:23.6	15.97±0.10	14.73± 0.08	14.04± 0.07	2.27±0.01	1.43±0.01	6.68±0.04	19.47±0.08	…	I/II	
MIR-29	21:40:36.52	58:13:45.8	13.51±0.02	12.58± 0.03	12.24± 0.03	4.69±0.02	3.14±0.01	2.17±0.03	2.64±0.03	44.29±0.09	Trans.	Hα, X-ray
MIR-30	21:40:36.65	58:18:23.0	17.12±…	15.18±0.10	13.93±0.07	1.84±0.01	1.55±0.01	1.42±0.03	1.21±0.03	…	II	
MIR-31	21:40:36.88	58:14:37.8	11.90±0.02	10.89± 0.03	10.23± 0.02	54.30±0.14	48.79±0.10	38.25±0.12	34.45±0.10	39.36±0.07	II	Hα, X-ray
MIR-32	21:40:37.02	58:15:02.9	14.27±0.03	13.28± 0.04	12.82± 0.03	4.01±0.02	3.07±0.01	2.86±0.03	3.87±0.04	…	II	Hα, K_s
MIR-33	21:40:37.16	58:15:46.6	17.01±…	15.80±0.16	14.55±0.10	1.33±0.01	1.28±0.01	0.71±0.03	…	…	III/S	
MIR-34[b]	21:40:37.54	58:15:39.3	18.07±0.02	16.98±0.01	16.24±0.02	0.49±0.01	0.77±0.01	1.05±0.03	1.63±0.04	17.15±0.06	0/I	
MIR-35	21:40:39.05	58:16:03.3	…	…	…	0.41±0.01	1.04±0.01	2.19±0.03	…	…	H$_2$	
MIR-36[a]	21:40:39.60	58:16:09.0	…	>17.6	15.14±0.16	10.47±0.03	36.11±0.08	59.09±0.17	82.89±0.22	239.10±0.10	0/I	X-ray
MIR-37	21:40:39.80	58:16:24.9	…	…	…	0.53±0.01	0.76±0.01	1.15±0.02	1.39±0.03	…	0/I	
MIR-38	21:40:39.84	58:18:34.8	18.29±…	15.30±0.12	13.36±0.04	6.88±0.03	8.19±0.03	9.95±0.06	13.49±0.06	30.69±0.07	II	X-ray
MIR-39	21:40:40.15	58:16:18.2	…	…	…	1.36±0.01	2.65±0.01	3.24±0.04	4.25±0.05	…	0/I	
MIR-40	21:40:40.43	58:18:26.1	18.28±…	15.64±0.15	13.85 ±0.06	2.35±0.01	2.05±0.01	1.64±0.03	0.76±0.02	…	III/S	
MIR-41	21:40:40.96	58:16:12.0	17.55±…	15.89±…	13.59± 0.06	13.04±0.04	23.41±0.06	29.43±0.10	42.25±0.15	…	0/I	
MIR-42	21:40:40.98	58:16:52.4	17.93±…	15.34±0.14	13.93±0.06	1.41±0.01	1.04±0.01	0.83±0.02	0.37±0.03	…	III/S	
MIR-43	21:40:41.07	58:13:58.9	12.96±0.02	12.08± 0.03	11.77± 0.02	6.80±0.02	4.58±0.02	3.19±0.03	1.84±0.03	…	III/S	Hα, X-ray
MIR-44	21:40:41.10	58:17:54.1	14.20±0.04	13.46± 0.04	13.21± 0.03	1.89±0.01	1.14±0.01	0.73±0.02	0.37±0.02	…	III/S	
MIR-45	21:40:41.14	58:15:11.2	12.97±0.03	11.61± 0.04	10.68± 0.02	66.38±0.17	65.98±0.14	81.84±0.21	124.60±0.31	194.40±0.09	II	Hα, X-ray
MIR-46	21:40:41.27	58:17:14.2	…	…	…	0.06±0.00	0.03±0.00	0.65±0.02	2.61±0.03	…	I/II	
MIR-47	21:40:41.40	58:14:17.5	15.48±…	15.50±0.12	14.63±0.00	0.34±0.00	0.21±0.00	0.16±0.01	0.10±0.02	…	III/S	
MIR-48	21:40:41.43	58:16:37.8	18.30±…	15.60±0.15	12.79±0.03	51.81±0.14	109.40±0.20	158.50±0.34	199.60±0.44	1362.00±0.26	0/I	Hα, X-ray
MIR-49	21:40:41.54	58:14:25.5	13.65±0.03	12.62± 0.03	12.17± 0.03	8.70±0.03	7.38±0.03	6.65±0.04	6.42±0.04	…	II	X-ray
MIR-50	21:40:41.71	58:16:12.6	…	…	…	10.84±0.04	78.01±0.16	128.00±0.29	137.00±0.34	1871.00±0.31	0/I	X-ray, JHK_s
MIR-51	21:40:41.89	58:15:23.0	15.68±0.09	14.30± 0.06	13.65± 0.05	2.88±0.02	2.30±0.01	3.75±0.04	8.33±0.06	…	I/II	X-ray, JHK_s
MIR-52	21:40:41.96	58:13:49.1	15.50±0.06	15.00± 0.09	14.98± 0.14	0.40±0.00	0.27±0.00	0.19±0.01	0.10±0.02	…	III/S	

Table 2.1 (cont'd)

Source SFO38	α_{2000} hh:mm:ss	δ_{2000} °:′:″	J mag	H mag	K_s mag	$F_{3.6}$ mJy	$F_{4.5}$ mJy	$F_{5.8}$ mJy	$F_{8.0}$ mJy	F_{24} mJy	Class	Comments
MIR-53	21:40:42.35	58:18:40.1	...	...	...	0.48±0.00	2.16±0.01	1.99±0.03	1.26±0.02	...	H_2	
MIR-54	21:40:42.77	58:16:01.1	...	...	...	20.16±0.06	75.86±0.15	113.50±0.27	117.60±0.31	2484.00±0.38	I	X-ray
MIR-55[a]	21:40:43.32	58:17:16.5	...	>17.6	15.31±0.11	1.65±0.01	2.23±0.01	2.72±0.03	4.31±0.03	145.40±0.08	0/I	
MIR-56	21:40:43.34	58:18:42.6	16.32±0.13	14.42±0.05	13.55±0.04	1.93±0.01	1.39±0.01	0.91±0.02	0.26±0.03	...	III/S	
MIR-57	21:40:43.62	58:16:18.8	17.89±...	16.09±...	13.51±0.07	33.21±0.09	68.55±0.14	82.72±0.21	91.38±0.24	...	0/I	X-ray
MIR-58	21:40:43.65	58:14:18.4	15.55±0.08	15.05±0.10	14.89±0.14	0.41±0.00	0.28±0.00	0.19±0.01	0.14±0.02	...	Trans.	
MIR-59	21:40:44.23	58:16:52.2	...	...	...	1.36±0.01	4.43±0.02	9.13±0.05	10.52±0.06	100.90±0.07	0/I	
MIR-60	21:40:44.26	58:14:12.4	15.57±0.06	15.00±0.09	14.69±0.12	0.45±0.00	0.30±0.00	0.22±0.01	0.09±0.02	...	III/S	
MIR-61	21:40:44.31	58:15:13.2	16.05±0.10	14.59±0.07	13.60±0.05	3.78±0.02	4.10±0.02	7.89±0.05	15.74±0.08	...	I/II	X-ray, JHK_s
MIR-62	21:40:44.64	58:17:04.9	17.83±...	15.75±0.15	14.62±0.10	2.16±0.01	2.38±0.01	2.51±0.03	3.06±0.03	...	II	
MIR-63	21:40:44.82	58:16:05.0	15.86±...	14.28±0.06	12.89±0.05	7.08±0.03	7.17±0.03	6.83±0.05	7.25±0.05	...	II	X-ray, K_s
MIR-64	21:40:44.83	58:15:03.3	14.62±0.04	13.35±0.04	12.66±0.03	5.64±0.02	5.23±0.02	7.28±0.05	12.94±0.06	...	I/II	Hα, X-ray
MIR-65	21:40:44.89	58:17:47.7	...	...	...	0.42±0.00	2.56±0.01	2.01±0.02	2.29±0.03	...	H_2	
MIR-66[b]	21:40:45.11	58:15:24.0	18.46±0.02	16.74±0.01	15.71±0.01	0.59±0.01	0.44±0.01	1.73±0.03	5.26±0.05	...	I/II	
MIR-67	21:40:45.16	58:15:59.6	...	...	...	5.73±0.02	9.26±0.03	11.46±0.06	11.78±0.07	...	I	X-ray
MIR-68[b]	21:40:45.24	58:16:41.3	17.38±0.01	16.29±0.01	15.53±0.01	0.43±0.01	0.42±0.01	0.41±0.01	0.68±0.02	...	Galaxy	
MIR-69	21:40:45.29	58:16:53.3	...	...	...	0.53±0.01	0.61±0.01	0.60±0.02	...	...	III/S	
MIR-70[b]	21:40:45.41	58:16:45.5	20.38±0.15	17.48±0.02	15.96±0.01	0.33±0.00	0.27±0.01	0.48±0.02	1.14±0.02	...	Galaxy	
MIR-71	21:40:45.48	58:15:11.5	14.65±0.05	13.71±0.06	13.11±0.04	3.17±0.02	2.61±0.01	3.41±0.04	5.73±0.05	...	I/II	X-ray, K_s
MIR-72	21:40:45.50	58:16:02.6	15.68±0.09	13.73±0.06	12.85±0.04	4.13±0.02	3.15±0.02	2.74±0.03	2.88±0.03	...	II	X-ray
MIR-73	21:40:45.76	58:15:48.9	...	...	...	2.71±0.02	7.27±0.03	10.79±0.06	11.29±0.07	...	I	X-ray
MIR-74	21:40:45.82	58:17:43.0	...	...	...	0.36±0.00	0.92±0.01	1.16±0.02	1.38±0.02	...	H_2	
MIR-75	21:40:46.22	58:17:40.2	...	...	...	0.34±0.00	0.71±0.01	1.20±0.02	1.53±0.02	...	H_2	
MIR-76	21:40:46.46	58:15:23.0	12.81±0.03	11.95±0.03	11.65±0.02	8.66±0.03	5.35±0.02	5.25±0.04	7.74±0.07	...	Trans.	X-ray, Hα
MIR-77	21:40:46.86	58:15:33.4	15.30±0.06	13.55±0.05	12.63±0.04	5.80±0.02	4.05±0.02	5.16±0.04	10.41±0.08	...	Galaxy	X-ray
MIR-78	21:40:47.35	58:16:37.3	17.08±...	16.14±0.24	14.63±0.10	1.00±0.01	0.75±0.01	0.59±0.02	0.36±0.02	...	III/S	

Table 2.1 (cont'd)

Source SFO38	α_{2000} hh:mm:ss	δ_{2000} °:′:″	J mag	H mag	K_s mag	$F_{3.6}$ mJy	$F_{4.5}$ mJy	$F_{5.8}$ mJy	$F_{8.0}$ mJy	F_{24} mJy	Class	Comments
MIR-79	21:40:47.43	58:17:39.1	11.53±0.03	9.98± 0.03	9.37± 0.02	72.47±0.17	46.36±0.10	34.42±0.11	20.21±0.07	...	III/S	
MIR-80	21:40:48.00	58:15:37.6	13.89±0.03	12.95± 0.03	12.67± 0.03	4.72±0.02	3.39±0.02	5.77±0.04	11.90±0.06	...	I/II	Hα, X-ray
MIR-81	21:40:48.52	58:16:37.1	16.18±0.09	14.95± 0.08	14.46± 0.08	0.71±0.01	0.46±0.01	0.38±0.02	0.62±0.02	...	Galaxy	K_s
MIR-82	21:40:48.58	58:16:00.9	15.88±0.09	13.45± 0.04	11.88± 0.02	30.35±0.08	37.01±0.08	43.12±0.13	61.94±0.17	167.10±0.09	II	JH
MIR-83	21:40:48.84	58:16:22.8	16.02±0.12	15.25± 0.13	14.46± 0.08	0.61±0.01	0.43±0.01	0.25±0.02	...	...	III/S	
MIR-84	21:40:48.87	58:15:10.9	15.64±0.06	15.04± 0.08	14.56± 0.09	0.77±0.01	0.62±0.01	0.75±0.02	1.34±0.03	...	I/II	Hα, JK_s
MIR-85	21:40:49.05	58:17:19.4	15.79±0.08	13.83± 0.05	12.92± 0.02	3.32±0.02	2.19±0.01	1.75±0.02	1.18±0.02	...	Trans.	J
MIR-86	21:40:49.06	58:17:09.3	14.14±0.03	12.86± 0.04	12.13± 0.02	13.88±0.05	14.57±0.04	15.54±0.07	17.83±0.07	17.99±0.05	II	Hα, X-ray, K_s
MIR-87	21:40:49.29	58:14:11.3	13.52±0.03	12.66± 0.03	12.35± 0.02	3.87±0.02	2.44±0.01	1.66±0.02	0.99±0.02	...	III/S	
MIR-88	21:40:49.67	58:17:37.3	17.13±0.23	14.99± 0.09	14.23± 0.07	1.07±0.01	0.73±0.01	0.60±0.02	0.36±0.02	...	III/S	
MIR-89[b]	21:40:51.07	58:16:24.3	17.80±0.01	16.70±0.01	16.09±0.01	0.11±0.00	0.08±0.00	0.11±0.02	0.23±0.02	...	Galaxy	
MIR-90	21:40:51.23	58:16:38.9	14.23±0.03	13.76± 0.04	13.61± 0.04	1.26±0.01	0.78±0.01	0.57±0.02	0.53±0.02	...	Trans.	HK
MIR-91	21:40:51.81	58:16:29.1	15.70±0.06	14.45± 0.06	13.93± 0.07	1.19±0.01	0.74±0.01	0.60±0.02	0.54±0.02	...	Trans.	HK
MIR-92	21:40:51.90	58:17:01.6	...	...	...	0.36±0.00	0.33±0.00	0.20±0.02	...	...	III/S	
MIR-93[b]	21:40:51.97	58:16:23.6	19.21±0.06	17.47±0.01	16.39±0.01	0.16±0.00	0.10±0.00	0.23±0.02	0.65±0.02	...	Galaxy	
MIR-94	21:40:52.26	58:17:46.0	15.68±0.05	14.56± 0.05	14.06± 0.06	0.94±0.01	0.65±0.01	0.59±0.02	0.48±0.03	...	Trans.	
MIR-95	21:40:52.98	58:18:01.1	15.29±0.05	14.59± 0.06	14.22± 0.07	0.84±0.01	0.53±0.01	0.54±0.03	0.34±0.03	...	III/S	
MIR-96	21:40:53.12	58:14:57.4	14.77±0.06	14.25± 0.07	13.95± 0.07	0.84±0.01	0.54±0.01	0.38±0.02	0.37±0.03	...	Trans.	
MIR-97	21:40:53.42	58:14:51.9	15.50±0.06	14.88± 0.09	14.74± 0.11	0.44±0.00	0.31±0.01	0.23±0.01	0.20±0.02	...	Trans.	
MIR-98	21:40:53.68	58:16:41.2	...	...	...	0.25±0.00	0.71±0.01	0.79±0.02	0.83±0.02	...	H$_2$	
MIR-99	21:40:55.68	58:15:50.8	...	...	...	0.36±0.00	0.14±0.00	2.69±0.03	9.65±0.05	...	I/II	
MIR-100	21:40:55.87	58:14:16.3	14.18±0.03	13.61± 0.04	13.39± 0.04	...	0.87±0.02	...	0.45±0.03	...	III/S	
MIR-101	21:40:55.88	58:15:34.8	...	...	...	0.25±0.00	0.32±0.00	0.41±0.02	0.71±0.02	...	Galaxy	
MIR-102	21:40:55.93	58:17:07.8	14.45±0.03	13.19± 0.04	12.76± 0.03	3.21±0.01	2.01±0.01	1.39±0.02	0.99±0.02	...	Trans.	
MIR-103	21:40:57.04	58:16:56.8	16.61±0.13	15.92± 0.21	16.22± 0.00	0.42±0.01	0.34±0.00	0.40±0.02	1.19±0.03	...	Galaxy	
MIR-104	21:40:57.06	58:16:29.0	14.73±0.03	13.00± 0.03	12.24± 0.02	6.10±0.02	4.11±0.02	2.87±0.03	1.96±0.03	...	Trans.	

Table 2.1 (cont'd)

Source SFO38	α_{2000} hh:mm:ss	δ_{2000} $\circ$:$'$:$''$	J mag	H mag	K_s mag	$F_{3.6}$ mJy	$F_{4.5}$ mJy	$F_{5.8}$ mJy	$F_{8.0}$ mJy	F_{24} mJy	Class	Comments
MIR-105	21:40:57.33	58:16:41.7	16.64±...	15.41±...	14.55± 0.13	0.79±0.01	1.18±0.01	2.90±0.03	6.34±0.04	...	H_2	
MIR-106	21:40:57.50	58:14:43.6	15.00±0.04	14.66± 0.07	14.34± 0.09	...	0.43±0.01	0.25±0.03	0.15±0.02	...	III/S	
MIR-107	21:40:58.03	58:15:12.1	15.06±0.05	14.50± 0.07	14.12± 0.08	0.70±0.01	0.46±0.01	0.30±0.02	0.21±0.02	...	Trans.	
MIR-108	21:40:58.45	58:16:20.5	13.11±0.03	12.44± 0.03	12.02± 0.03	5.93±0.03	3.77±0.02	3.13±0.03	2.52±0.03	...	Trans.	
MIR-109	21:40:58.53	58:15:00.3	12.15±0.03	11.26± 0.03	10.96± 0.02	...	8.34±0.03	5.73±0.05	3.46±0.03	...	III/S	
MIR-110	21:40:59.71	58:17:33.3	12.69±0.02	11.25± 0.03	10.59± 0.02	24.86±0.17	...	10.77±0.13	...	...	III/S	

[a] JHK_s photometry from Nisini et al. (2001)

[b] JHK_s photometry from Beltrán et al. (2009)

[c] Variable in $J/H/K_s$

2.4.2 Classification of YSOs Based on Near- and Mid-infrared Colors

In regions of high obscuration like SFO 38, which has a visual extinction of up to 20 mag, mid-infrared color indices provide an ideal tool for identifying YSOs and classify them according to their phases of PMS evolution (Getman et al., 2007). Here we use several color indices generated using the *Spitzer* IRAC and MIPS data to characterize the evolutionary stages of the MIR sources detected in SFO 38.

Stern et al. (2005) demonstrated that (a) normal star-forming galaxies and narrow-line AGNs with increasing 5.8 and 8.0 μm and (b) broad-line AGNs with red, nonstellar SEDs, result in colors which are very similar to bona-fide YSOs. Thus prior to identifying PMS sources based on the color indices it is necessary to inspect deep IRAC images for contamination due to the extragalactic sources. Gutermuth et al. (2009) have extensively discussed the criteria for identifying such extragalactic objects in the IRAC color-color diagrams. Using the criteria given in the appendix of their paper, we identify MIR-2, 17, 68, 70, 75, 81, 84, 89, 101 and 103 as AGNs and MIR-77, 81, 93 and 103 as galaxies strongly emitting in the PAH bands. Of these sources, MIR-17, 89 and 103 satisfy most of the criteria for extragalactic objects. The profiles of sources in the R-band is typically quite a good indicator of whether the source is actually extragalactic or stellar. However all the sources in SFO 38 which satisfy the criteria mentioned above are extremely faint so that with the exception of MIR-2, these sources though visible are not detected clearly enough in the R-band so that the intensity profile can be studied. Further, none of the sources is detected in the MIPS 24 μm image either. The R-band profile of MIR-2 appears to be stellar with a faint companion on one side and MIR-84 is associated with an Hα emission star, so we do not identify both these sources as extragalactic. In the absence of any conclusive evidence we presently assume the sources identified by the empirical criteria as above to be extragalactic.

The 4.5 μm IRAC band of *Spitzer* covers many of the H$_2$ pure rotational lines, as a result of which this band records a large excess of emission at the position of the unresolved blobs of shocked emission from high velocity outflows which interact with the molecular cloud. Using the empirical criteria outlined by Gutermuth et al. (2009) here we flag the sources MIR-24, 27, 53, 65 and 98 as possible features due to shocked H$_2$ emission. Based on 2.12 μm H$_2$ integrated line emission Beltrán et al. (2009) identified as many as 97 emission features possibly created by H$_2$ excitation by shocks driven by outflows powered by YSOs. We find that 10 out of the 110 MIR sources that we have identified are associated with such H$_2$ knots. These include the sources MIR-20, 24, 27, 35, 53, 65, 74, 75, 98 and 105. Thus the color indices for 5 out of the 10 sources are consistent with the observed association with H$_2$ knots. The source MIR-75 which also satisfied the criteria for being an extragalactic object is thus identified as a H$_2$ knot.
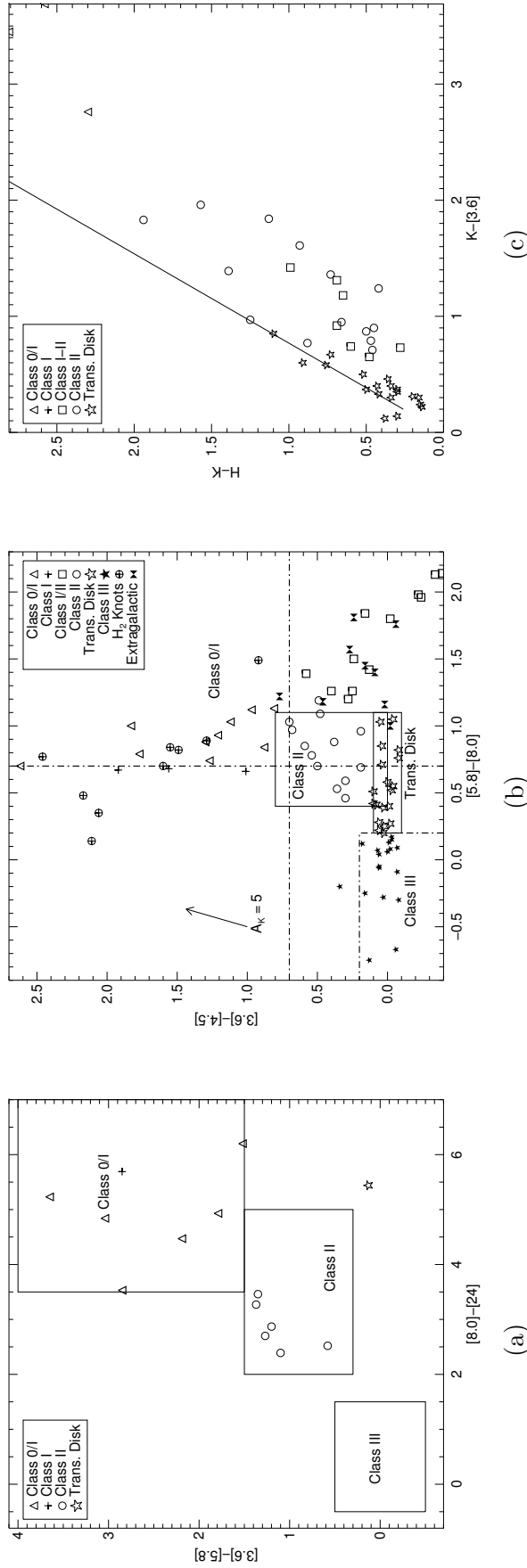
Figure 2.4 Color-color diagrams for all MIR sources. Approximate classification criteria adopted from Megeath et al. (2004), Fang et al. (2009) and Muzerolle et al. (2004b) are shown in panels *a* and *b*. (a) MIR color-color diagram based on *Spitzer* 3-band IRAC and MIPS photometry and (b) 4 band IRAC color-color diagram. Dashed lines in the two panels are taken from Hartmann et al. (2005). Reddening vector corresponding to the extinction laws given by the fitted function from Indebetouw et al. (2005) is shown in (*b*). The dashed lines $[3.6]-[4.5] = 0.7$, $[4.5]-[5.8] = 0.7$ and $[5.8]-[8.0] = 0.7$ discriminate Class II sources from Class I/0 sources, and $[3.6]-[4.5] = 0.2$, $[4.5]-[5.8] = 0.2$ and $[5.8]-[8.0] = 0.2$ discriminate Class III from Class II and Transitional Disk sources. (c) NIR and *Spitzer* MIR color-color diagram. *Solid* line is the reddening vector due to interstellar extinction (Tapia, 1981). Sources to the right of the reddening vector are YSOs with NIR excess.

Figure 2.4 presents color-color diagrams of NIR, IRAC and MIPS 24 μm sources detected in the SFO 38 globule. We have used several criteria (shown as dashed lines and boxes in Figure 2.4) to identify the potential YSOs using these color-color diagrams.

The most stringent classification scheme uses the IRAC ([3.6]–[5.8]) colors and the [8]–[24] IRAC and MIPS color. At 24 μm the reddening due to extinction is small and the photospheric colors are very close to zero for all spectral types (Muzerolle et al., 2004b). Therefore the [8]–[24] color is very sensitive to infrared excess, but of course not all young stars are bright enough to be detected at 24 μm. Using this color-color diagram we find fourteen sources with infrared excess (Figure 2.4 (*left*)). We identify MIR-34, 36, 48, 50, 54, 55 and 59 as Class 0/I sources, while MIR-11, 31, 38, 45, 82 and 86 are within the Class II regime and MIR-29 which has a large [8.0]–[24] color excess and very small value for the [3.6]-[5.8] color is identified as a transition disk object. Jørgensen et al. (2007) predicted sources with [3.6]–[4.5]>1.0 and [8]–[24] > 4.5 to be YSOs driving molecular outflows. We find that the sources MIR-34, 48, 50, 54, and 59, all of which have been identified as Class 0/I objects also satisfy the criteria for being sources driving outflows.

Figure 2.4 (*middle*) presents the [3.6]–[4.5] vs [5.8]–[8.0] color-color plot for the sources detected in all the IRAC bands. Sources with the colors of stellar photospheres are centered at ([3.6]–[4.5],[5.8]–[8.0])=(0,0) and include foreground and background stars as well as diskless (Class III) pre-main sequence stars. Sources which satisfy the criteria $-0.1 \leq$ [3.6]–[4.5] ≤ 0.1 and $0.2 \leq$ [5.8]–[8.0] ≤ 1.1 are classified as the transitional disk objects (Fang et al., 2009) which also do not have any NIR color excess. The box outlined in Figure 2.4 (*middle*), defines the location of Class II objects (Megeath et al., 2004; Allen et al., 2004), i.e. sources whose colors can be explained by young, low-mass stars surrounded by disks. Hartmann et al. (2005) have shown from their observations of young stars in the Taurus-Auriga complex that Class 0/I protostars require [3.6]–[4.5]> 0.7 and [5.8]–[8.0]> 0.7. With the exception of MIR-29, the classes derived for the sources identified in the MIPS 24 μm band and plotted in Fig. 2.4(*left*) are completely consistent with the classes derived from the [3.6]–[4.5] vs [5.8]–[8.0] color-color plot. We identify 10 of the MIR sources as being associated with H_2 knots, this includes MIR-75, which otherwise satisfies the criteria for extragalactic objects. We also plot NIR and *Spitzer* MIR color-color diagram of the identified YSOs and transitional Disk objects in Figure 2.4 (*right*).

Table 2.1 presents a summary of classification of the MIR sources based on the color-color diagrams presented here. We have additionally looked into the [3.6]–[5.8] vs [4.5]–[8.0] color-color diagram and found that the Classes derived from this diagram are consistent with the classes derived based on the color-color diagrams presented here. For most sources it was possible to arrive at a unique Class based on all three color-color diagrams. For all sources the Class derived based on at least two color-color diagrams match.

Use of the more sensitive long integration 3.6 and 4.5 μm images in combination with

Table 2.2. Coordinates and flux densities of NIR & IRAC 3.6/4.5 μm PMS sources in SFO 38

Source SFO38	α_{2000}	δ_{2000}	J	H	K_s	$F_{3.6}$ mJy	$F_{4.5}$ mJy
NIR-1	21:40:34.36	58:16:19.2	20.88±...	18.12±0.03	16.68±0.02	15.73±0.03	15.38±0.03
NIR-2	21:40:36.46	58:16:28.7	20.84±...	19.31±0.10	17.14±0.03	15.23±0.02	14.75±0.02
NIR-3	21:40:37.57	58:16:01.2	20.80±...	19.98±...	17.35±...	15.22±0.03	14.29±0.02
NIR-4	21:40:38.17	58:15:32.7	20.87±...	18.32±0.03	16.72±0.02	14.84±0.02	14.59±0.02
NIR-5	21:40:39.53	58:15:46.9	...	...	...	14.22±0.01	13.72±0.01
NIR-6	21:40:39.65	58:15:06.6	16.59±0.01	15.88±0.01	15.52±0.01	14.07±0.01	13.82±0.01
NIR-7	21:40:42.81	58:15:45.3	16.29±0.00	15.38±0.00	14.77±0.00	13.91±0.01	13.27±0.01
NIR-8	21:40:44.15	58:15:49.6	...	...	...	15.78±0.04	13.83±0.01
NIR-9	21:40:44.57	58:15:51.6	15.97±0.00	15.23±0.00	14.71±0.00	14.28±0.02	13.68±0.01
NIR-10	21:40:45.85	58:15:40.6	18.70±0.03	17.09±0.01	16.01±0.01	14.68±0.02	14.18±0.02
NIR-11	21:40:48.28	58:16:18.8	18.17±0.02	17.16±0.01	16.40±0.02	15.63±0.03	15.24±0.03
NIR-12	21:40:50.55	58:16:01.8	20.84±...	19.65±0.10	17.55±0.03	15.65±0.03	15.29±0.03
NIR-13	21:40:51.14	58:17:01.5	20.86±...	18.74±0.05	17.23±0.04	15.99±0.03	15.68±0.04

2MASS data (following a classification scheme involving the K_s–[3.6] and [3.6]–[4.5] colors) yields an additional 113 sources, 11 of which are PMS objects. Since the long integration 3.6 and 4.5 μm images go deeper and are less affected by extinction than the 2MASS survey, we also checked how many of these IRAC sources which have no 2MASS associations are likely to be PMS stars. Among the 48 remaining sources which have no NIR counterparts, following the arguments of Mookerjea et al. (2009) if we use the color criterion, [3.6]-[4.5] $\geq$ 0.2, we obtain 8 sources. However 6 of these 8 sources are actually associated with H_2 emission knots as detected by Beltrán et al. (2009). Table 2.2 lists the 13 PMS candidates identified on the basis of NIR and 3.6 and 4.5 μm magnitudes.

Excluding the H_2 knots and the possible extragalactic objects we identify 10 Class 0/I sources, 3 Class I sources, 13 Class I/II sources (occupying the top-left and bottom-right corners), 14 Class II sources and 19 transitional disk objects in SFO 38. Thus we find a total of 40 YSOs (Classes 0/I/II) and 13 PMS candidates based on MIR color indices. We note that 13 Class I/II objects and 19 Transitional Disk objects are $\sim$ 30% of the selected YSOs and show noticeable color excess only beyond 6 μm.

2.4.3 Hα Emission of SFO 38 and Spatial Distribution of YSOs

Sugitani et al. (1991) classified SFO 38 as a B type BRC powered by O6.5 star HD 206267. The bright rim structure is quite prominent in the continuum subtracted Hα line image of SFO 38 in Figure 2.5. The Hα emission nebulosity of the bright-rim of the globule is asymmetric with respect to the geometric axis of the globule as well as the direction of the adopted ionizing source HD 206267. The ionized rim appears to be brighter towards the east and rather diffuse towards the western edge, facing HD 206267. The Hα intensity distribution of the diffuse material in between the bright-rim and the ionizing star also
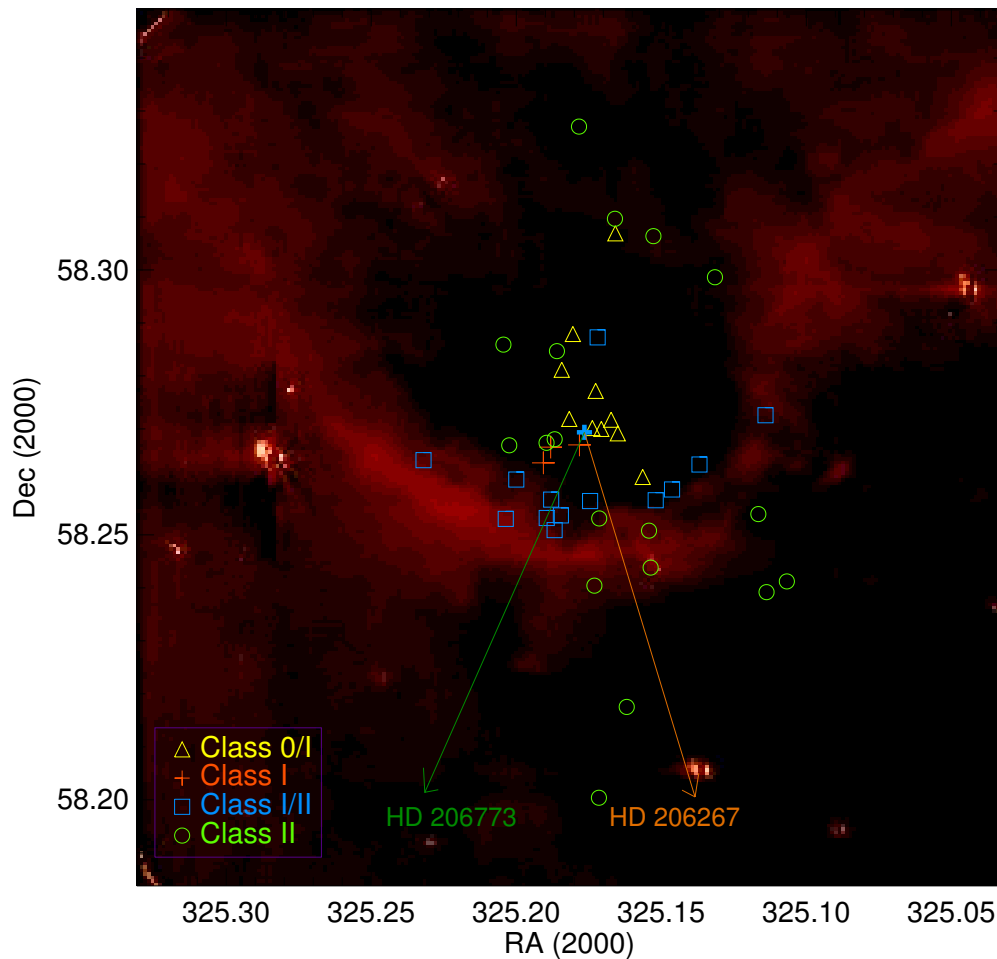
Figure 2.5 Continuum subtracted Hα emission line image of SFO 38. Class 0/I to Class II YSOs are overplotted with different symbols. The directions towards HD 206267 and HD 206773 are marked with two different *arrows*.

show similar kind of asymmetric distribution as that of the bright-rim. We, therefore, searched for other massive O and B type stars in the surrounding region that can produce the relatively brighter Hα emission on the eastern side of the globule. We find a B0V type (Jaschek & Egret, 1982) star HD 206773 which is situated on the symmetry axis of the left side of the bright-rim at a projected distance of ~ 7.6 pc from SFO 38. de Zeeuw et al. (1999) tagged HD 206773 as a member of Cep OB2 association. The distance towards the star is between 550–1000 pc, adopting the parallax measurement and the associated error (van Leeuwen, 2007) which is consistent with the distance of SFO 38. The number of ionizing photons emitted per second by a B0V star is $\sim 10^{48.02}$ (Sternberg et al., 2003) and using $n_H \simeq 10^7 \ m^{-3}$ for number density of hydrogen in the interior of the H II region IC 1396, the Strömgren radius would be ~ 8.5 pc which suggests that HD 206773 could be a potential ionizing source for SFO 38. Fig. 2.5 shows the distribution of the YSOs and the directions toward HD 206267 and HD 206773 on the Hα line image. We find that most of Hα emitting Class II objects lie within the bright-rim. Class I/II objects are situated

behind the Class II objects in the intermediate region between the bright-rim and the dense portion of the globule. All the Class 0/I and Class I objects are situated well within the dense core part of the globule. There is no Class 0/I to Class I/II YSO which is situated before the ionized rim. The YSOs appear to have elongated distribution to the east and west sides of the bright rim with two different axes of elongation.

2.4.4 Additional YSO Candidates Based on Hα Emission

Hα emission surveys are very useful to identify low mass (< 2 M$\odot$) Classical T Tauri Stars (CTTS) in young star forming regions as the Hα emission is due to the accretion of circumstellar material in YSOs. These observations also detect a fraction of Weak-lined T Tauri stars with weak Hα emission which is believed to arise from enhanced chromospheric activities. Based on Hα emission, we searched for the additional YSO candidates available in the literature outside the field of view of *Spitzer* observations to complement the list of YSOs around SFO 38. Many of the candidate YSOs in and around SFO 38 were found during Hα objective prism survey by Ogura et al. (2002); Ikeda et al. (2008). A total of 14 out of the 17 Hα emission line sources (Ogura et al., 2002; Ikeda et al., 2008) are situated within the field of view of IRAC. We consider the rest of the Hα emission line sources *viz.,* [OSP2002] BRC 38 1, [OSP2002] BRC 38 16, and [OSP2002] BRC 38 17 as YSO candidates. We also find 4 Hα emission line sources near SFO 38 in the catalog of point-source Hα emission-line objects selected from the INT/WFC Photometric Hα Survey (IPHAS) of the northern Galactic plane (Witham et al., 2008). We identify IPHAS J214027.32+581421.3 as [OSP2002] BRC 38 2, IPHAS J214036.90+581437.9 as [OSP2002] BRC 38 6, IPHAS J214041.23+581158.5 as [GFG2007] 64. Thus, we also consider [GFG2007] 64 and IPHAS J214042.81+581937.4 as YSO candidates.

2.4.5 Optical and NIR variability

Out of the 115 sources (110 MIR + 5 Hα emission sources) mentioned in Secs. 2.4.2, 2.4.4 and 2.4.6 we detect a total of *39* sources in B, *46* sources in V, *51* source in R and *63* source in I bands. VR magnitudes of all the sources observed on 17th July, 2009 and detected in in V band are presented in Table 2.3. BI magnitudes of all the sources observed on 15th September, 2009 and detected in in B band are presented in Table 2.4. BVI magnitudes of all the sources observed on 23rd August, 2009 and detected in V band are presented in Table 2.5. We do not detect the optical counterparts of the 13 PMS candidates listed in Table 2.2. Photometric variability, a very common characteristic of YSOs, can happen due to various physical processes *viz.,* variation in stellar spots or variable obscuration which affect the emission from its photosphere. Since we have BVI observations separated by several months, we have also looked for the variability in the BVI bands for all the sources. The median variability in BVI bands are ~ 0.04 mag which is also indicative of

Table 2.3. *VR* photometry of MIR sources in SFO 38 on 17th July, 2009

Source	V	R	Source	V	R
MIR-1	18.28±0.005	17.18±0.004	MIR-58	18.82±0.007	17.86±0.005
MIR-2	18.93±0.005	17.88±0.008	MIR-60	19.12±0.005	18.07±0.005
MIR-3	19.60±0.007	18.37±0.006	MIR-64	20.48±0.017	18.77±0.016
MIR-4	20.45±0.017	19.15±0.007	MIR-76	17.18±0.002	15.90±0.002
MIR-5	19.22±0.005	17.77±0.004	MIR-79	18.59±0.006	16.52±0.002
MIR-7	19.43±0.006	17.90±0.004	MIR-80	19.67±0.013	17.90±0.006
MIR-8	15.77±0.001	14.55±0.001	MIR-86	20.78±0.019	18.85±0.009
MIR-9	18.54±0.008	17.60±0.005	MIR-87	17.72±0.003	16.50±0.002
MIR-10	16.10±0.001	15.29±0.001	MIR-90	16.87±0.002	16.04±0.001
MIR-11	19.58±0.012	17.94±0.007	MIR-95	20.17±0.011	18.71±0.009
MIR-14	16.28±0.001	15.38±0.001	MIR-96	17.86±0.002	16.94±0.003
MIR-15	15.29±0.001	14.33±0.001	MIR-97	18.66±0.006	17.76±0.005
MIR-18	17.62±0.003	16.30±0.002	MIR-100	16.92±0.002	16.03±0.001
MIR-26	16.06±0.001	15.20±0.001	MIR-102	20.26±0.014	18.61±0.009
MIR-29	18.48±0.005	16.94±0.002	MIR-106	17.79±0.004	16.96±0.003
MIR-31	15.76±0.001	14.60±0.001	MIR-107	18.14±0.005	17.22±0.003
MIR-32	19.48±0.006	18.01±0.007	MIR-108	17.34±0.004	16.13±0.003
MIR-43	17.60±0.002	16.21±0.001	MIR-109	16.21±0.001	15.00±0.001
MIR-44	17.69±0.004	16.57±0.001	MIR-110	19.92±0.010	17.76±0.004
MIR-45	19.63±0.009	18.10±0.012	BRC 38 1	20.05±0.014	18.24±0.009
MIR-47	19.89±0.009	18.76±0.005	MIR 38 17	20.32±0.017	18.65±0.005
MIR-49	18.58±0.006	17.04±0.003	GFG 64	17.50±0.004	16.19±0.001
MIR-52	18.34±0.005	17.52±0.003	IPHAS	20.23±0.012	18.28±0.009

Table 2.4. *BI* photometry of MIR sources in SFO 38 on 15th September, 2009

Source	B	I	Source	B	I
MIR-1	19.88±0.010	16.07±0.003	MIR-49	20.80±0.029	15.80±0.002
MIR-2	20.53±0.014	16.88±0.004	MIR-52	19.57±0.008	16.72±0.005
MIR-3	21.67±0.028	17.19±0.003	MIR-58	20.23±0.015	16.94±0.005
MIR-5	20.11±0.007	16.56±0.002	MIR-60	20.80±0.026	17.08±0.006
MIR-7	21.61±0.024	16.39±0.002	MIR-76	19.04±0.005	14.56±0.001
MIR-8	17.78±0.002	13.38±0.001	MIR-79	21.50±0.065	14.59±0.001
MIR-9	20.00±0.017	16.66±0.005	MIR-80	21.70±0.035	16.01±0.003
MIR-10	17.31±0.001	14.52±0.001	MIR-87	19.78±0.012	15.32±0.002
MIR-14	17.72±0.002	14.55±0.001	MIR-90	18.19±0.002	15.28±0.001
MIR-15	16.94±0.001	13.47±0.001	MIR-96	19.26±0.008	16.05±0.003
MIR-18	19.68±0.012	15.02±0.001	MIR-97	20.08±0.014	16.82±0.003
MIR-26	17.38±0.001	14.33±0.001	MIR-100	18.35±0.003	15.28±0.002
MIR-29	20.62±0.022	15.44±0.001	MIR-106	18.90±0.005	16.20±0.003
MIR-31	17.51±0.002	13.57±0.001	MIR-107	19.51±0.006	16.30±0.003
MIR-32	20.87±0.028	16.43±0.004	MIR-108	18.98±0.005	14.92±0.002
MIR-43	19.56±0.008	14.83±0.001	MIR-109	18.20±0.003	13.90±0.001
MIR-44	19.39±0.011	15.55±0.002	GFG 64	19.03±0.007	15.21±0.001
MIR-45	20.82±0.023	15.79±0.003	. . .	. . .	. . .

Table 2.5.   *BVI* photometry of MIR sources in SFO 38 on 23rd August, 2009

Source	B	V	I	Variability
MIR-1	19.82±0.010	18.24±0.005	16.00±0.003	
MIR-2	20.48±0.015	18.88±0.006	16.84±0.005	
MIR-3	21.58±0.021	19.58±0.007	17.14±0.004	
MIR-4	0.00±0.000	20.38±0.016	17.73±0.006	
MIR-5	21.11±0.015	19.32±0.007	16.37±0.002	BVI
MIR-7	21.59±0.021	19.39±0.006	16.38±0.002	
MIR-8	17.74±0.001	15.74±0.001	13.35±0.001	
MIR-9	19.95±0.017	18.48±0.004	16.62±0.004	
MIR-10	17.28±0.001	16.07±0.001	14.49±0.001	
MIR-11	0.00±0.000	19.52±0.011	16.19±0.005	
MIR-14	17.67±0.001	16.24±0.001	14.53±0.001	
MIR-15	16.89±0.001	15.26±0.001	13.44±0.001	
MIR-18	19.62±0.006	17.58±0.003	14.98±0.009	
MIR-26	17.34±0.001	16.03±0.001	14.30±0.001	
MIR-29	20.58±0.011	18.43±0.005	15.42±0.002	
MIR-31	17.43±0.002	15.71±0.001	13.52±0.001	
MIR-32	21.15±0.015	19.29±0.006	16.25±0.002	BVI
MIR-43	19.41±0.004	17.49±0.002	14.73±0.001	BVI
MIR-44	19.36±0.006	17.65±0.003	15.51±0.002	
MIR-45	21.41±0.018	19.45±0.007	16.33±0.002	BVI
MIR-47	0.00±0.000	19.86±0.009	17.61±0.005	
MIR-49	20.91±0.012	18.81±0.004	15.69±0.001	BVI
MIR-52	19.54±0.008	18.32±0.005	16.64±0.005	
MIR-58	20.13±0.007	18.75±0.003	16.91±0.003	B
MIR-60	20.79±0.011	19.13±0.005	17.06±0.003	
MIR-64	0.00±0.000	20.49±0.014	17.09±0.006	
MIR-76	19.08±0.006	17.16±0.002	14.55±0.001	
MIR-79	21.41±0.024	18.56±0.004	14.55±0.001	
MIR-80	21.69±0.023	19.81±0.008	16.00±0.004	V
MIR-87	19.72±0.005	17.72±0.002	15.28±0.002	
MIR-90	18.15±0.002	16.85±0.002	15.26±0.002	
MIR-95	0.00±0.000	20.16±0.012	17.34±0.004	
MIR-96	19.23±0.008	17.85±0.003	16.02±0.002	
MIR-97	20.06±0.007	18.63±0.005	16.83±0.004	
MIR-100	18.31±0.003	16.86±0.002	15.28±0.002	
MIR-106	18.87±0.004	17.75±0.003	16.21±0.002	
MIR-107	19.50±0.004	18.12±0.002	16.27±0.002	
MIR-108	18.94±0.005	17.31±0.004	14.86±0.001	
MIR-109	18.17±0.003	16.17±0.001	13.86±0.001	
MIR-110	0.00±0.000	19.78±0.010	15.76±0.003	*V*
BRC38 1	0.00±0.000	20.05±0.017	16.45±0.003	
BRC38 17	0.00±0.000	20.51±0.017	16.92±0.006	*V*
GFG 64	19.01±0.007	17.48±0.003	15.18±0.001	
IPHAS	0.00±0.000	20.28±0.011	16.50±0.004	

the accuracy of the optical photometric measurements. We consider a source to be *variable* if the magnitude difference is ≥ 0.1 mag (Table 2.5) at the two observing epochs. MIR-5, MIR-32, MIR-43, MIR-45 and MIR-49 show variation in *BVI* bands. In particular MIR-5 with $W_\lambda(H\alpha) \sim 80$ Å shows ~ 1 mag variability in B over a timescale of month.

YSOs also show variation in NIR bands which may or may not have any correlation with the optical variation (Eiroa et al., 2002). Both the stellar photosphere and the circumstellar disk contribute to the NIR fluxes of PMS stars. Hence, NIR variability can be either due to the same physical processes responsible for optical variability or any structural variability of disk and circumstellar materials. We compare the NIR magnitudes from 2MASS (Cutri et al., 2003) and from the more recently obtained JHK magnitudes by Beltrán et al. (2009)

of the sources reported in both the datasets to identify NIR variability. Sources which have shown variation of ~ 0.1 mag in any of the NIR band are listed in the last column of Table 2.1.

2.4.6 Medium Resolution Spectra of YSOs

The Hα emission though a very prominent feature in the spectrum of the YSO is not sufficient to identify YSOs because there also exist other kinds of Hα emission line stars *viz., Be, Mira* stars etc. Medium resolution spectroscopy is helpful to distinguish the YSOs from the *Be* and *Mira* stars. Figure 2.6 presents sample spectra observed with HFOSC of a few YSOs. The prominent features e.g. Hα, CaII NIR triplet etc. are marked in the respective spectra. We have detected strong Hα emission in most of the Class II objects except BRC 38 16 and therefore we do not consider it as a YSO in the remainder of the chapter. Log of spectroscopic observations and Hα equivalent widths (W$_\lambda$) of the individual YSOs are given in Table 2.6. BRC 38 6 (MIR-31) is the brightest Class II object detected in
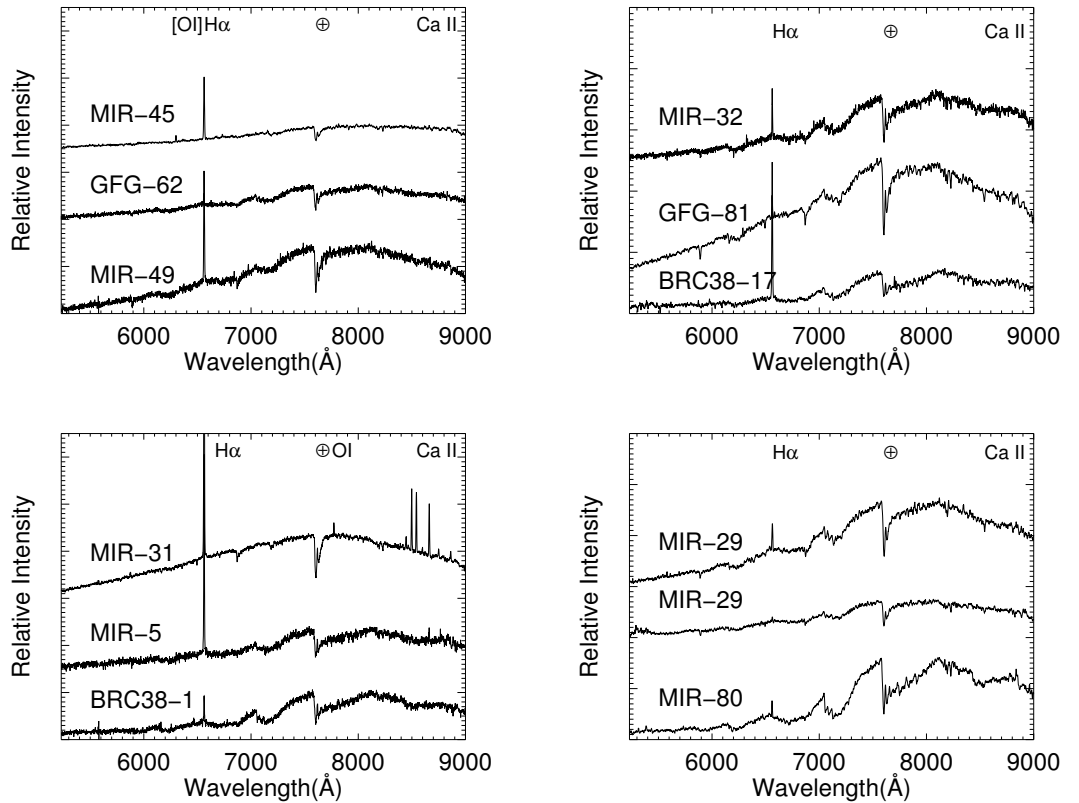
Figure 2.6 Sample spectra of YSOs in SFO 38 obtained with *HFOSC* instrument. The strong features e.g. Hα emission ($\lambda6563$Å), CaII infrared triplet emission , OI line at $\lambda7773$ Å and [O I] line at $\lambda6300$ Å are marked in the spectra. Atmospheric features are indicated with $\oplus$. Two spectra of MIR-29 taken at two different epochs show variable Hα emission (see text for details).

optical band. From the multiepoch spectroscopic observations we find that MIR-31 shows variable Hα emission (Table 2.6). We have also detected OI λ7773 (blend of OI λ7771.96, λ7774.18, λ7775.40), OI λ8446 (blended with Pa18 λ8437) CaII infrared triplet i.e λ8498 (blended with Pa16 λ8502), λ8542 (blended with Pa15 λ8545) and λ8662 (blended with Pa13 λ8665) and several other Paschen lines e.g. Pa10 λ 9014, Pa11 λ8862, Pa12 λ8750, Pa14 λ8598, Pa17 λ8467, Pa19 λ8413, Pa20 λ8392 in MIR-31. According to Muzerolle et al. (1998b), OI λ7773 is a very sensitive indicator of infall in the context of magnetospheric accretion scenario. LiI λ6708 (W_λ ∼0.7 Å) is also present in the spectra of MIR-31. All these spectroscopic features indicate that MIR-31 is indeed a YSO which is going through an active accretion phase. We have detected [OI] λ6300 and [OI] λ6363 and [SII] λ6717 and [SII] λ6731 emission lines in MIR-45 which are well known signatures of outflows from YSOs. We also find a positive correlation between Hα emission and MIR excess for YSOs with $W_\lambda(H\alpha) \leq 40$ Å. We have detected sporadic Hα emission in transitional disk object MIR-29 on 3rd November 2008. We observed the object in 2009 also but we do not find any further Hα emission. We have detected weak Hα emission from two more transitional disk objects e.g. MIR-43 ([GFG2007] 62) and MIR-76 ([GFG2007] 81). We also obtained the spectra of few more transitional disk objects e.g. MIR-1, MIR-2, MIR-9, MIR-18 and MIR-108 and do not find Hα emission in any of these objects.

2.4.7 Spectral Classification

We have classified the observed optical spectra by manual inspection of the spectra of target stars and also by comparing it with the spectra of known spectral type. We observed several stars with spectral type of F to M from Jacoby et al. (1984), Valdes et al. (2004) and Kirkpatrick et al. (1991) with HFOSC using the same set up as the target stars to minimize the effect of instrumental effects and resolution. From preliminary analysis we find that the YSOs are of spectral types K and M.

For more accurate classification in the range of spectral type K–M, we use the calibration file provided in the *SPTCLASS* (Hernández et al., 2004) code for various absorption features *viz.,* TiO bands etc. The detailed information on the classification scheme can be found in the *SPTCLASS* code[5]. This scheme measures the equivalent widths or "indices" of the absorption features which are sensitive to T_{eff} using the adjacent blue and red continuum bands and calibrate the indices against the spectral type of the stars. Spectral type of the target star is determined from the weighted mean of the spectral types obtained from different absorption features of the target star excluding the apparently anomalous values. As this classification scheme uses the local continuum of the absorption feature, it is insensitive to reddening and the S/N ratio. Further, the spectral features which are used for classification are also insensitive to the luminosity class. The errors in the spectral

---

[5]http://www.astro.lsa.umich.edu/~hernandj/SPTclass/sptclass.html

type determination come from the measurement of indices and the standard deviation of the spectral types obtained from different absorption features. To check the applicability of the adopted calibration on *HFOSC* spectra we classify the *HFOSC* spectra of a few K and M type stars and retrieve the spectral type within ∼0.5 subtype. We then use the same calibration scheme to classify the YSO spectra. We further explore the Fe I λ6495 Å line to classify the spectra of early K type stars (Gray & Corbally, 2009). The "index" or equivalent width of λ6495 line was calculated for spectral types F–K, using the *HFOSC* spectra of stars with known spectral type taken from Jacoby et al. (1984); Valdes et al. (2004). The results of our classification are summarized in Table 2.6. We also tabulate the effective temperatures of YSOs using the *table* of Kenyon & Hartmann (1995). Using the *V-I* color of a particular spectral type and our optical *BVRI* observations we calculated the A_v assuming the normal interstellar extinction law as given by Bessell & Brett (1988). The average extinction towards the globule is estimated to be $A_v = 2.5$ mag.

2.4.8 Rate of Accretion from Hα Emission

Emission in the Balmer Hα and other Hydrogen lines, have been very useful the iconic spectral diagnostics of accretion of circumstellar materials in the YSOs. Magnetospheric accretion models have provided satisfactory explanation of the observed spectral characteristics of accretion in CTTS e.g. broad asymmetric line profiles etc. (Muzerolle et al., 1998a, 2001). According to the magnetospheric accretion model the stellar magnetic field disrupts the circumstellar disk at several stellar radii and accreting material fall to the stellar surface along the magnetic field lines (Koenigl, 1991). Magnetospheric accretion models suggest that the hydrogen emission lines form in the infall zone, so that the blue shifted asymmetric emission line profiles arise due to partial obscuration of the flow by the inner part of the accretion disc and the red shifted absorption profiles result from infalling material at near free-fall velocities on the stellar surface (Muzerolle et al., 1998a). Strength of the Hα emission line has been widely used to distinguish the actively accreting CTTS from their less active and evolved counterparts i.e Weak-lined T Tauri Stars (WTTS). White & Basri (2003) proposed to classify a YSO as CTTS if W_λ (Hα) ≥ 3 Å for K0–K5 stars, W_λ (Hα) ≥ 10 Å for K7–M2.5 stars, W_λ (Hα) ≥ 20 Å for M3-M5.5 stars, and W_λ (Hα) ≥ 40 Å for M6-M7.5 stars. They also proposed that the stars with full width of Hα emission line at 10 % of the peak intensity (Hα[10%]) greater than 270 km s^{-1} are accreting CTTS independent of spectral type. We identify *9* stars as CTTS and *5* stars as WTTS according to the above mentioned criteria (Table 2.6).

Table 2.6. Spectral Classification of YSOs

ID	Alt. ID	Date	W_λ (Å)	Sp. Type (±subtype)	T_{eff} (K)	Type	Hα[10%] (km s^{-1})	log $\dot{M}_{ac}$ (M$_\odot$ yr^{-1})	α_{IRAC}	E(V-I)	A_V	E(V-I)/E(B-V)
BRC 38 1		5/10/08 10/10/09	-12.93 -16.24	M3±1	3470	CTTS	312.23 205.29	-9.86 -10.90		1.13	2.81	
MIR-5	BRC 38 2	5/10/08 10/10/09	-85.23 -106.1	M1±1	3720	CTTS	359.79	-9.40 -10.52		0.99	2.47	3.19
MIR-7	BRC 38 3	6/10/08 10/10/09	-19.0 -18.75	M1±2	3720	CTTS	244.53 476.25	-8.27 -8.39	-0.87	1.05	2.61	1.46
MIR-11	BRC 38 4	10/09/08 18/07/09	-7.30 -11.29	M1±2	3720	WTTS	463.50		0.02	1.37	3.41	
MIR-29	BRC 38 5	6/09/08 3/11/08 24/08/09 9/11/09	-3.42 -8.84 -1.89 -2.74	M1±2	3720	WTTS	469.90	-8.33	-1.74	1.05	2.61	1.57
MIR-31	BRC 38 6	6/09/08 24/08/09 9/10/09	-53.47 -57.32 -60.5	K2±1	4900	CTTS	384.43 442.02 382.26	-9.16 -8.60 -9.18	-1.60	1.18	2.94	1.42
MIR-32	BRC 38 7	10/09/08 12/09/09	-33.12 -15.78	M2±1	3580	CTTS	368.03 220.59	-9.32 -10.75	-1.03	0.90	2.24	2.65
MIR-43	GFG 62	18/07/09	-3.516	M1±1	3720	WTTS			-2.61	0.80	1.99	1.82
MIR-45	BRC 38 9	6/09/08 3/11/08 24/08/09	-37.43 -41.22 -56.33	K4±1	4590	CTTS	281.09 389.74 273.39	-10.16 -9.11 -10.24	-0.18	1.97	4.91	2.21
MIR-49	BRC 38 10	4/11/08 9/10/09	-13.5 -30	M0±1	3850	CTTS	430.70 450.55	-8.71 -8.52	-1.37	1.32	3.29	1.91
MIR-64	BRC 38 11	10/09/08 12/09/09	-31.46 -25.06	K5±1	4350	CTTS	239.20	-10.57	0.10	2.04	5.08	
MIR-76	GFG 81	18/07/09 10/10/09	-3.261 -3.135	K7±1	4060	WTTS			-1.07	1.01	2.51	1.87
MIR-80	BRC 38 12	24/08/09	-8.404	M4±1	3370	WTTS			0.31	0.95	2.37	
BRC 38 17		11/11/09	-119.	M3±2	3470	CTTS	205.29	-10.90		1.12	2.79	3.39

Natta et al. (2004) showed that Hα[10%] $\geq$ 200 km s^{-1} can be used to distinguish the accretors and non accretors as well as to derive an approximate estimate of the accretion rate $\dot{M}_{ac}$ quantitatively by the following relation,

$$\log\dot{M}_{ac} = \text{-12.89} (\pm 0.3) + 9.7 (\pm 0.7) \times 10^{-3} \text{ H}\alpha[10\%]$$

where Hα[10%] is in km s^{-1} and $\dot{M}_{ac}$ is in M$_{\odot}$yr^{-1}. In order to estimate the accretion rates from some of the well resolved Hα line profiles, we fitted Gaussian profiles to the Hα emission lines and calculate the equivalent width and FWHM of each line profile. The measured FWHM of each profile has been deconvolved assuming a Gaussian instrumental profile. We calculate the Hα[10%] for these objects and transformed them into velocity units. We did not correct for the underlying photospheric absorption in Hα if there is any. Table 2.6 presents the accretion rates $\dot{M}_{ac}$, calculated using the above formula along with the measured values of Hα[10%]. Based on the observed multiepoch spectra we find variable accretion rates in BRC 38 1, MIR-5, MIR-31, MIR-32 and MIR-45.

2.4.9 Optical Color-Magnitude Diagram

Figure 2.7 presents the extinction-corrected 'V vs. V-I' diagram for the YSOs associated with SFO 38. We have corrected for the extinction of individual objects with known spectral types and used an average value of A_v=2.5 mag when the spectral type is not known. In order to estimate the mass and age of the YSOs we overplot the isochrones from Siess et al. (2000) assuming a distance of 750 pc (Matthews, 1979). We find that most of the YSOs (Class II with(out) Hα) have ages between 1-5 Myr and masses in the range 0.3-2.2 M$_{\odot}$. We note that several transitional disk objects are located to the left of the Zero Age Main Sequence (ZAMS) line. A closer examination of the position of the transitional disk objects in the MIR color-color diagram (Fig. 2.4) reveals that 6 out of 7 transitional disk objects which are situated to the left of ZAMS line have [5.8]-[8] color excess $<$ 0.5 and 4 out of 5 transitional disk objects which are situated to the right of ZAMS line have [5.8]-[8] color excess $>$ 0.5. The transitional disk objects to the left of the ZAMS line are more like Class III objects with smaller values of color excess. We have used an average A_v=2.5 mag for extinction correction for these objects because the spectral types are not known. There are several factors that could lead the transitional disk objects to the anomalous position in Fig. 2.7 e.g. extinction correction, uncertainties in distance and PMS evolution model used. An extinction correction with a smaller A_v ($\leq$1 mag) brings all the transitional disk objects closer to, or to the right of the ZAMS line. The distance of IC 1396 is in the range of 615 pc (de Zeeuw et al., 1999) to 900 pc (Contreras et al., 2002) and we adopt a distance of 750 pc for SFO 38 to make our results comparable to most published results. This uncertainty in the distance corresponds to an uncertainty of $\pm$ 0.4 mag in the absolute magnitude.

Adoption of a distance of 900 pc brings up the transitional disk objects somewhat closer to the ZAMS line but these objects still occupy positions below the ZAMS line. While different theoretical models differ in the details of the PMS evolution, close to the ZAMS line all these models agree with each other and with the empirical ZAMS of the young star clusters. Therefore, the anomalous positions of the transitional disk objects with respect to the ZAMS track in Fig. 2.7 is primarily due to over-correction of the extinction. Estimation of mass and age from the color-magnitude diagram (CMD) is strongly dependent on the adopted model (Hillenbrand et al., 2008). The ages can differ by as much as 10 Myr or more when two different models are used on the same dataset (Ikeda et al., 2008). The main source of error in the V vs. V-I diagram is the estimation of extinction towards the globule. In the last column of Table 2.6 we list the ratios of E(V-I)/E(B-V) which are different from the standard value of 1.6 and indicate that normal extinction law may not hold good for star forming regions due to anomalous dust absorption (Bhatt & Gorti, 1993). Although the NIR *JHK* bands suffer comparatively less extinction than the optical *BVRI* band but for the YSOs, thermal emission also contributes to *JHK* bands resulting in excess fluxes compared to the main sequence counterparts without disk. For a given model we consider the derived values of the masses and ages as representative values and the age spread of YSOs as more reliable estimate.

2.4.10 Spectral Energy Distribution (SED) of YSOs with MIPS 24 μm Detection

In order to interpret the observed Spectral Energy Distribution (SEDs) for the YSOs detected at 24 μm and better characterize these sources we have explored the archive of two-dimensional (2D) axisymmetric radiative transfer models of protostars calculated for a large range of protostellar masses, accretion rates, disk masses and disk orientations created by Robitaille et al. (2007). This archive also provides a linear regression tool which can select all model SEDs that fit the observed SED better than a specified χ^2. Each SED is characterized by a set of model parameters, such as stellar mass, temperature, and age, envelope accretion rate, disk mass, and envelope inner radius. We have used this online tool to generate models, which fit the observed SEDs for the 14 YSOs which have been detected at 24 μm. We restricted the SED fitting tool to explore only distances between 650 and 850 pc. Below we present and briefly discuss the best fit models.

Figure 2.8 shows results of detailed modeling of the observed SED in the mid-infrared (and sub-mm for MIR-50) for all the YSOs which were detected at 24 μm. A major criticism against the use of these models has been the non-uniqueness of the solutions obtained from the model library. However we find that for all sources the best fit models are distinctively better than the next few models in reproducing all the observed flux densities. Table 2.7
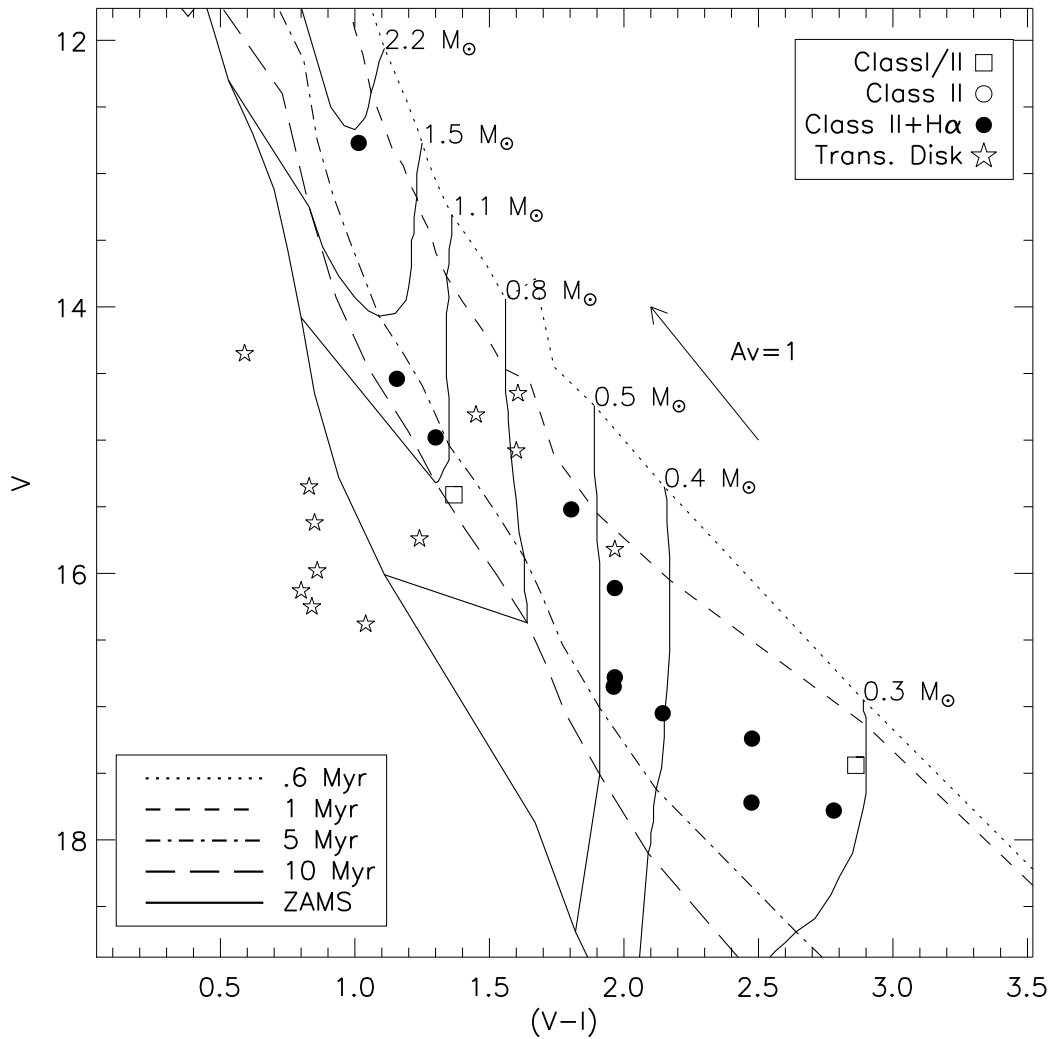
Figure 2.7 Extinction corrected V vs. V-I Color-Magnitude diagram for YSOs associated with SFO 38. Hα emission YSOs are shown by *filled circles.* The ZAMS and 0.6, 1, 5, 10 Myr isochrones of Siess et al. (2000) are shown with the evolutionary tracks for masses from 0.3 to 2.2 $M_\odot$, at an adopted distance of 750 pc.

presents the parameters corresponding to the best fit models for the fourteen sources which we fitted with the accretion disk models.

Robitaille et al. (2006) presented a classification scheme which is essentially analogous to the Class scheme, but refers to the actual evolutionary stage of the object based on its physical properties like disk mass and envelope accretion rates rather than the slope of its near/mid-IR SED. According to the Robitaille et al. classification scheme, MIR-50 and MIR-54, are stage 0/I objects, while all the others are stage II objects. However, the YSOs MIR-34, 36, 48, 55 and 59 were identified as Class 0/I objects based on the color-color diagrams. Next we consider the fact that except for MIR-34 all the sources have rather high visual extinction (A_v >40) and the MIR color-color diagrams we had used to classify
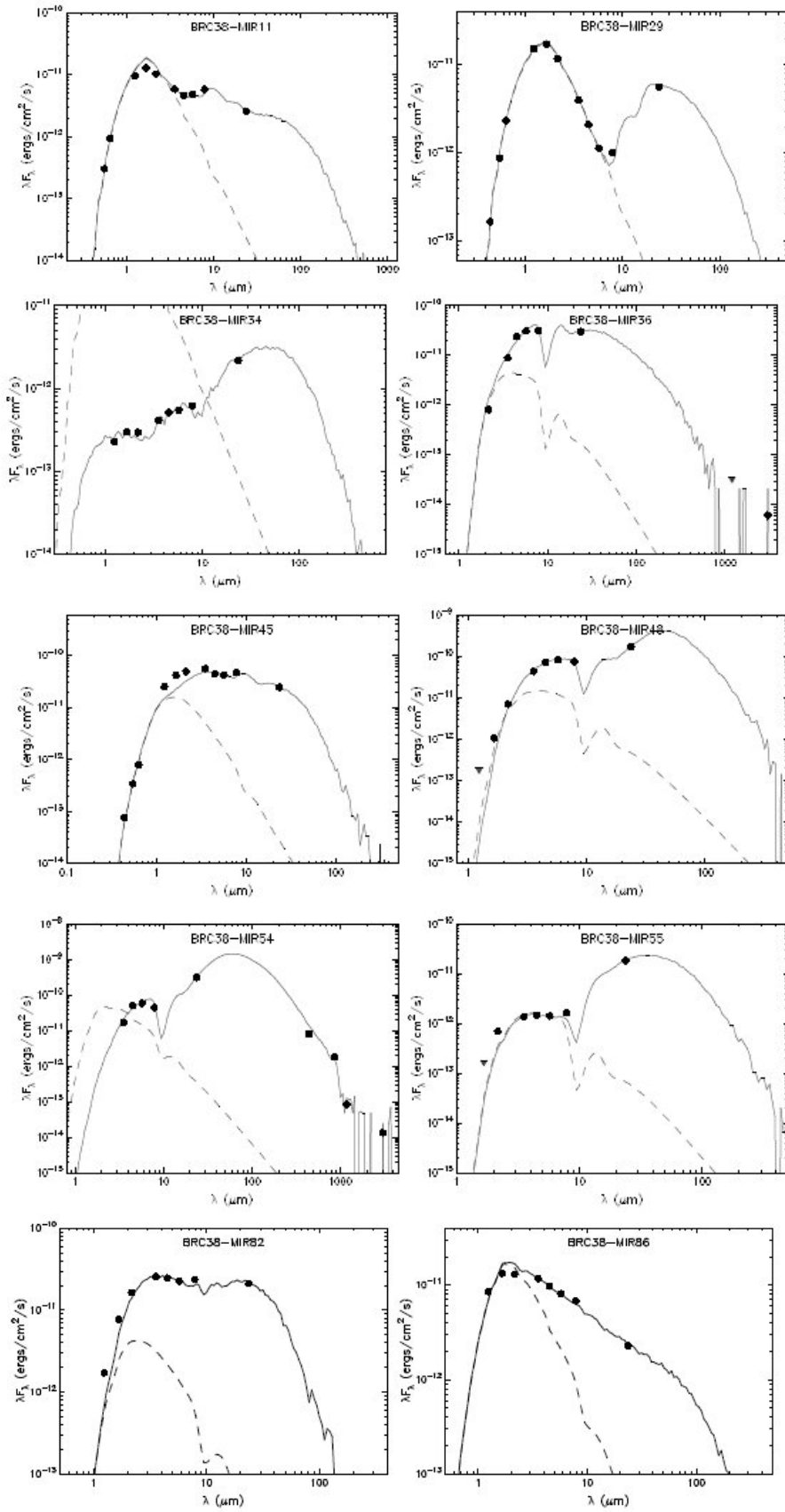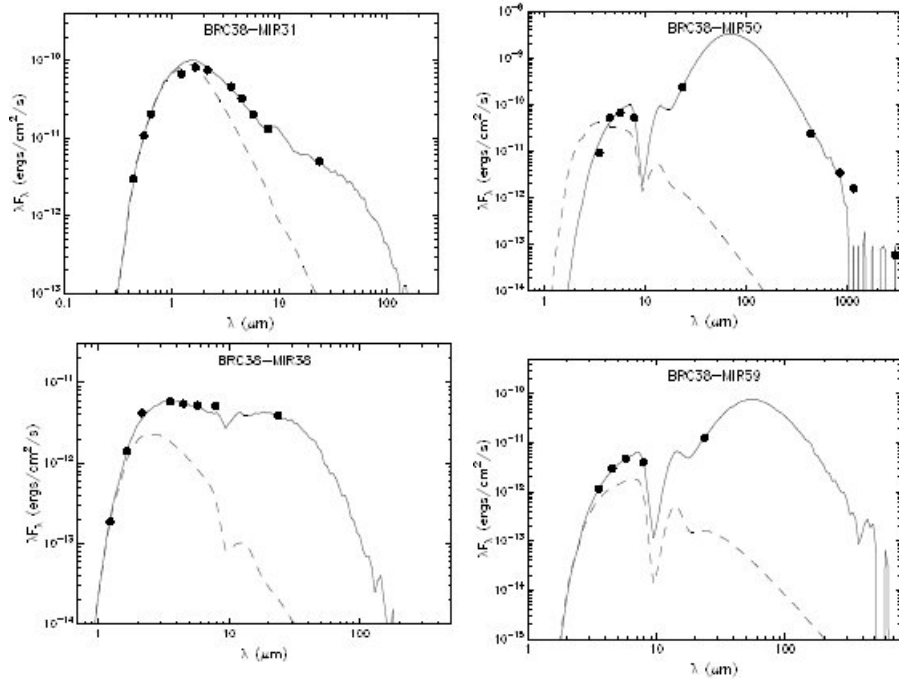
Figure 2.8 SED fits for the PMS objects using axisymmetric radiation transfer models. The filled circles indicate the measured fluxes and uncertainties. The filled triangles correspond to the upper limits of flux at these wavelengths. The continuous black line represents the best-fitting SED, and the dashed line shows the stellar photosphere corresponding to the central source of the best fitting model, in the absence of circumstellar dust (but including interstellar extinction).

the YSOs did not correct for the reddening. Using standard interstellar extinction laws (Indebetouw et al., 2005) and the A_v derived from the models, we find that when de-reddened, the sources MIR-48, 55 and 59 occupy the region typically occupied by Class II objects. However for MIR-34 and 36 the difference in the inferred evolutionary stage can not be explained only in terms of reddening.

Based on the results of fitting the observed SEDs with axially symmetric accretion models we find that all the YSOs analyzed here have low to intermediate-mass central stars. Figure 2.5 shows that consistent with our expectations the sources located within the globule have A_v>20 mag, while the sources lying at the periphery of the bright rim have A_v between 3–5 mag. In Sec. 2.4.11 we discuss the two most luminous Class 0/I sources MIR-50 and MIR-54 in detail.

The ages estimated for these fourteen YSOs from the SED models and the location of these sources in BRC 38 show that most of the sources closer to the bright rim have ages between 5–8 Myr. The sources within the BRC and lying almost along the axis of the BRC have ages between 0.1–1 Myr, with the protostellar cluster at the position of IRAS 21391+5802 being the youngest with an age of ∼0.1 Myr. The age spread estimated for the YSOs (mostly Class II and above) from optical CMD diagram is of the range 1–8 Myr. However,

Table 2.7. Parameters derived from SED modeling using axisymmetric radiation transfer models for the candidate YSOs. A_v refers to the foreground extinction towards the source.

Source	T_* K	M_* $M_\odot$	$M_{\rm disk}$ $M_\odot$	$M_{\rm env}$ $M_\odot$	$\dot{M}_{\rm env}$ $M_\odot\ {\rm yr}^{-1}$	$\dot{M}_{\rm disk}$ $M_\odot\ {\rm yr}^{-1}$	L $L_\odot$	A_v	Age Myr
MIR-11	4442	1.26	6.44×10^{-3}	6.39×10^{-5}	0.0	2.10×10^{-9}	1.27	5.3	3.2
MIR-29	4837	1.55	1.66×10^{-3}	6.13×10^{-7}	0.0	1.16×10^{-9}	1.67	4.4	5.8
MIR-31	5923	1.88	1.33×10^{-4}	7.04×10^{-8}	0.0	2.41×10^{-9}	8.92	4.2	6.7
MIR-34	4523	1.53	7.64×10^{-5}	2.56×10^{-3}	1.21×10^{-8}	1.28×10^{-10}	5.8	3.2	0.69
MIR-36	5413	3.29	4.37×10^{-3}	1.85×10^{-8}	0.0	4.80×10^{-8}	29.1	49.6	1.3
MIR-38	7854	1.98	3.10×10^{-5}	2.99×10^{-6}	0.0	5.49×10^{-11}	11.9	23.0	8.2
MIR-45	9960	2.32	4.23×10^{-5}	1.70×10^{-8}	0.0	1.37×10^{-9}	27.0	8.3	9.4
MIR-48	7554	5.14	1.71×10^{-3}	21.4×10^{-2}	2.23×10^{-7}	2.38×10^{-9}	280	45.9	0.49
MIR-50	4643	5.97	7.67×10^{-2}	40.8	3.82×10^{-4}	2.08×10^{-8}	196.7	44.4	0.1
MIR-54	4290	1.50	2.46×10^{-2}	9.3	7.13×10^{-5}	2.98×10^{-6}	33.4	19.6	0.17
MIR-55	4989	3.07	7.86×10^{-4}	1.44×10^{-3}	1.97×10^{-9}	1.14×10^{-9}	14.4	52.3	0.91
MIR-59	5218	4.27	9.99×10^{-3}	7.37×10^{-3}	2.95×10^{-7}	2.00×10^{-8}	60.5	87.4	0.53
MIR-82	11320	2.77	5.85×10^{-5}	1.18×10^{-6}	0.0	1.40×10^{-10}	57.2	21.0	4.8
MIR-86	4594	1.55	8.18×10^{-4}	3.63×10^{-7}	0.0	4.50×10^{-10}	2.59	9.7	1.8

the ages estimated from both methods are higher than the ages obtained from the NIR CMD by Getman et al. (2007).

2.4.11   The Protostellar Cluster at IRAS 21391+5802

Interferometric millimeter continuum images have shown that the most luminous source IRAS 21391+5802 in the IC 1396 region can be resolved into three components, named as BIMA 1, BIMA 2 and BIMA 3 (Beltrán et al., 2002). Radio continuum images at 3.6 cm observed with VLA have also identified three peaks VLA 1–3, coincident with the millimeter continuum peaks (Beltrán et al., 2002). Of these three sources VLA 3 is the strongest emitter of radio continuum. Recent sub-arcsecond resolution millimeter observations have identified three components within BIMA 2 itself (Neri et al., 2007). The SCUBA images at 450 and 850 μm do not resolve the components of continuum emission associated with IRAS 21391+5802 (Morgan et al., 2008).

We identify MIR-50 and 54 as the mid-infrared counterparts of BIMA 2 and BIMA 3 and do not detect any source associated with BIMA 1. The source MIR-36 is located $3\rlap{.}''8$ away from BIMA 1 and hence is most likely not associated with BIMA 1. We have used the continuum fluxes available in literature to construct the observed SEDs for MIR-50 and MIR-54. In order to make a realistic estimate of the flux densities at 450 and 850 μm from each of BIMA 2 and BIMA 3, we have split up the observed total flux densities at these wavelengths according to the ratio of flux densities of these sources measured at 1.2 mm by Beltrán et al. (2002). Fitting of the observed flux densities with the axially symmetric accretion-based models (Robitaille et al., 2007) shows that MIR-50 (BIMA 2) is a protostellar object with $L = 197$ L$_\odot$ and a mass of 5.97 M$_\odot$. Both mass and luminosity values match reasonably well with the literature. We note however that the model fitted does not reproduce the interferometric flux densities at 1.2 and 3.1 mm well. This is consistent with the conclusions

of Beltrán et al. (2002) that the interferometric observations miss a significant amount of emission. The best fit model for MIR-54 corresponds to a mass of 1.5 $M_\odot$ and a luminosity of 33.4 $L_\odot$. Codella et al. (2001) had estimated an integrated luminosity of 233 $L_\odot$ including both BIMA 2 and BIMA 3 and here we derive a total luminosity of 230 $L_\odot$. Based on the SED fitting performed in this chapter, MIR-54 or BIMA 3 is a low mass Class 0/I protostar and MIR-50 or BIMA 2 is a Class 0/I intermediate-mass star, although Neri et al. (2007) have already shown BIMA 2 as having three components. The SED models derive the age of both these sources to be $\sim 10^5$ yr.

2.5   Discussion: RDI Mechanism at Work in SFO 38

Based on the observational evidences in the form of YSOs, an outflow-driving IRAS source and several HH objects, SFO 38 is unambiguously an active star forming region. There is however considerable disagreement regarding whether the star formation is triggered or influenced by the nearby OB association. The two most recent studies of SFO 38 based on Chandra X-ray and *Spitzer* Mid-IR observations (up to 5.8 μm Getman et al., 2007) and deep NIR observations (Beltrán et al., 2009) arrive at diametrically opposite conclusions. Considering the spatial and temporal distribution of the fewer YSOs selected by using MID-IR color-color diagram ([3.6]–[4.5] vs. [4.5]–[5.8]), Getman et al. (2007) argued in favor of triggered star formation by Radiation Driven Implosion (RDI) model. However Beltrán et al. (2009) did not find either *(a)* enhanced star formation activity towards the southern rim of SFO 38 or *(b)* systematic gradient in the evolutionary stage of the YSOs using the deep NIR imaging. Based on the absence of NIR excess from the YSOs Beltrán et al. (2009) concluded that the sources closer to the O type star appear to be more evolved primarily due to the modification of their environment by the intense UV field. Thus, according to Beltrán et al. the evolutionary sequence observed by Getman et al. should not necessarily be interpreted as due to triggered star formation. However Beltrán et al. also concede that NIR-only studies are inadequate to identify all the YSOs in the region.

We explore two possible scenarios which could have been the dominant driving mechanism to initiate the formation of stars in SFO 38 *viz.,* coeval star formation throughout the H II region and triggered star formation by the RDI mechanism. The assumption that the stars near the globule were formed simultaneously with the other stars of the OB association suggests that the distribution of YSOs should be correlated with the distribution pattern of the other massive to low mass stars of the OB association. The observed elongated distribution of YSOs along two different axes in SFO 38 is quite different from the distribution of the known members of Cep OB2 association (Fig. 22 of de Zeeuw et al., 1999). Moreover the ages of the outflow driving IRAS source and the associated protostellar cluster are significantly less than the dynamical age of 3 Myr (Patel et al., 1995) of the H II region created by the massive OB type stars. We thus rule out the possibility of coeval star formation

in SFO 38 with the members of Cep OB2 association, although some of the Hα emitting sources could have been formed prior to the arrival of the shock front. Next, we investigate the other possibility, based on the RDI model, by comparing our observations with the predicted signatures of the model. The RDI model suggests enhancement of density along the axis of the UV irradiated globule and an age sequence of YSOs with the oldest YSO lying closer to the OB association.

Sequential star formation is considered to be one of the key signatures of triggered star formation via RDI. Beltrán et al. (2009) have cautioned against the use of the spatial distribution of YSOs as a proof of triggered star formation, by arguing that intense UV fields close enough to the OB associations tend to destroy the protoplanetary disks around the YSOs and thus make them appear to be older. However we find this argument untenable for the case of SFO 38, since the typical radius of influence of O stars is found to be $< 1 \, \text{pc}$ (Balog et al., 2007; Hernández et al., 2008; Mercer et al., 2009), while the mean projected distance of the nearest O and B -type stars close to SFO 38 is $\sim 9 \, \text{pc}$. Thus the spatial distribution of the YSOs discussed in SFO 38 signify the temporal evolution of the YSOs and not due to the destruction of protoplanetary atmospheres under the influence of the UV radiation from the OB association.

The bright-rimmed cloud SFO 37, was found to have an an exemplary bow shaped geometry and shows a clean evolutionary sequence of YSOs (Ikeda et al., 2008). SFO 38 in contrast has a more complicated geometry. As noted earlier the Hα emission from SFO 38 shows an asymmetry relative to the axis connecting the globule to the nearest O star HD 206267. Further, in SFO 38 though the YSOs clearly show an age segregation, they are not distributed along a single straight line. It is however possible to identify another direction along which some of the YSOs are most likely aligned. The asymmetry of Hα emission and the non-linearity of the distribution of YSOs suggest that the evolution of SFO 38 is influenced by the nearby B star HD 206773 as well. From the Hα line image (Figure 2.5) HD 206773 seems to be ionizing the eastern part of the rim more efficiently than the extent to which HD 206267 has ionized the western part of the rim. Using the $^{13}CO \quad J = 1\text{--}0$ map of SFO 38, Patel et al. (1995) also found that the eastern and western wings of SFO 38 differ in velocity by about 1.5 km s^{-1} relative to the velocity of the dense core of the globule. This suggests that HD 206773 plays an active role in the present dynamics of the globule.

We have identified a spatio-temporal gradient in the distribution of YSOs along the directions of both HD 206267 and HD 206773. However the spatial gradient is not continuous, there is a distinguishable gap between the two classes of YSOs e.g. the projected distance of Class I/II sources from the approximate center of the distribution of Class I sources is ~ 0.3 pc and this gap can be interpreted as due to the difference in the arrival times of the shock within the framework of the RDI model. If we consider the age spread to be $\sim$ a few Myr (comparing the estimated ages from SED fitting and optical CMD) and the spatial separation between the MIR-50 (Class 0/I) and MIR-29 (Class II) to be ~ 0.6 pc,

we obtain the speed of shock propagation to be 0.1–$0.3\,\mathrm{km}\,s^{-1}$. The estimated shock speed is consistent with the shock velocities obtained from 3-D numerical simulations (Miao et al., 2006). The estimated speed of shock propagation are approximate since we use only projected distances between sources and do not consider the time lapse between the arrival of the shockwave and the triggering of star formation in the globule, which from simulations is ~ 0.375 Myr (Miao et al., 2006).

Thus, our observations and estimate of the evolutionary stages of the YSOs embedded in SFO 38, are consistent with a scenario of triggered star formation via the RDI mechanism powered by two different ionizing sources, HD 206267 and HD 206773.

Feedback of Massive Stars to

Giant Molecular Clouds

Part II. Clearing the Central H II Cavity

Chapter 3

Kinematics of Young Stellar Objects and Cometary Globules in an Evolved H II Region: Gum Nebula

3.1 Introduction

In Chapter 2 we discuss the constructive role of the radiative feedback of the massive stars in the formation of next generation of stars from the leftover molecular material. As we discuss in Chapter 1, the feedback of massive stars can also disrupt the molecular cloud. For example, the *Rocket Effect* can push the leftover material radially outward from the center of the H II cavity and thus can reshape the morphology of the H II region. At the same time, photoevaporation by massive stars, supernova explosions etc. can also play important roles in shaping the morphology of the *blistered* H II regions. All these effects are generally present in relatively evolved H II region or OB association. It has also been suggested that the nearly circular distribution of the Bright-Rimmed Clouds (BRCs) or Cometary Globules (CGs) at the border of the H II regions is resulted due to the destructive feedback of the massive stars. We are interested to understand the importance of these disruptive processes in the distribution and kinematics of the CGs in a comparatively evolved H II region. To analyze the source cause of the kinematics of CGs, measurements of their motion in the plane of the sky are very important. Since CGs are diffuse structures so their proper motion measurements are not feasible. But the embedded young stars in CGs share the same motion as their parent globules. We planned to use the proper motion of the YSOs near CGs as a proxy for the motion of these globules. To get a good statistics, a reasonable number of relatively bright YSOs associated with different CGs in a comparatively evolved

and nearby H II region are needed. Relatively evolved H II region, the Gum Nebula, satisfies all the criteria required for this work.

The Gum Nebula, a prominent H II region of southern Milky Way, was discovered by Gum (1952). The whole nebula is around 36° in diameter (Chanot & Sivan, 1983). The true nature of the Gum Nebula is not very clear. Along with the two O type stars ζ Pup and γ^2 Velorum, two OB associations, Vela OB2 and Tr 10, have been found in the Gum Nebula region. There are also two supernova remnants (SNRs) in the direction of the Gum Nebula, Pup A and Vela SNR. However, Sridharan (1992) argued that the spatial coincidence of these two SNRs with the Gum Nebula is due to chance superposition. Chanot & Sivan (1983) described the Gum Nebula as an intermediate structure between classical HII region and typical supernova remnant.

About 30 cometary globules have been found in the Gum Nebula and they are distributed in a nearly circular pattern. They share common features of a compact, dusty head (sometimes with a bright-rim), and a comet-like tail. The tails of the globules generally point radially outwards from the center of the Vela OB2 association. The axes of these CGs seem to converge on a very small area around at $l_{\parallel} \sim 261°$, $b_{\parallel} \sim$ - 5° (e.g. Reipurth, 1983, Zealey et al., 1983). The source of the CG complex is as yet still unclear. A single source may not be responsible for the formation and the evolution of the Gum Nebula complex. ζ Pup, and γ^2 Velorum and the two OB associations are considered as the probable source of the UV radiation and photoionization of the nebula in the literature.

There are some uncertainties about the distances of ζ Pup and γ^2 Velorum. The estimated Hipparcos distance to the Wolf-Rayet WC8+O spectroscopic binary γ^2 Velorum is 258^{-31}_{+41} pc and to the O4I(n)f star ζ Pup it is 429^{-77}_{+120} pc (van der Hucht et al., 1997). However, Pozzo et al. (2000) argued that the distance to the γ^2 Velorum may be same as that for the Vela OB2 association. Again the estimated Hipparcos distance to the Vela OB2 association is 410 pc (de Zeeuw et al., 1999) and Woermann et al. (2001) estimated a distance of 500 pc to the expansion centre of the association. In this context an average distance to the CG system as 450 pc is reasonable as adopted by Sridharan (1992).

There have been several studies on the kinematics of the Gum Nebula region to determine whether the system is expanding or not, e.g. Yamaguchi et al. (1999) and references therein. Most of the studies concluded that the molecular material associated with the Gum Nebula is expanding though the expansion velocities obtained from various studies are different from each other. Zealey et al. (1983) and Sridharan (1992) studied the kinematics of the CGs in details and based on the radial velocity measurements concluded that the CGs are expanding and obtained the expansion velocity of the system as 5 and 12 km s^{-1} respectively. Woermann et al. (2001) investigated the kinematics of the neutral material around the Gum Nebula. They concluded that the Diffuse Molecular Clouds (DMCs) and CGs form a single expanding shell centered on $l_{\parallel} = 261°$, $b_{\parallel} = $ -2.5°. According to

their model the shell is asymmetric with the radii of the front and back faces as 130 and 70 pc respectively. They also obtained the expansion velocities of 14 and 8.5 km s^{-1} for front and back faces respectively. They suggested the supernova explosion of the companion of ζ Pup about 1.5 Myr ago as the probable origin of the Gum Nebula and the expanding shell.

There have been no studies of the transverse (in the plane of the sky) motion of the Gum Nebula and the associated CGs. In this chapter we have examined the proper motion measurements of stellar and Young Stellar Objects (YSOs) in this region to study the expansion of the system of CGs and possible sources responsible for the triggered star formation in the CGs of Gum Nebula. In Sections 3.2 and 3.3. we summarize the characteristics of the CGs in the Gum Nebula as well as the known YSOs in and around the CGs. We discuss the proper motions of the YSOs in Section 3.4. Results are discussed in Section 3.5 and conclusions are presented in Section 3.6.

3.2   Cometary Globules in the Gum Nebula

Zealey et al. (1983) carried out an extensive study of the cometary globules in the Gum Nebula region. They found 29 CGs within a region of projected angular radius of 9.5°. They tabulated the coordinates, position angles, tail directions and measured H_2CO radial velocities of some of the CGs. They proposed the approximate centre of the CG complex based on the best fitting circle of the CG positions. Sridharan (1992) found some discrepancies in the coordinates of the CGs and redefined the coordinates of the individual CGs. Sridharan (1992) studied the kinematics of the cometary globules in the Gum Nebula using the transition lines of ^{12}CO and tabulated the V_{LSR} velocities of most of the CGs. We have adopted positions and velocities from Sridharan (1992) and the approximate centre of the system from Zealey et al. (1983). Reipurth (1983) suggested that the CGs are pointed towards the triangle formed by ζ Puppis, γ^2 Velorum and Vela Pulsar and estimated an average projected distance of 70 pc for the CGs from the centre of the triangle. It is possible that the two O type stars and the progenitor of the Vela Pulsar were the main energy source of the whole Gum Nebula region in the past. In Figure 3.1 we have plotted the respective CGs, members of the Vela OB2 association and the YSOs around the CGs in the galactic coordinates together with the the probable energy sources γ^2 Velorum and ζ Pup. The adopted centre of the nebula from Zealey et al. (1983) is also plotted. The vectors associated with the CGs in the plot have lengths proportional to the tail-lengths of the CGs and also indicate their directions.

Various authors derived the centre of expansion of the CG complex, e. g., Zealey et al. (1983), Reipurth (1983) and Sridharan (1992). In this chapter we have adopted the position of the centre as suggested by Zealey et al. (1983) i. e., RA(2000) $= 08^h19^m40.54^s$ Dec(2000) $= $ - 44°09′30.8″ (l $\sim$ 261.10°,   b $\sim$ - 4.46°)   which is in good agreement with
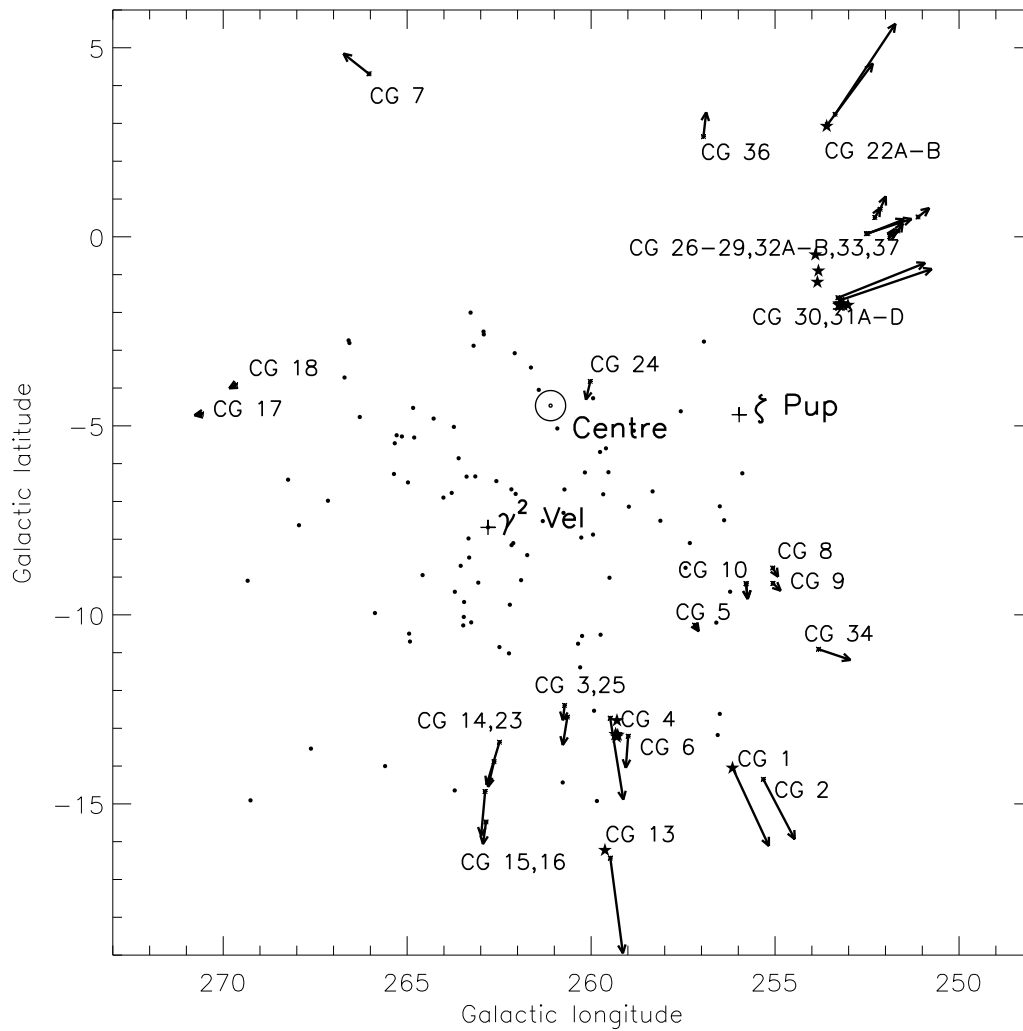
Figure 3.1 Distribution of CGs in the Galactic coordinate. The tail vectors have lengths proportional to the tail lengths of the respective CGs. *Filled Circles* represent the members of the Vela OB2 association. *Stars* represent the Young Stellar Objects around the CGs. Positions of ζ Pup and γ^2 Velorum are also marked .

the centre coordinate $(l \sim 261.5°$, $b \sim - 4.0°)$ obtained by Woermann et al. (2001). We have also adopted the approximate centre of the Vela OB2 association as RA(2000) = $08^h07^m00.22^s$ Dec(2000) = - 46°41′53.8″ $(l \sim 262.3°$, $b \sim - 7.71°)$.

Reipurth (1983) proposed a mechanism for the formation and evolution of the CGs based on the interaction of the massive stars and their parent molecular cloud. (Brand et al., 1983) proposed that the cometary morphology has been created by the passing of shock wave through a spherical molecular cloud. They also suggested the possibility of star formation in the shocked molecular clouds. Analytical models (also known as the Radiation Driven Implosion (RDI) models) have been developed by Bertoldi (1989) and Bertoldi & McKee (1990). Lefloch & Lazareff (1994) studied the evolution and morphology of the cometary globules by a 2-d hydrodynamic simulation. These models could not reproduce the details of triggered star formation by the UV radiation because they did not include the effect of

self gravity. Miao et al. (2006) have shown the evolution of the cometary globules as well as the triggered star formation under the influence of the UV radiation of the massive stars by a 3-d smoothed particle hydrodynamics (SPH) simulation.

According to these models, when an OB association forms in a comparatively dense core of a clumpy Giant Molecular Cloud (GMC) its interaction with its parent molecular cloud can be destructive or constructive depending on the size and density distribution of the leftover clumps and cores of the parent GMC. The UV radiation from the massive young stars evaporates the gas and less dense material in its surroundings and creates an expanding Strömgren sphere. But it cannot evaporate the relatively dense cores of the clumpy parent cloud because of the recombination shielding of the front layer known as the ionized boundary layer [IBL] (Elmergreen, 1976). However, the ionized gas starts to move towards the ionizing source and due to momentum conservation the clumps also get a velocity radially outward from the central star. This mechanism is known as Rocket Effect (Oort & Spitzer, 1955). The rocket effect pushes the loosely bound gaseous envelope much more effectively than the dense core. The expanding Strömgren sphere also creates a shock wave which interacts with the leftover remnant clumps and converts them into more dense regions. As a result a newly exposed dense core generally has a thin ionized layer and a tail in the opposite direction created by the leftover material of the parent GMC. At the same time the compression by the shock front can trigger the next generation star formation in the dense core. It thus provides the additional external pressure force to the gravity to collapse the clumps to form stars. This process of star formation is known as triggered star formation as opposed to the spontaneous star formation where only gravity is responsible for the collapse of the cloud core. Also the low mass stars which have formed in these globules simultaneously with the massive stars are exposed to photoevaporation.

Considerable evidence for current low mass star formation in the cometary globules of the Gum Nebula is discussed in the following section.

3.3 Young Stellar Objects in and around the Cometary Globules

Photometric and spectroscopic studies to investigate the low mass star formation in the Cometary Globules have been undertaken by Pettersson (1987), Sahu & Sahu (1992), Reipurth (1983),Reipurth & Pettersson (1993), Kim et al. (2005). Based on Hα emission line, Li absorption line and near IR infrared excesses, $\sim$ 30 YSOs have been identified in the direction of the Gum Nebula. There are confirmed signatures of the low mass star formation in the globules; e.g. CG 1 (Reipurth, 1983), CG 22 [Sahu & Sahu (1992), Reipurth (1983),Reipurth & Pettersson (1993)], CG 30/31/38 complex [Reipurth & Pettersson (1993),Pettersson (1987), Kim et al. (2005)], CG 4/CG 6/Sa101 and CG 13

Reipurth & Pettersson (1993). We have tabulated the optical and near IR photometric measurements of the individual YSOs in the Table 3.1. We also include the spectral types and the measured Hα equivalent widths in the Table 3.1. Near IR magnitudes are taken from the 2MASS Point Source Catalog Cutri et al. (2003). Except for NX Pup which is of spectral type A, the other YSOs found near the CGs are all late type stars with spectral types F, K and M. We also tabulate some useful parameters related to the known star forming CGs and dark clouds in Table 3.4.

Pettersson (1987) made photometric, spectroscopic and infrared observations of 16 Hα emission line stars in the region near the cometary globules CG 30/31/38. They identified 9 T Tauri stars. They also found that except PHa 12 and PHa 44 all other spectroscopically confirmed YSOs are variable in V band. PHa 41 has shown optical variability of $\sim$ 3 mag. and PHa 15, PHa 21, PHa 34, PHa 41 have large (U-B) excesses.

Reipurth & Pettersson (1993) surveyed five fields in the Gum Nebula for low mass emission line stars. They found 7 Hα emission line stars near the CG4/CG6/Sa 101 cloud complex and one more near CG 13. They confirmed the nature of the objects as the low-mass young stars [RP93] based on the low resolution spectra, optical and near IR photometry.

Kim et al. (2005) presented photometric and spectroscopic observations of low mass pre-main sequence stars in the cometary globules CG 30/31/38. They identified PMS stars in that direction by photometric and spectroscopic studies. They confirmed the youth of the PMS stars using the lithium abundances. They also measured the radial velocities of the PMS stars which are consistent with those of the cometary globules. However, Kim et al. (2005) also suggested that XRS 9, KWW 1055, KWW 1125, KWW 1333 and KWW 1806 are probably old field stars (50-100 Myr) with strong magnetic activity. We do not consider these objects in further discussion.

There are two YSOs, NX Pup and PHa 92, which are of some special interest. From the Figure 3.4 and Figure 3.5 it seems very likely that they are embedded in the heads of CG 1 and CG 22 respectively. Both the stars show associated reflection nebulosities, Hα emission line and near IR excess. Based on these observations Reipurth (1983) concluded that NX Pup is a YSO formed in CG 1. Sahu & Sahu (1992) also confirmed that PHa 92 is a T-Tauri star formed in CG 22. As these two YSOs are still associated with the respective CGs we can use the proper motion of the two stars as the transverse motion of the respective CGs. The formation and evolutionary models of the CGs predict a net radially outward motion . The CG tails are also directed radially outward. It should be noted that the tail formation is a relatively fast process and, therefore, the tail direction is determined by the current position of the cloud and the exciting star, while the direction of motion of the star born in the CG would be determined by the initial velocity of the cloud (inertia) and prolonged acceleration, if any, due to the winds, radiation and supernova shocks of massive stars.

Table 3.1. Photometric and spectroscopic properties of YSOs associated with CGs and Diffuse Molecular Clouds

No.	Name	V	Spectral Type	$W_\lambda(H\alpha)$ Å	J^b mag	H^b mag	K^b mag	Ref.[a]
1	NX Pup	10.61[1]	A0[1]	-44.0[5]	8.579 ±0.030	7.285±0.042	6.080 ±0.031	1,5
2	KWW 464	15.82	M3V	-2.8	12.126±0.024	11.392±0.026	11.173 ±0.026	2
3	KWW 1892/PHa 12	15.17	M1V	-26.6/-31.3	11.402±0.023	10.663±0.023	10.323 ±0.021	2,3
4	KWW 598	17.27	M2V	-11.5	12.150±0.024	11.519±0.023	11.281 ±0.023	2
5	KWW 1863	14.65	M1V	-2.8	10.873±0.028	10.194±0.033	9.940 ±0.024	2
6	KWW 1637	12.15	K6V	-2.4	9.529±0.023	8.880±0.022	8.708 ±0.024	2
7	KWW 873	13.81	K7V	-7.9	10.676±0.023	9.947±0.023	9.578 ±0.023	2
8	KWW 1043/PHa 15	16.61	M3V	–	11.925±0.028	11.135±0.025	10.628 ±0.024	2,3
9	KWW 975/Pha 14	15.56	M2V	-8.43	11.387±0.022	10.640±0.025	10.299 ±0.023	2,3
10	KWW 1302	15.76	M4V	-8.23	11.500±0.032	10.761±0.036	10.429 ±0.023	2
11	KWW 1953	15.58	M3V	-4.24/ -4.93	11.438±0.023	10.722±0.022	10.510 ±0.023	2
12	KWW 2205	16.20	M4V	-4.34	11.780±0.023	11.122±0.022	10.840 ±0.021	2
13	KWW XRS 9	–	G5V	3.23	9.783 ±0.021	9.464±0.022	9.346 ±0.023	2
14	KWW 1055	14.40	G2V	2.17	12.424±0.026	12.028±0.025	11.890 ±0.023	2
15	KWW 314	15.14	A3e	6.2	12.546±0.024	12.155±0.023	11.931 ±0.026	2
16	KWW 1125	12.35	<F8V	5.75	11.285±0.023	11.085±0.023	11.015 ±0.023	2
17	KWW 1333	13.64	<F8V	5.23	12.074±0.024	11.788±0.027	11.694 ±0.026	2
18	KWW 1806	13.99	<F8V	0.81	12.262±0.028	11.820±0.031	11.678 ±0.027	2
19	PHa 44	15.8	K7-M0	-50.7	12.996±0.028	12.175±0.027	11.713 ±0.019	3
20	PHa 51	15.7	K7-M0	-70.1	12.664±0.027	11.730±0.023	11.090 ±0.024	3
3	PHa 12	15.5	M1.5	-16.1	11.402±0.023	10.663±0.023	10.323 ±0.021	3,2
21	PHa 21	16.4	M4	-48.1	12.212±0.026	11.420±0.022	11.058 ±0.023	3
22	PHa 34	15.6	K3	-60.5	12.439±0.029	11.642±0.026	11.031 ±0.023	3
23	PHa 40	16.4	M0.5	-18.7	12.750±0.024	11.759±0.022	11.326 ±0.021	3
24	PHa 41	14.0	–	-98.6	10.775±0.024	9.806±0.022	8.914 ±0.024	3
8	PHa 15	16.9	M3	-130.5	11.925±0.028	11.135±0.025	10.628 ±0.024	3,2
9	PHa 14	16.4	M2	-22.0	11.387±0.022	10.640±0.025	10.299 ±0.023	3,2
25	PHa 92	13.38	K2	-35.4	10.573±0.023	9.692±0.024	9.044 ±0.021	3
26	[RP93] 1	>17	M3-4	-24.8	11.378±0.023	10.716±0.025	10.406 ±0.023	4
27	[RP93] 2	>17	M2	-266.5	12.855±0.021	11.932±0.021	11.404 ±0.020	4
28	[RP93] 3	14.99	K7	-27.0	11.204±0.022	10.218±0.021	9.582 ±0.020	4
29	[RP93] 4	14.59	K7-M0	-19.3	11.423±0.033	10.669±0.042	10.244 ±0.031	4
30	[RP93] 5	15.25	K2-5	-126.9	11.959±0.026	10.820±0.030	10.020 ±0.023	4
31	[RP93] 6	14.21	K7	-5.0	10.445±0.022	9.531±0.022	9.111 ±0.025	4
32	[RP93] 7	13.97	K5	-9.8	11.491±0.023	10.739±0.023	10.352 ±0.025	4
33	[RP93] 8	15.33	M1-2	-42.1	11.830±0.027	11.066±0.024	10.832 ±0.021	4

[a]Ref: 1: Hillenbrand et al. (1992), 2: Kim et al. (2005), 3: Pettersson (1987), 4: Reipurth & Pettersson (1993), 5: Manoj et al. (2006)

[b]JHK measurements from the 2MASS ALL-Sky Release Point Source Catalog.

Here we have used the proper motion measurements of the YSOs to study the kinematics of the CGs and effects of earlier events in the region on these objects, if any.

3.4 Proper Motion of the Young Stellar Objects

We have collected the available proper motion data on the confirmed YSO candidates from the Naval Observatory Merged Astrometric Dataset (NOMAD) Zacharias et al. (2004) catalog. We have selected only those YSOs whose proper motion of at least one component is greater than the error of the measurements given in the catalog. We have also considered the catalog by Ducourant et al. (2005) for the proper motion of the Pre-Main Sequence (PMS) stars. The best measurements (smallest error) available in the two catalogs have been selected. However, (NOMAD) does not have the measurements for NX Pup. We have taken the proper motion measurements for NX Pup from Tycho 2 catalog (Hog *et al.* ,2000). For the stars taken from NOMAD catalog, we have converted their proper motion to the galactic coordinates by the formula as described by Mdzinarishvili & Chargeishvili (2005).

We tabulate the identification number, name, radial distance from the respective star to the NOMAD counterpart (r), equatorial coordinates, proper motion measurements and the associated errors in the respective columns of Table 3.2 . The observed differential proper motions of the YSOs with respect to the mean proper motion of the Vela OB2 are tabulated in Column (10) and Column (11). The proper motion measurements in galactic coordinates are included in Column (12) and Column (13) and the differential proper motion of the YSOs with respect to the mean proper motion of the Vela OB2 in galactic coordinate are tabulated in Column (14) and Column (15).

We have tabulated the mean proper motions of the YSOs from Table 3.2 and the member of the Vela OB2 association (de Zeeuw et al., 1999) from Tycho 2 Catalog (Høg et al., 2000). From Table 3.3 its quite clear that mean proper motion of all the YSOs is not similar to that of the Vela OB2 members. We consider YSOs 2, 4, 11 and 29 as *High Velocity YSOs* due to their proper motions being greater than 2σ from the mean in both the components. We discuss the properties of *High Velocity YSOs* in detail in the Section 3.5. Excluding the *High Velocity YSOs*, the rest of the YSOs are termed as *Normal Velocity YSOs*. The mean proper motion of the *Normal Velocity YSOs* is similar to the mean motion of the members of the Vela OB2 association within the error limit associated with the measurements of the proper motion. We have plotted the histogram of the proper motion of both *Normal Velocity YSOs* and *High Velocity YSOs* with the Vela OB2 association in Figure 3.2.

The heliocentric velocity of the association $V_{helio} = 18$ km s^{-1} (de Zeeuw et al., 1999), which is equivalent to $V_{LSR} = 4$ km s^{-1}. The radial velocities of the CGs and Diffuse Molecular Clouds are taken from Sridharan (1992), Woermann et al. (2001) and Otrupcek et al. (2000) respectively. The mean V_{LSR} ($< V_{LSR} >$) of the CGs is 1.74 km s^{-1} with $\sigma_{V_{LSR}} = 4.73$. Among all the CGs, only CG 24 has radial velocity more than 2σ away from the mean. Excluding CG 24, $< V_{LSR} >$ for rest of the CGs is 2.13 with $\sigma_{V_{LSR}} = 4.13$. $< V_{LSR} >$ of the DMCs is 5 km s^{-1} with $\sigma_{V_{LSR}} = 6$ km s^{-1}. Out of the 106, 96 DMCs have values within 2σ of the calculated mean. $< V_{LSR} >$ of these 96 DMCs is 3.5 km s^{-1} with $\sigma_{V_{LSR}} = 4.52$ km s^{-1} . These values indicate that there is a good coupling between the CGs, DMCs and the members of the Vela OB2 associations. All these systems of objects have the same average motion.

Table 3.2 Proper Motion of the YSOs associated with Cometary Globules and Diffuse Molecular Clouds

No.	Name	RA (2000)	Dec (2000)	r arcsec	$\mu_\alpha cos\delta$ mas /yr	e mas /yr	μ_δ mas /yr	e mas /yr	$\Delta\mu_\alpha cos\delta$ mas /yr	$\Delta\mu_\delta$ mas /yr	$\mu_l cosb$ mas /yr	μ_b mas /yr	$\Delta\mu_l cosb$ mas /yr	$\Delta\mu_b$ mas /yr
1	NX Pup	07 19 28.26	-44 35 11.4	0.123	-4.2	2.0	6.1	1.9	2.22	-2.03	-7.08	-1.26	3.32	0.04
3	KWW 1892	08 08 22.15	-36 03 47.0	0.101	-6.5	4.8	7.7	4.7	-0.08	-0.43	-9.99	-1.29	0.41	0.01
6	KWW 1637	08 08 39.27	-36 05 01.7	0.259	-7.7	2.8	8.6	2.7	-1.28	0.47	-11.40	-1.81	1.00	-0.51
7	KWW 873	08 08 45.40	-36 08 40.2	0.024	-8.4	4.7	4.6	4.7	-1.98	-3.53	-8.42	-4.56	1.98	-3.26
8	KWW 1043	08 08 46.82	-36 07 52.8	0.354	-7.0	4.7	8.5	4.8	-0.58	0.37	-10.94	-1.27	0.54	0.03
9	KWW 975	08 08 33.87	-36 08 09.8	0.099	-5.9	4.8	12.3	4.8	0.52	4.17	-13.53	1.71	3.13	3.01
20	PHa 51	08 12 47.04	-36 19 17.9	0.069	-6.4	4.8	0.5	4.6	0.02	-7.63	-3.98	-5.03	2.59	-0.37
22	PHa 34	08 13 56.07	-36 08 02.1	0.061	-5.7	4.7	5.6	4.8	0.72	-2.53	-7.81	-1.67	4.06	-3.37
24	PHa 41	08 15 55.32	-35 57 58.1	0.014	-7.4	4.6	2.7	4.6	-0.98	-5.43	-6.34	-4.67	6.42	-3.73
25	PHa 92	08 28 40.70	-33 46 22.3	0.041	-6.6	4.6	10.4	4.6	-0.18	2.27	-12.30	0.71	1.90	2.01
28	[RP93] 3	07 31 10.81	-47 00 32.5	0.987	-6.7	5.0	10.9	4.9	-0.28	2.77	-12.73	-1.29	2.33	0.01
30	[RP93] 5	07 31 36.68	-47 00 13.2	1.104	-6.9	5.0	8.4	5.0	-0.48	0.27	-10.57	-2.54	0.17	-1.24
31	[RP93] 6	07 31 37.42	-47 00 21.5	0.541	-7.0	4.9	3.6	5.0	-0.58	-4.53	-6.29	-4.73	4.11	-3.43
32	[RP93] 7	07 33 26.86	-46 48 42.6	1.501	-3.2	4.9	11.1	4.9	3.22	2.97	-11.37	2.03	0.97	3.33
33	[RP93] 8	07 15 40.89	-48 31 27.3	0.363	-4.5	5.8	7.1	5.9	1.92	-1.03	-8.29	-1.39	2.11	-0.09
2	**KWW 464**	08 08 00.66	-35 57 33.3	0.404	-17.4	4.7	17.5	4.7	-10.98	9.37	-24.13	-5.17	-13.73	-3.87
4	**KWW 598**	08 08 37.60	-36 09 49.4	1.089	-10.0	18.0	24.0	5.0	-3.58	15.87	-25.59	4.61	-15.19	5.91
11	**KWW 1953**	08 08 26.93	-36 03 35.4	0.103	-13.0	4.9	13.1	5.0	-6.58	4.97	-18.05	-3.83	-7.65	-2.53
29	**[RP93] 4**	07 31 21.85	-46 57 43.9	1.177	-24.9	4.9	32.0	4.9	-18.48	23.87	-39.66	-8.47	-29.26	-7.17

Note: Differential proper motions are given with respect to Vela OB2 association. The **High Velocity YSOs (2, 4, 11, 29)** have been highlighted.

Table 3.3 Statistics of proper motion of the Young Stellar Objects and Vela OB2 members

Objects	$<\mu_\alpha \cos\delta>$ mas yr^{-1}	$\sigma(\mu_\alpha \cos\delta)$ mas yr^{-1}	$<\mu_\delta>$ mas yr^{-1}	$\sigma(\mu_\delta)$ mas yr^{-1}
All YSOS	-8.39	5.12	10.25	7.53
High Velocity YSOs	-16.33	6.47	21.65	8.23
Normal Velocity YSOs	-6.27	1.38	7.20	3.37
Vela OB2 members	-6.42	2.45	8.13	1.93

Table 3.4 Star forming CGs and Diffuse Molecular Clouds

CGs and the DMCs	l (°)	b (°)	V_{LSR} kms^{-1}	Vela OB2		γ^2 Vel		ζ Pup	
				Angular separation (°)	Projected distance (pc)	Angular separation (°)	Projected distance (pc)	Angular separation (°)	Projected distance (pc)
CG 1	256.14	-14.07	3.3	8.6	67	9.11	71	9.35	73
CG 30/31/38	253.29	-1.61	5.8-7	10.67	84	11.3	89	4.11	32
CG 22	253.58	+2.96	6.5-6.8	13.54	106	14.1	110	7.97	63
CG 13	259.48	-16.43	3.7	9.03	71	9.29	73	12.22	96
CG4/CG6/Sa101	259.48	-12.73	0.9-1.7	5.98	47	6.38	50	9.03	71

Note: V_{LSR} from Sridharan (1992). Projected distances are at 450 *pc*.

3.5 Discussion

Woermann et al. (2001) have suggested that the supernova explosion of the massive binary companion of the ζ Pup is responsible for the origin of the Gum Nebula. They estimated that the explosion took place $\sim$1.5 Myr ago. They also suggested that the runaway O-star ζ Pup was within $< 0.5°$ of the expansion centre of the neutral shell $\sim$1.5 Myr ago. As a first order estimate we have traced back the proper motion of ζ Pup and Pha 92 and NX Pup (embedded YSOs) in galactic coordinates, and calculated their angular separations. The angular separation of PHa 92 and NX Pup from ζ Pup as a function of time in the past are plotted in Figure 3.3. We do not see any indication of convergence between all three in the last 1.5 Myr . This trend suggests that the supernova explosion of the companion of the ζ Pup did not import any radial motion to the stars NX Pup and PHa 92. So the supernova explosion was not responsible for the bulk motion of CG 1 and CG 22 associated with NX Pup and PHa 92 respectively.

Woermann et al. (2001) also gave a likely configuration of the Gum nebula. They suggested that most of the CGs and the Vela OB2 association are situated within the front face of the expanding shell. The expected transverse velocity components of the two stars based on the radial velocities of the CGs and the expansion velocity of the system can be calculated using the following formula $\quad V_T = \sqrt{V_{exp}^2 - V_{radial}^2}$.
Considering V_{LSR} (CG 1) $= +3.3$ km s^{-1} and V_{LSR} (CG 22)$= 6.65$ km s^{-1} from Sridharan (1992) and $V_{exp} = 14$ km s^{-1} for the front face from Woermann *et al.* (2001), we obtain the expected transverse velocity components as V_T (CG 1)$= 13.6$ km s^{-1} and V_T (CG 22)$= 12.32$ km s^{-1}. These values corresponds to 5.78 and 6.38 mas yr^{-1} for CG 1 and CG 22 respectively with respect to the centre of explosion. Again, if CG 22 and CG 1 were close to the site of supernova explosion of the companion of ζ Pup 1.5 Myr ago then the proper motions of NX Pup and Pha 92 born in the respective CGs should be consistent with their motion from the site of the explosion to their present position. This would require a differential proper motion of NX Pup as $\Delta\mu_l cosb \sim$ - 30.09 mas yr^{-1}, $\quad \Delta\mu_b \sim$ - 36.23 mas yr^{-1} and PHa 92 as $\Delta\mu_l cosb \sim$ - 39.73 mas yr^{-1}, $\quad \Delta\mu_b \sim 1.01$ mas yr^{-1}. We do not have the proper motion of the binary companion of ζ Pup which is the suggested centre of the expansion. But the other O type star γ^2 Vel shares a similar kind of motion as Vela OB2. So it is reasonable to adopt the mean proper motion of Vela OB2 for the motion of the centre. Considering the mean proper motion of the Vela OB2, the expected proper motion of NX Pup is $\mu_l cosb \sim$ - 40.49 mas yr^{-1}, $\quad \mu_b \sim$ - 41.03 mas yr^{-1} and for PHa 92 it is $\mu_l cosb \sim$ - 50.13 mas yr^{-1}, $\quad \mu_b \sim 2.31$ mas yr^{-1}.

Considering the early type stars Yamaguchi et al. (1999) suggested the age of the association as less than 10 Myr. We also traced back the proper motion of Pha 92 and NX Pup from the γ^2 Velorum and the mean proper motion of the Vela OB2 association up to 15 Myr. Figure 3.3 also shows the angular separations of NX Pup and PHa 92 from γ^2 Vel and
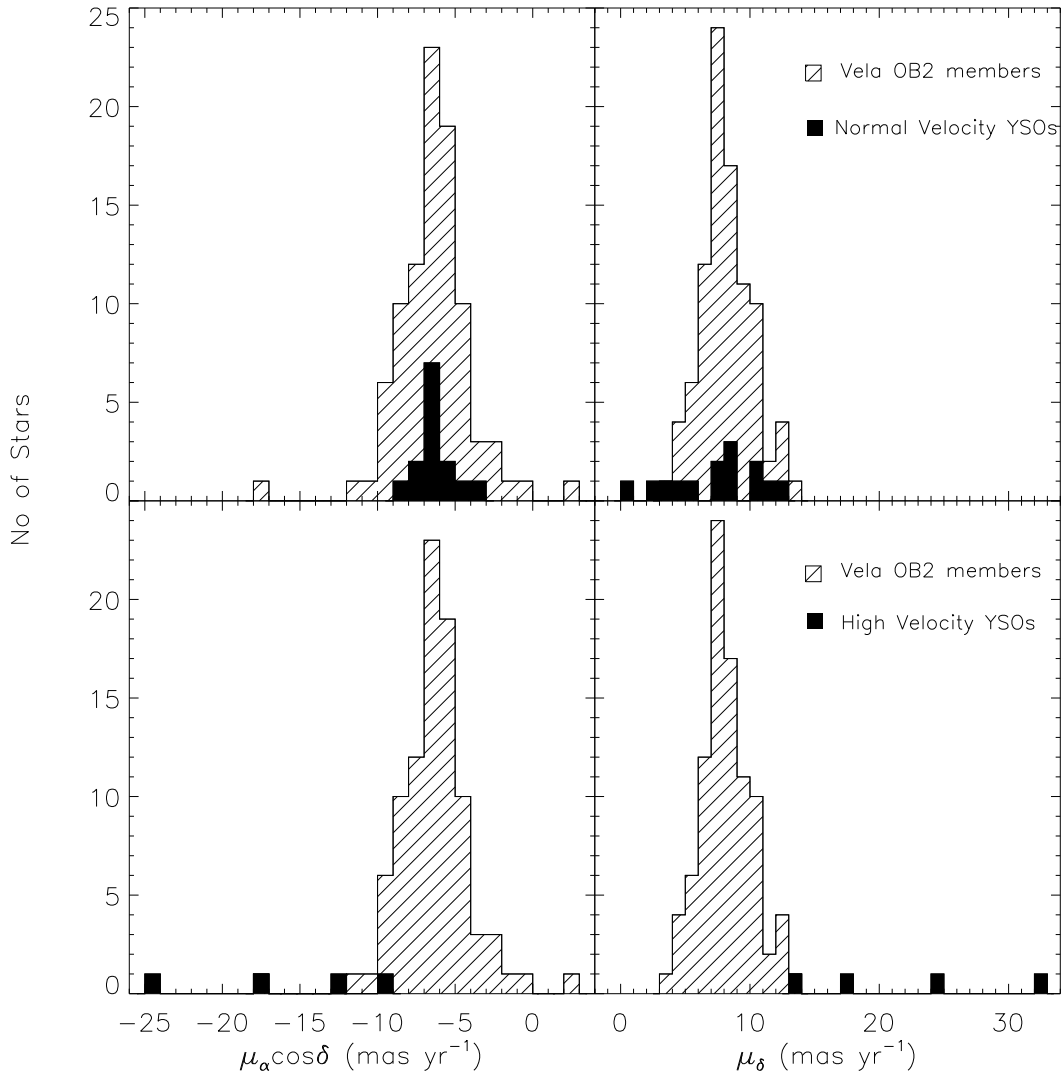
Figure 3.2 Proper motion histograms of *Normal Velocity YSOs, High Velocity YSOs*, and the members of Vela OB2 association. *Line-filled* histogram represent the members of the association and the *solid* histogram represent the YSOs.

Vela OB2 association. There is no indication of convergence of NX Pup with any of the sources (ζ Pup, γ^2 Velorum and Vela OB2) plotted in the diagram. However, the angular separation between the PHa 92 and the Vela OB2 association was shorter in the past than the present separation.

Adopting the proper motion of Vela OB2 for the motion of the centre, the observed differential proper motion of the stars with respect to the Vela OB2 association are estimated and tabulated in Table 3.2 (column 15 and 16). There is significant mismatch between the expected and observed differential proper motions of the YSOs with respect to the Vela OB association. For NX Pup the expected differential proper motion is $\Delta\mu_l cosb \sim$ -30.09 mas yr^{-1}, $\Delta\mu_b \sim$ -36.23 mas yr^{-1} while the observed differential proper motion is $\Delta\mu_l cosb$ $\sim$ 3.32 mas yr^{-1}, $\Delta\mu_b \sim$ 0.04 mas yr^{-1}. For PHa 92 the expected differential proper
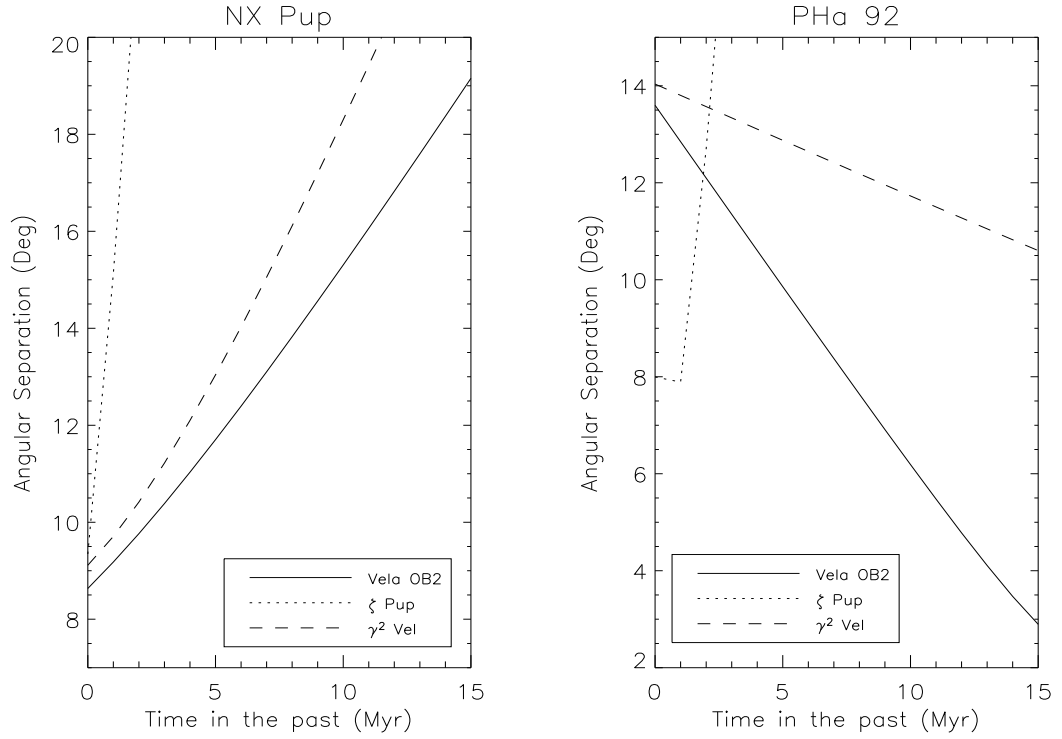
Figure 3.3 Angular separation of NX Pup and PHa 92 from ζ Pup, γ^2 Vel and Vela OB2 association in look back time. The dotted, dashed and solid lines represent the angular separation from ζ Pup, γ^2 Vel and Vela OB2 association respectively.

motion is $\Delta\mu_l cosb \sim$ -39.73 mas yr^{-1}, $\Delta\mu_b \sim$ 1.01 mas yr^{-1} while the observed differential proper motion is $\Delta\mu_l cosb \sim$ 1.90 mas yr^{-1}, $\Delta\mu_b \sim$ 2.01 mas yr^{-1}. For other YSOs, the expected differential proper motion $|\Delta\mu| \sim$ 30 mas yr^{-1} while the observed differential proper motion is $|\Delta\mu| \sim$ 5 mas yr^{-1} .

The proper motion vector *P1* of NX Pup [Star identification No. 1 in Table 3.1] is plotted on the DSS image of CG 1 in Figure 3.4. The differential proper motion vector *D1* of NX Pup with respect to Vela OB2 association is also plotted Figure 3.4. The proper motion vector *P25* of PHa 92 [Star identification No. 25 in Table 3.1] is plotted on the DSS image of CG 22 in Figure 3.5. The differential proper motion vector *D25* of PHa 92 with respect to the Vela OB2 association is also plotted in Figure 3.5. The directions towards the Vela OB2 association and ζ Pup are also shown in Figure 3.4 and Figure 3.5. Within the errors associated with the proper motion measurements we do not find any clear evidence for the transverse motion for these two stars away from the site of supernova explosion of the companion of ζ Pup. For the objects which are not embedded in any CGs but supposed to be associated with the Gum Nebula, we get similar results. They also do not show any indication of expansion within the errors of proper motion measurements. This suggests that the system of CGs share the mean motion of Vela OB2 and do not show any systematic radial motions away from the centre.

We have also found 3 high velocity YSOs in CG 30 complex and one more in Sa 101. They
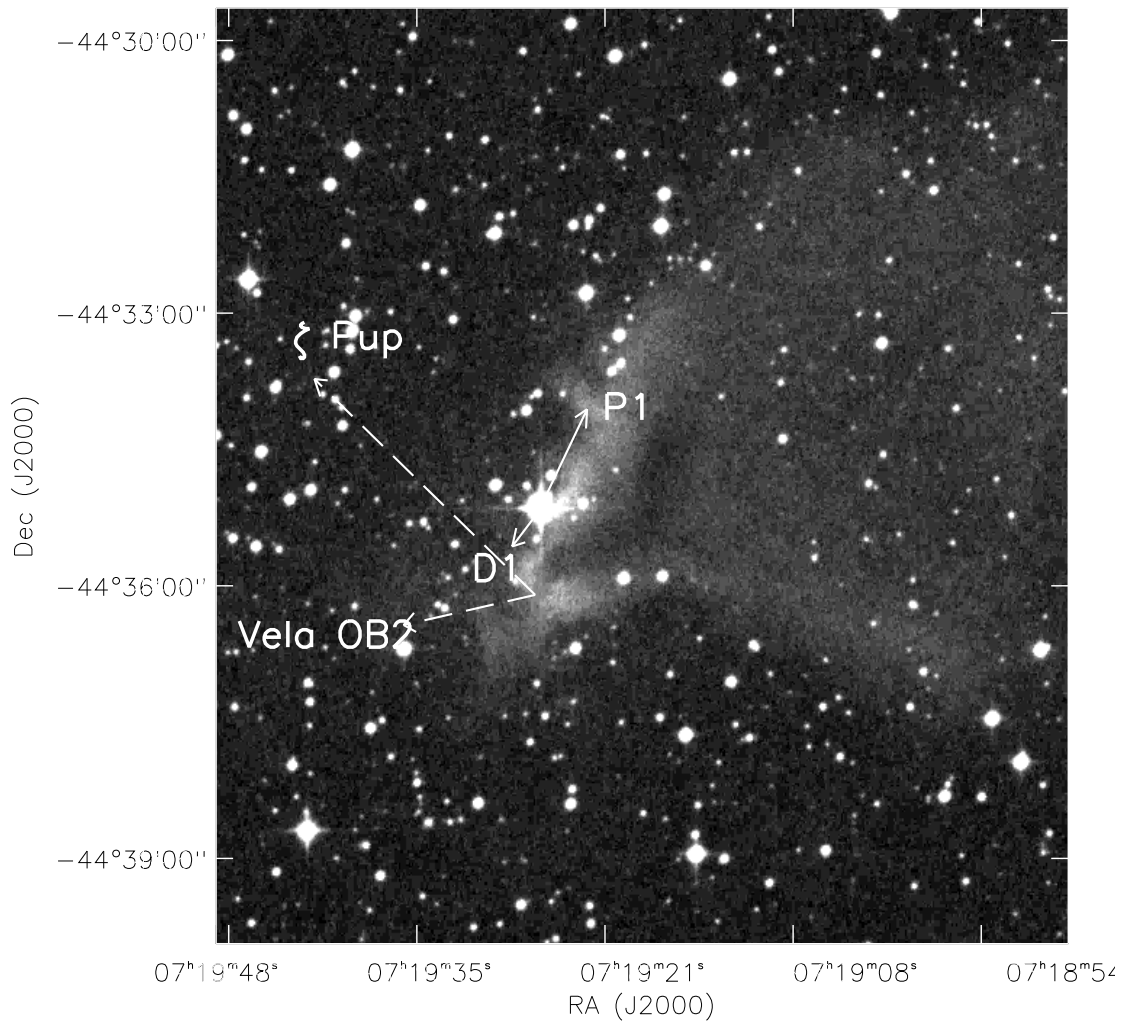
Figure 3.4 The proper motion vector *P1* of NX Pup plotted on the DSS image of CG 1. The directions towards the Vela OB2 association and ζ Pup are also shown by *dashed* lines. The differential proper motion vector *D1* is also plotted. Arrow lengths are proportional to the respective proper motion.

have proper motion measurements more than 3σ away from the the mean proper motion of the Vela OB2. For the stars in the CG 30 complex Kim et al. (2005) have estimated an age of 2-5 Myr. These YSOs have Hα emission line as well as Li absorption line indicating youth. Figure 3.6 gives a near IR J-H vs. H-K color-color (CC) diagram of the known YSOs in and around the CGs with reliable NIR photometry as given in Table 3.1. High velocity stars are marked with diamond and their corresponding identification number, as given in the Table 3.1. We exclude the high velocity star [RP93] 4 from the CC diagram due to poor measurements. The location of normal main-sequence and giant stars from Bessell & Brett (1988) are modified to the 2MASS photometry as suggested by Carpenter (2001) and plotted with solid and dash dot lines respectively. Points marked with *plus* on the dashed line are at an interval of A$_v$ = 5 mag. Lee et al. (2005) have developed
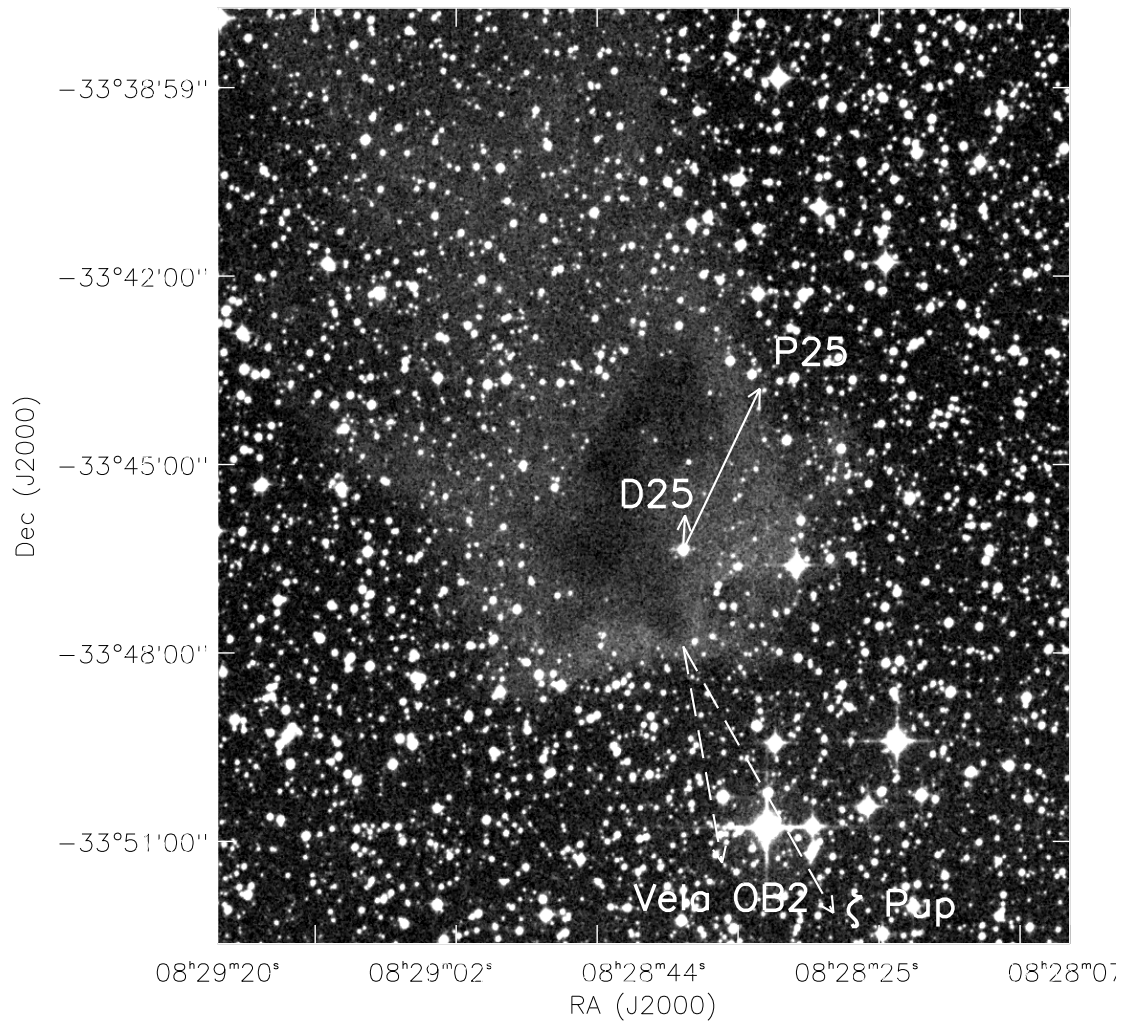
Figure 3.5 The proper motion vector *P25* of PHa 92 plotted on the DSS image of CG 22. The directions towards the Vela OB2 association and ζ Pup are also shown by *dashed* lines. The differential proper motion vector *D25* is also plotted. Arrow lengths are proportional to the respective proper motion.

an empirical and effective set of criteria, based on the 2MASS colors, to select candidate Classical T Tauri Stars (CTTSs). They found that the CTTS lie approximately between the two parallel dashed lines, defined empirically by $(j\_m - h\_m) - 1.7(h\_m - k\_m) + 0.0976 = 0$ and $(j\_m - h\_m) - 1.7(h\_m - k\_m) + 0.450 = 0$, where j_m, h_m, and k_m are 2MASS magnitudes, and the slope is specified by the interstellar reddening law (Rieke & Lebofsky, 1985). The *dash dot dot* line in the CC diagram represents the dereddened CTTS locus Meyer et al. (1997) , modified to the 2MASS photometry (Carpenter, 2001) with $(j\_m - h\_m) - 0.493(h\_m - k\_m) - 0.439 = 0$. The dashed parallel lines separate CTTS from Herbig Ae/Be and from reddened main sequence stars. Positions occupied by the objects in the CC diagram give primary information about the nature of the YSOs. NX Pup (Herbig Ae) and PHa 92 (T Tauri) both have near IR excesses and their positions
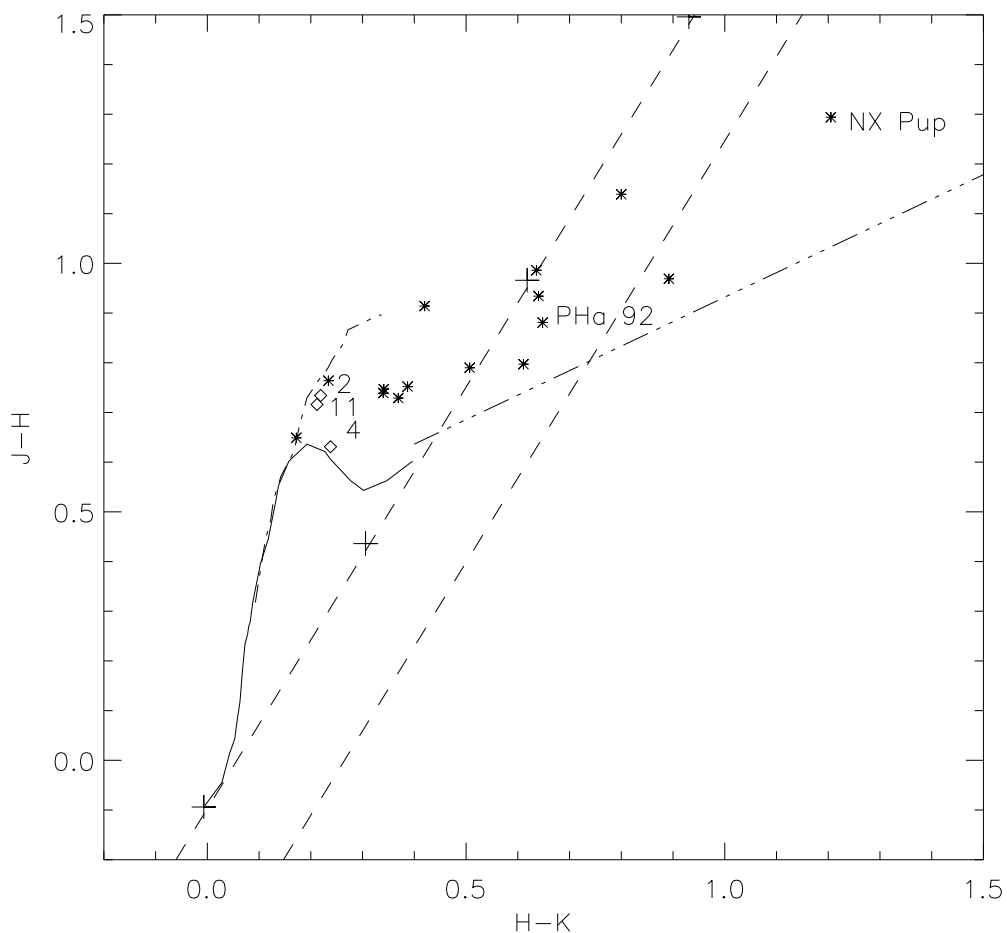
Figure 3.6 2MASS JHK color-color diagram for the known YSOs in and around the CGs with reliable NIR photometry. High velocity stars are marked with diamond and their corresponding number from Table 3.1. *Solid* and *dash dot* curves are the locations of main-sequence and giant stars from Bessell & Brett (1988) converted into 2MASS as suggested by Carpenter (2001). The two *dashed* parallel lines, with the slope derived from interstellar reddening law Rieke & Lebofsky (1985), separate CTTSs from Herbig Ae/Be and from reddened main-sequence stars Lee et al. (2005). The *dash dot dot* line is the dereddened CTTS locus (Meyer et al., 1997). Points marked with plus on the dashed line are at an interval of $A_v = 5$ mag.

in the CC diagram also match with the criteria suggested by Lee et al. (2005) to select Herbig Ae/Be and T Tauri stars based on near IR excesses emission. It is interesting to note that most of the YSOs which have similar proper motion as Vela OB2, show near IR excesses but all the three high velocity YSOs occupy similar positions in the CC diagram and they do not show near-infrared excesses. But there are no significant differences in Hα or Li equivalent widths and radial velocities of these objects compared with the other stars and the CGs (Kim et al., 2005). If they are indeed associated with the CG 30 complex then they perhaps owe their high velocities to the process of star formation in the cloud which is not understood. It may also be possible that the cause of their high proper motion affected their circumstellar environment and as a result they do not have infrared excesses.

There have been suggestions that during the star formation in binary or multiple systems YSOs can gain high velocities due to dynamical interactions [Sterzik & Durisen (1995), Gorti & Bhatt (1996), Reipurth (2000)]. But CG 30 lies close to galactic plane . So it is also possible, though less unlikely, that these objects are foreground YSOs moving with relatively higher velocities and large proper motions.

3.6   Conclusion

In the analysis presented above no clear evidence is found for the supernova explosion of the binary companion of ζ Pup causing expansion of the system of CGs in the Gum Nebula. We also do not find any systematic transverse expansion of the YSOs and the CGs in the Gum Nebula. It is possible that the CGs retain the initial velocities of their parent clumps inside the GMC characterized by a velocity dispersion as seen in the radial velocities. The energy sources in the Gum Nebula (stellar wind, radiation and supernova explosions) perhaps sweep out the diffuse material but not the relatively dense and massive CGs. The absence of CGs within some radius ($\sim$ 9 °) of the OB association would then require destruction due to evaporation by the UV radiation (Reipurth, 1983) from the central energy sources.

Interaction of Pre-Main Sequence Stars with Circumstellar Environment

Chapter 4

Signatures of Accretion and Outflow in Hα Emission Line Profile: Case of V351 Ori

4.1   Introduction

In Chapter 1, we briefly discuss the interaction of Pre-Main Sequence (PMS) stars with their circumstellar environment. We also describe the importance of accretion and outflow processes in the evolution of the PMS stars in Sec. 1.2.1. In this chapter, we focus on the observational evidence of interaction of PMS stars with their circumstellar environment. We selected to observe Herbig Ae star V351 Ori to understand the timescales and kinematics of the gaseous material involved in accretion and outflow processes.

Herbig Ae/Be (HAeBe) stars are revealed PMS emission line stars with masses of $\sim$1.5 to 10 M$_\odot$ and typical ages of $\sim$10^6 years with spectral types earlier than *F0*. Balmer emission lines of hydrogen and infrared (IR) excess emission produced by thermal emission of circumstellar dust grains are the prominent characteristics of HAeBe stars. Both of these signatures originate due to the circumstellar material around these stars and the interaction between them. It has been well established that circumstellar material, i.e. dust and gas around the HAeBe stars, are distributed in disks (e.g. Maheswar et al. (2002) and references therein). Significant variations in shape and intensity of permitted and forbidden emission line profiles, originating in the accretion or outflow events of the interaction between the central star and its surrounding material, are observed in many HAeBe stars (Hamann & Persson, 1992; Hamann, 1994; Reipurth et al., 1996). Optical spectroscopic studies of emission line profiles of a few HAeBe stars are reported in the literature in e.g. Grinin et al. (1994); de Winter et al. (1999); Grinin et al. (2001); Natta et al. (2000); Mora et al. (2002, 2004); Guimarães et al. (2006). Natta et al. (2000) reported the evidence for episodic rather than continuous accretion in Herbig Ae star UX Ori. Mora et al. (2002, 2004) reported

transient absorption components (TACs) in several Balmer and metallic lines of a few Herbig Ae type stars, which are thought to be created by moving gaseous blobs around these stars. These studies have discussed the dynamical circumstellar environment around HAeBe stars which show strong Hα emission.

Manoj et al. (2006) showed that the emission line activity of HAeBe stars substantially decreases on a timescale of $\sim$3 Myr. Hernández et al. (2005, 2009) estimated the inner disk survival timescale as $\sim$3 Myr for the early spectral type stars such as B, A, and F types. The dissipation of optically thick disks beyond $\sim$3 Myr to the onset of young main sequence stars with a debris disk can be caused by various disk dispersal processes such as accretion and outflows, photoevaporation, planet formation, etc. HAeBe stars with weak emission lines and moderate IR excess can be considered as the precursors of the young main sequence stars with IR excess and no gaseous emission lines, e.g. *β Pic* and *Vega*. Understanding the nature of accretion and circumstellar material of comparatively less active HAeBe stars of age $\geq$ 3 Myr are important because these processes eventually set the stage for planet formation. However, detailed studies, specially time variabilities of weak emission line HAeBe stars that cover hours, days, and months are not available in the literature. In this chapter we discuss the interaction of Herbig Ae star V351 Ori with its circumstellar environment.

V351 Orionis (V351 Ori, HIP 27059, HD 38238) is a weak Hα emission line Herbig Ae star that showed photometric and spectroscopic variabilities over various timescales (e.g. van den Ancker et al. (1996); Balona et al. (2002) and references therein). The classification of V351 Ori as a Herbig Ae star has been confirmed by several authors, e.g. van den Ancker et al. (1996); Vieira et al. (2003); Hernández et al. (2005). Grady et al. (1996) analyzed the ultraviolet (UV) spectra of V351 Ori and did not find any absorption component, i.e. signatures of stellar wind or accretion, in the spectra. van den Ancker et al. (1996) presented photometric and spectroscopic observations of V351 Ori and found that it transformed into an almost non-variable star from a strong photometric variable within a short period of $\sim$14 years. van den Ancker et al. (1996) reported that the Hα profile of V351 Ori was of an inverse P Cygni type and also showed a high infrared excess emission. Inverse P Cygni profiles are signatures of the accretion of circumstellar material onto the central object and are characterized by blue-shifted emission with red-shifted absorptions or systematically enhanced red shifted absorptions. V351 Ori shows δ Scuti type pulsation (Marconi et al., 2000), which is another characteristic of Pre-Main Sequence (PMS) stars of mass $\geq$ 1.5M$_\odot$ as they cross the pulsation instability towards their contraction to the main sequence. Balona et al. (2002) obtained simultaneous multi-colour photometric and spectroscopic observations of V351 Ori to investigate the nature of the pulsation of V351 Ori. Balona et al. also reported a variable inverse P Cygni type Hα profile with a variation on a timescale of a day with complete absence of emission at some epochs. Vieira et al. (2003) observed an inverse P Cygni type Hα emission line profile in V351 Ori and also suggested that V351 Ori

might be an evolved Herbig Ae star, because it shows weak emission lines. Hernández et al. (2005) also reported a low equivalent width of Hα i.e $EW_\lambda[H\alpha] = -0.9$ Å and associated V351 Ori with Ori OB1bc region. These signatures hint at an active interaction of the weak Hα emission line young star V351 Ori with its circumstellar environment.

In this chapter we present high-resolution spectroscopic observations of V351 Ori along with optical *BVRI* observations. We discuss the dynamic circumstellar gaseous environment of the star in the light of available models of star-disk interaction. Observations and data reduction are discussed in Sect. 4.2. In Sect. 4.3 we present the details of the spectra and the analysis of the Transient Absorption Component (TACs) detected in the spectra. A discussion of the kinematics of the observed TACs, an estimate of the disk mass and a qualitative interpretation of the Hα line profile variation are presented in Sect. 4.4. We present our conclusion in Sect. 4.5.

4.2   Observations and Data Reduction

45 high-resolution spectra of V351 Ori were obtained during October 2008 to April 2009 with a fibre-fed cross-dispersed echelle spectrometer (Rao et al., 2005) at the Vainu Bappu Telescope (VBT) of Vainu Bappu Observatory (VBO), Kavalur, India[1]. VBT is a 2.3m aperture optical telescope, equipped with the fibrefed coude echelle spectrometer. The main dispersing element is a spectrometer that consists of a 408×204 mm^2 echelle grating of 52.6 gr/mm with a blaze angle of 70 degree. The input beam size is 150 mm. The star light is fed to the spectrometer from the prime focus of the telescope by an optical fibre. Spectra of resolution R ∼ 30,000 – 100,000 can be obtained by varying the slit width. The resolving power of the spectrometer set-up used for observation is ∼28,000 and the attached 2K×4K CCD gives a dispersion of ∼0.025 Å per pixel. The typical integration time of each spectrum was 45 minutes. The log of the observations is given in Table 4.1. Bias subtraction, flat field correction and scatter light removal were carried out for all the spectra with the standard tasks available in the Image Reduction and Analysis Facility (IRAF)[2]. The Th-Ar lamp was used for wavelength calibration. The final spectra that were used for our analysis cover the wavelength region from λ4250 Å to λ7900 Å. The CCD used for observation did not cover the full echelogram, and as a consequence there are some gaps in the wavelength coverage of the observed spectra. However, we optimized the CCD position accordingly to cover the wavelength regions of Hα, *Hβ*, *NaD*1, *NaD*2 and several other photospheric lines. Atmospheric lines were also used to check the wavelength calibration. These wavelength calibrations of the final spectra are accurate up to ±0.01 Å.

---

[1] `http://www.iiap.res.in/vbo_vbt`

[2] The IRAF software is distributed by the National Optical Astronomy Observatory under contact with National Science Foundation. `http://iraf.noao.edu/`

Table 4.1 Observation log of the echelle spectroscopy of V351 Ori

Date	HJD − 2454000	t_{exp}(s)	Hα profile type[a]
2008-10-27	767.28 − 767.41	2700 x 4	IV-R,inverse P Cygni
2008-10-30	770.38	2700 x 1	II-R, double peak
2008-12-11	812.32	2700 x 1	IV-R
2008-12-28	829.10 − 829.32	2700 x 6	IV-R
2008-12-29	830.10 − 830.37	2700 x 8	IV-R
2009-01-17	849.11 − 849.22	2700 x 4	III-R, double peak
2009-01-18	850.10 − 850.32	2700 x 4	III-R
2009-01-19	851.09 − 851.35	2700 x 5	III-R
2009-01-20	852.07 − 852.18	2700 x 2	III-R
2009-03-02	893.11 − 893.15	2700 x 2	III-R
2009-03-03	894.20	2700 x 1	II-R
2009-03-29	920.16	2700 x 1	IV-R
2009-03-30	921.07 − 921.11	2700 x 2	II-R
2009-03-31	922.08	2700 x 1	III-R
2009-04-26	948.07	2700 x 1	III-R
2009-04-27	949.07	2700 x 1	II-R
2009-04-28	950.07	2700 x 1	II-R

a. Based on the classification scheme adopted from Reipurth et al. (1996). Type II-R profile represents a double peak profile where the red-sided peak exceeds the strength of the blue-sided peak by half. Type III-R also represents double peak profile with the red-sided peak less than half the strength of the blue-sided peak. Type IV-R represents the inverse P Cygni profile.

V351 Ori was observed on 11 November 2009 with the Bessell broad band filters B (5×5 s), V (4×2 s), R (4×1 s) and I (5×1 s) of the Himalayan Faint Object Spectrograph Camera (HFOSC) mounted on the 2m Himalayan Chandra Telescope (HCT) of the Indian Astronomical Observatory (IAO), Hanle, India[3]. Data were reduced with the standard tasks in IRAF.

4.3　Results and Analysis

4.3.1　Description of Echelle Spectra

HAeBe stars show both short and long term variabilities in their spectra. To explore the short to long term variations of the line profiles we obtained high-resolution spectra on timescales as short as an hour to the longest coverage of ∼7 months. All 45 spectra cover the wavelength regions of Hα, $H\beta$, $NaD1$, $NaD2$ and several other photospheric lines. Typical signal- to-noise ratios (S/N) are < 10 to 12 at $H\beta$, 15 to 30 at $NaD1$ and $NaD2$ and ≥ 30 to 60 at Hα. We note that [O I] $\lambda6300$ Å emission line was present in several spectra. Balona et al. (2002) also reported the detection of a narrow emission line of [O I] $\lambda6300$ Å at a velocity of +7.5 km s^{-1}. However, the line center of [O I] $\lambda6300$ Å in our

---

[3] http://www.iiap.res.in/centers/iao

observed spectra remained constant at laboratory wavelength, as did the other telluric lines throughout our observing runs. We therefore conclude that the [O I] $\lambda 6300$ Å emission line in our observed spectra is of telluric origin. We did not find any detectable emission in the $H\beta$, $NaD1$ and $NaD2$ line profiles, including the other photospheric lines typical to an A7 type stars within the noise level of our observed spectra. Though the Hα line profiles were dominated by variable absorption components, but nominal to significant variable emission components were also observed. Below we describe in detail the behavior of different line profiles. To compare the spectra obtained in different epochs one needs to normalize the spectra in a similar fashion. The normalization of the echelle spectra by fitting the continuum is tricky, because each order displays a limited wavelength coverage (in this case ~ 40 Å). However, with the synthetic spectra of the star as the guiding standard, a better fit to the continuum and accordingly a common normalization of all spectra can be obtained. As we shall discuss below, synthetic spectra are also essential to identify the circumstellar component in the line profiles that are dominated by absorption components.

4.3.2 Stellar Parameters and Synthetic Spectra

Balona et al. (2002) estimated the effective temperature (T_{eff}), rotational velocity (v sin i), and log g (logarithm of the surface gravity) of V351 Ori in order to generate the synthetic spectra of the star. Ripepi et al. (2003) estimated effective temperature (T_{eff} $\sim$7425-7600 K) of the star using the pulsation models. The average effective temperature of Ripepi et al. matches quite well with the estimated value of 7500 K by Balona et al.. Recent studies on the stellar parameters of HAeBe stars showed that the typical value of log g is $\sim$4.0, which also gives a reasonable fit to the photospheric wings of the Hα and $H\beta$ profiles of emission line HAeBe stars. Model atmosphere from the Kurucz model atmosphere database[4] for an A7 III star with T_{eff} =7500 K (as adopted from Balona et al. (2002)) and log g= 4.00, v sin$i$=102 km s^{-1} (Balona et al., 2002) and a micro turbulent velocity of 2 km s^{-1} (as suggested by Dunkin et al. (1997)) have been used. Detailed synthetic spectra were computed with the interactive data language (IDL) interface SYNPLOT (I. Hubeny, private communication) to the spectrum synthesis program SYNSPEC Hubeny & Lanz (2000), utilizing the adopted Kurucz model atmosphere. The linelist provided in SYNSPEC is used to generate the synthetic spectra.

Synthetic spectra have been deconvolved with the rotational profile of V351 Ori and the instrumental profile of the echelle spectrometer with SYNPLOT and ROTINS[5]. In Figs. 4.1 and 4.2 we display some of the representative photospheric line profiles and overplot the convolved synthetic spectra. Because the observed photospheric and synthetic line profiles show a good match over long wavelength ranges, we did not attempt to fit the photospheric lines rigorously to obtain the stellar parameters. We used the convolved synthetic spectra

---

[4]`http://kurucz.harvard.edu/`
[5]`http://nova.astro.umd.edu/Synspec43/synspec-frames-rotin.html`
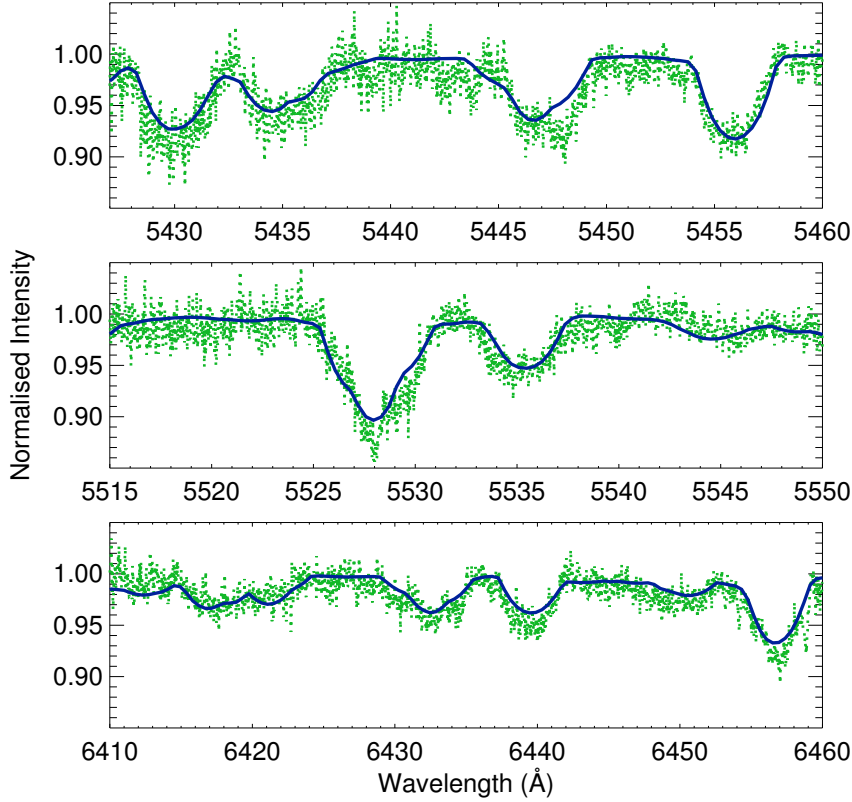
Figure 4.1 Average photospheric line profiles of V351 Ori on 29 December 2008 (*dotted green* line). Synthetic spectra in the same wavelength range are overplotted (*solid blue* line). The prominent photospheric lines are Fe I 5429.696, 5434.523, 5445.042, 5446.871, 5446.916, 5455.441 and 5455.609 in the first row, Sc II 5526.790, Mg I 5528.405 and Fe II 5534.847 in the second row, and Fe I 6430.844, Fe II 6432.680, Ca I 6439.075, and Fe II 6456.383 in the third row.

to identify unblended photospheric lines to obtain the radial velocity of the the star. Fe I, Fe II, and Ca I lines in a wavelength range from $\lambda 5000$ to $\lambda 6500$ Å [such as Fe II $\lambda 4923.827$ Å, Fe I $\lambda 5001.862$ Å, Fe I $\lambda 5429.696$ Å, Fe II $\lambda 5534.847$ Å, Fe I $\lambda 5615.644$ Å, Ca I $\lambda 6102.723$ Å, Ca I $\lambda 6122.217$ Å, Ca I $\lambda 6439.075$ Å] have been used to measure the radial velocity of the star. We estimate the average heliocentric radial velocity of the star as $+ 11^{+4}_{-3}$ km s^{-1}, which is similar to the estimated radial velocity i.e. $+ 13$ km s^{-1} by Balona et al. (2002). The photospheric Hα line profile have been synthesized following the same procedures.

4.3.3   Hα Line Profiles

We display all the Hα emission line profiles in the rest frame velocity of V351 Ori and overplot the photospheric components in Fig 4.3(a) to Fig 4.6(a). We also mark the spectra by their date of observation and the modified heliocentric Julian day (MHJD) defined by heliocentric Julian day (HJD)–2454000. We subtract the photospheric component from
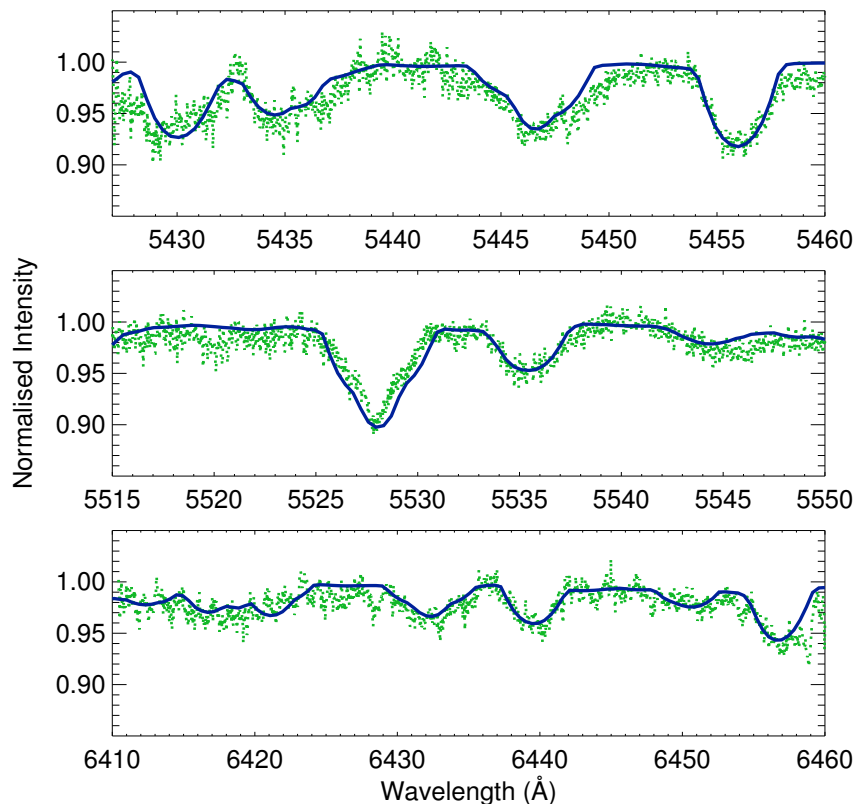
Figure 4.2 Average photospheric line profiles of V351 Ori of 17 to 19 January 2009 (*dotted green* line). Synthetic spectra in the same wavelength range are overplotted (*solid blue* line).

the observed spectrum and show the residual spectrum in Fig 4.3(b) to Fig 4.6(b). The zero level in the residual spectrum is described as the zero absorption level. As discussed before, profile variations on a timescale of days to months are quite common to V351 Ori. We also observed both blue- and red-shifted absorption components of various widths and depths in several epochs. These features are also seen in other HAeBe stars such as UX Ori, BF Ori, SV Cep, WW Vul, and XY Per, see e.g. Mora et al. (2002, 2004) and references therein. These features are called Transient Absorption Components (TACs) because they are sporadic in nature and last for a few days only. Transient absorption components can be divided into two categories, i.e blue-shifted absorption components (BACs) and red shifted absorption components (RACs). The chemical compositions and kinematics of the TACs have been discussed by several authors, e.g. Natta et al. (2000); Mora et al. (2002, 2004). We discuss the profile variations in detail in the subsequent sections. We quote the velocity of the broad wings from the residual spectra and that of the TACs from the observed normalized spectra.
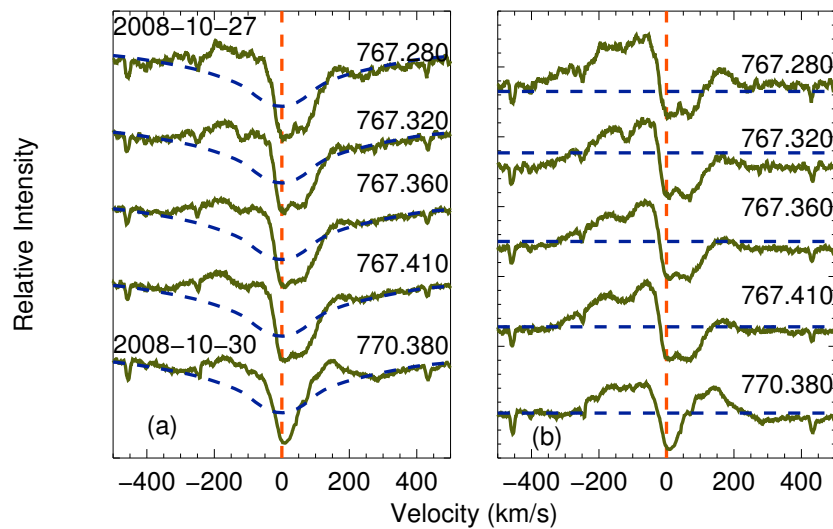
Figure 4.3 **(a)**. Hα line profiles (*green solid lines*) of V351 Ori of a couple of days in October 2008. The synthetic Hα line profiles (*blue dashed lines*) are overplotted on each spectrum. Modified Julian days are displayed against the respective spectrum. The *vertical red dashed line* represents the rest frame velocity of the star. **(b)**. Residual spectra of Hα line profiles in the same epochs. *Horizontal blue dashed lines* represent the zero absorption levels.

4.3.4 Line Profile Variations

Previous studies of e.g. van den Ancker et al. (1996), Balona et al. (2002), and Vieira et al. (2003) reported that the average Hα emission line profiles of V351 Ori were inverse P Cygni types. From Table. 4.1 it is evident that V351 Ori showed various profile shapes such as II-R and III-R, including inverse P Cygni types during our observation. Nightly variations of profiles from an average behavior at a timescale of a day were also observed in several epochs. The type II-R profile of 2 March 2009 evolved into a type III-R on 3 March 2009. Another incident of a rapid variation in profile shapes was observed during 29 to 31 March 2009. Three different types of Hα profiles, namely IV-R, II-R, and III-R, were observed on these consecutive nights. The flip-over from type II to type III profiles, i.e the change in strength of blue- and red-shifted emission peaks in a double-peak profile, was also reported by Vieira et al. (2003) in PDS 018 and PDS 024, but on longer timescales that were separated by months to year respectively. We also observed two prominent incidents of infall and outflow in the Hα profiles on 28 to 29 December, 2008 and 17 to 20 January, 2008 respectively. The infall event was seen in the $H\beta$ profiles as well (Fig. 4.11). A few photospheric metallic lines in these epochs (separated by nearly two weeks, Figs. 4.1 and 4.2) were compared and no variation in those profiles were found, which also indicates that there was no significant variation in the stellar photosphere during the infall and outflow events.
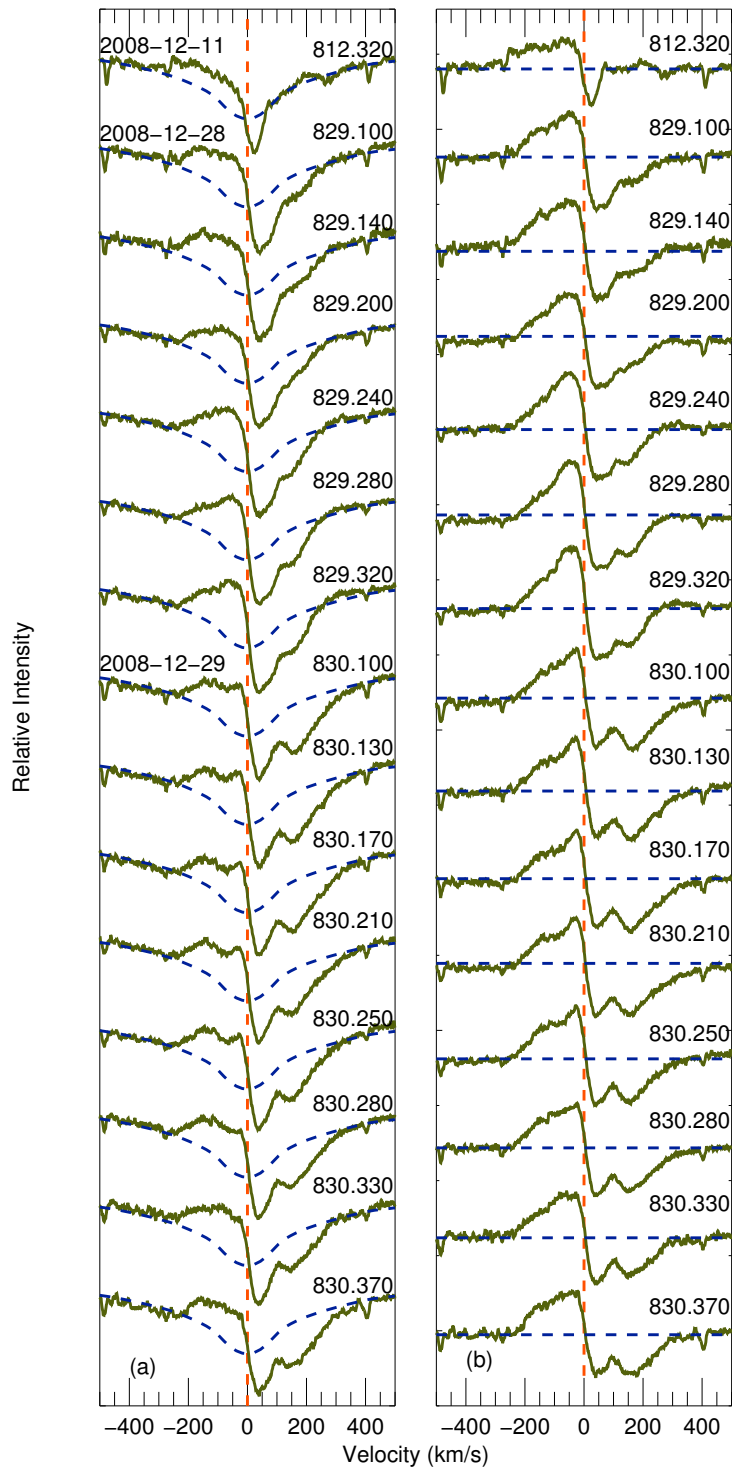
Figure 4.4 **(a)**. Hα line profiles (*green solid lines*) of V351 Ori of a few days in December 2008. Synthetic Hα line profiles (*blue dashed lines*) are overplotted on each spectrum. Modified Julian days are displayed against the respective spectrum. The *vertical red dashed line* represents the rest frame velocity of the star. **(b)**. Residual spectra of Hα line profiles in the same epochs. *Horizontal blue dashed lines* represent the zero absorption levels.
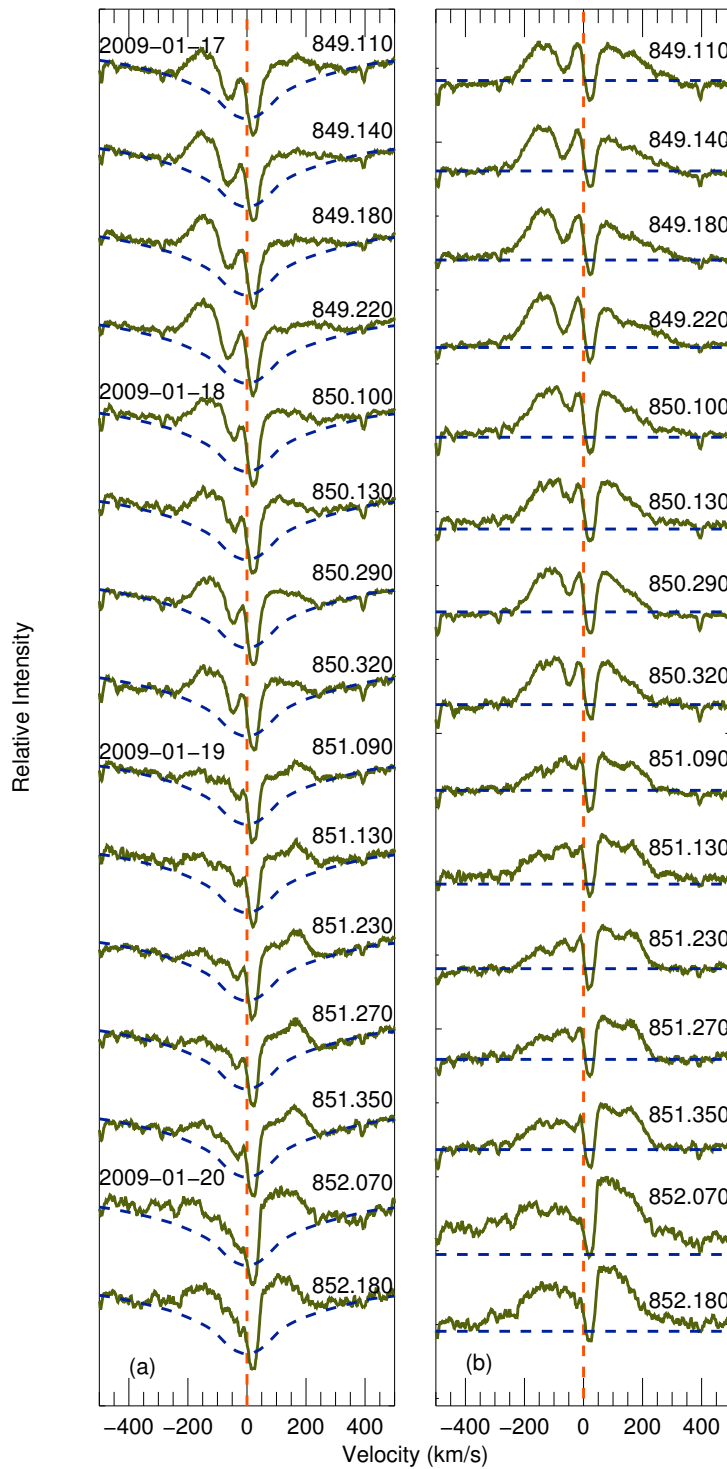
Figure 4.5 **(a)**. Hα line profiles (*green solid lines*) of V351 Ori of a few days in January 2009. Synthetic Hα line profiles (*blue dashed lines*) are overplotted on each spectrum. Modified Julian days are displayed against the respective spectrum. The *vertical red dashed line* represents the rest frame velocity of the star. **(b)**. Residual spectra of Hα line profiles in the same epochs. *Horizontal blue dashed lines* represent the zero absorption levels.
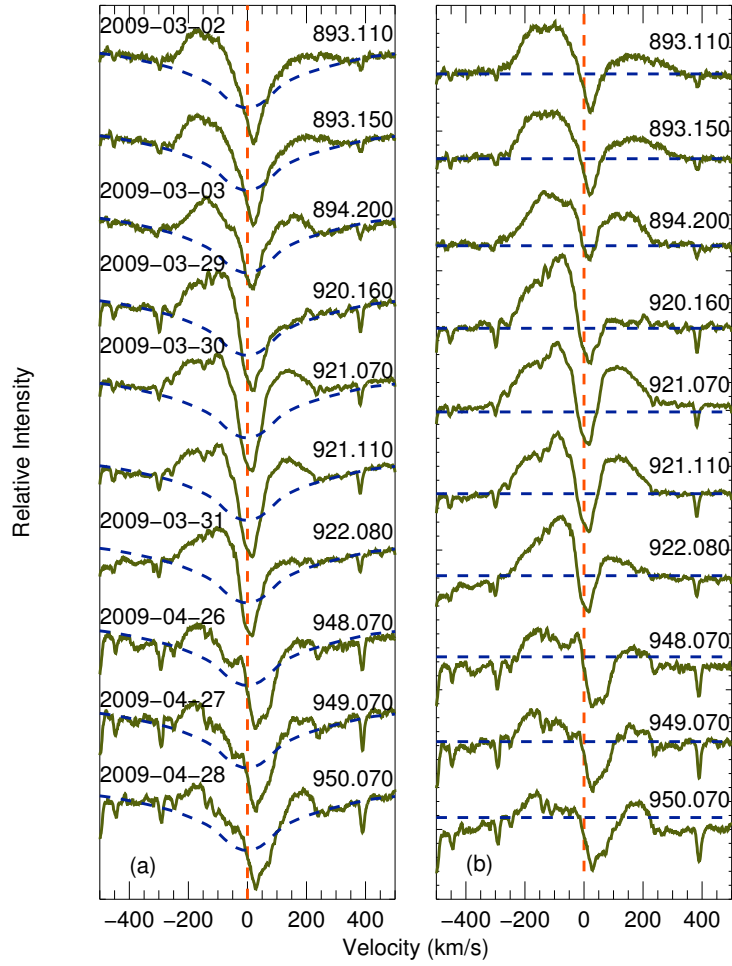
Figure 4.6 (a). Hα line profiles (*green solid lines*) of V351 Ori of some days in March and April 2009. Synthetic Hα line profiles (*blue dashed lines*) are overplotted on each spectrum. Modified Julian days are displayed against the respective spectrum. The *vertical red dashed line* represents the rest frame velocity of the star. **(b)**. Residual spectra of Hα line profiles in the same epochs. *Horizontal blue dashed lines* represent the zero absorption levels.

The mean and temporal variance profiles of Hα line profiles have been created to investigate the characteristics of the variations. We calculated the mean profile by taking the average normalized intensity in each velocity interval of a given profile over all observed profiles. The average normalized Hα line profile of V351 Ori is shown in Fig. 4.7. As suggested by Johns & Basri (1995), we define the temporal variance profile at each velocity interval as

$$\sum_{v} = \frac{\sum_{i=1}^{n}(I_{v,i} - \bar{I}_v)^2}{n-1},$$

where n is the number of spectra, $I_{v,i}$ is normalized intensity at a given velocity (v) in each
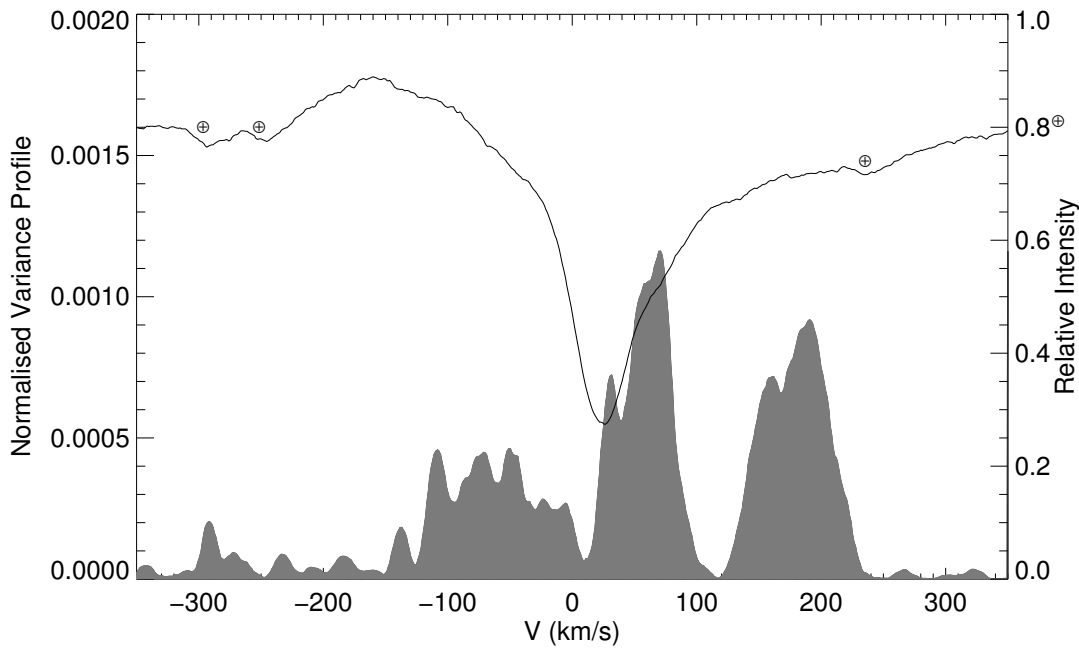
Figure 4.7 Average Hα line profile (solid line) and variance profile (grey shaded area) of V351 Ori obtained using all spectra.

spectrum (i), and $\bar{I}_v$ is mean normalized intensity at a given velocity (v) over all observed spectra. The normalized variance profile (shown as shaded area in Fig. 4.7) can be obtained by dividing the temporal variance profile by the average profile. The normalized variance profile indicates that the behavior of an individual spectrum observed at different epochs deviates substantially from the average profile. Most of the variability in Hα profile is on red side with two clearly distinguished features. There are significant variations on blue side as well, but the profile shows a single peak. A couple of outflow events were observed at different epochs separated by days to months, but they seem to have an approximate average velocity of -100 km s^{-1}. We also observed simultaneous infall and outflow events of different durations at different velocities. It is obvious from Fig. 4.7 that the infall events occurred at two distinctly different velocities of e.g. ∼60 km s^{-1} and ∼150 km s^{-1}. In emission line stars, circumstellar emission first fills the photospheric absorption components and the residual flux emerges as *emission* from the star. If there is strong emission, the reduction of emission flux to cover up the photospheric absorption is not significant. However, for weak emission, where the Hα line profile is dominated by absorption rather than emission, a subtraction of photospheric component is necessary to achieve the true contribution caused by emission. Red-shifted narrow absorption components in Fig. 4.3(a) to Fig. 4.6(a), which indicate infall of matter, are prominently visible beyond the photospheric profiles. Accordingly the subtraction of photospheric profiles are not crucial for comparative studies of these features. However, the broad blue- and red-shifted emission/absorption components at the wings sometimes appeared at the same level as the photospheric profiles. To make sure that we were not looking at the photospheric, but at the circumstellar components, we

subtracted the photospheric spectra from the observed normalized spectra and plotted the profiles in Fig. 4.3(b) to Fig. 4.6(b). The residual profiles also provide a better estimate of maximum velocity reached at the wings of the profiles, which are not contaminated by photospheric components. The maximum velocity of the profile at wings is defined as the full-width-at-zero intensity of the residual spectra. The average and variance profiles using residual spectra have also been created. The average profile in Fig 4.8 is a double-peak
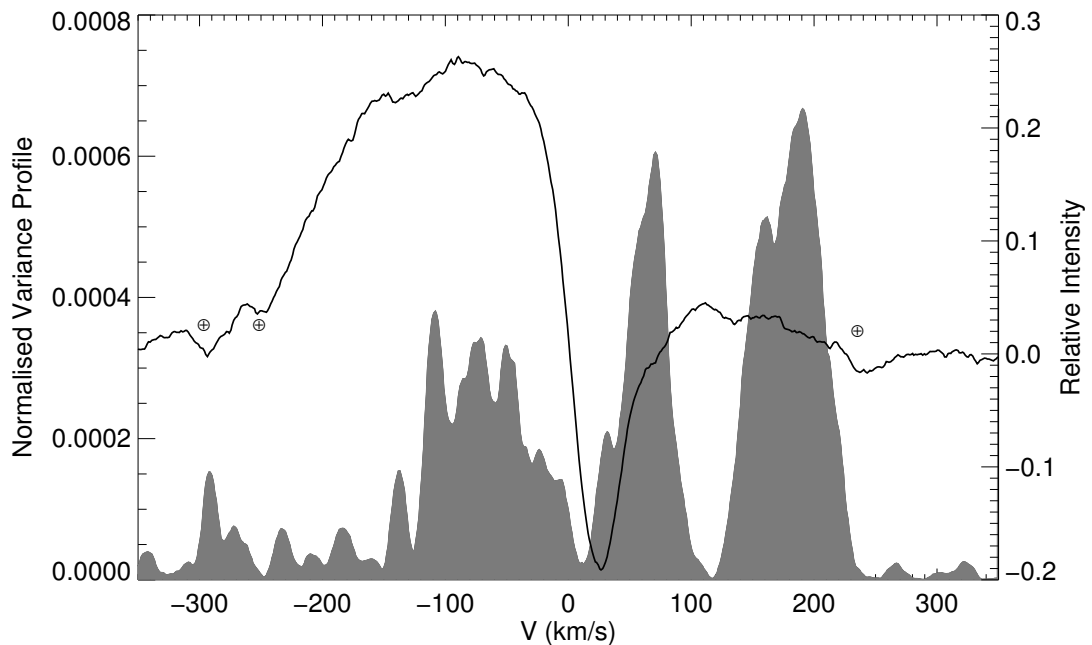
Figure 4.8 Average Hα line profile (solid line) and variance profile (grey shaded area) of V351 Ori obtained using all residual spectra.

profile with a strong blue to red asymmetry, i.e. III-R type, which is different from its counter part in Fig 4.7. The red- shifted absorption near the center is similar to that of Fig 4.7 and there is no change in the variance profiles in Figs 4.7 and 4.8. In Fig. 4.8, the two peaks of the red-shifted variance profiles do not coincide with red-shifted emission peak of average profile of the residual spectra, which supports the presence of emission in most epochs. Double peak profiles are supposed to form in stellar or disk winds contrary to inverse P Cygni profiles, which originate in the infall of materials. We shall discuss below the effects of accretion, winds, etc. on the profile shapes. Significant changes in the average profiles in Figs. 4.7 and 4.8 show that photospheric profile subtraction is necessary at least for weak Hα emission line stars.

4.3.5   Profile Variations on 27 and 30 October, 2008

We observed a double-peak profile, e.g. a type III-R profile, on 27 October 2008 with moderate blue-shifted and weak red-shifted emission components just above the photospheric spectra (Fig. 4.3(a)). The blue-shifted emission component did not change much, but the red-shifted component gained strength and became comparable to its blue-shifted counterpart, i.e. there were nearly symmetric broad emission components on both sides of the central minima, and thus the profile shape evolved into a type II-R on 30 October. The maximum average velocity of the profile was $\sim$ –350 km s^{-1} and $\sim$250 km s^{-1} on 27 October, and $\sim$ –300 km s^{-1} and $\sim$280 km s^{-1} on 30 October at the blue and red wings respectively. We observed simultaneous inflow and outflow events on 27 October. The central broad asymmetric absorption feature ($\sim$40 km s^{-1}) on 27 October was extended more towards the red region. It consisted of two barely resolved components with centers at $\sim$6 km s^{-1} and $\sim$50 km s^{-1}. This broad absorption might be a combination of two absorptions of nearly similar depths because of both the disk and the infall of the circumstellar material. The width of the central absorption was reduced on 30 October and seemed to represent a single absorption component at $\sim$9 km s^{-1}, which was nearly symmetric with the rest frame velocity of the star. We also observed a blue-shifted absorption component on 27 October superposed on the blue-shifted emission component, which is considered as a signature of the outflow. The full width at half maxi ma (FWHM) of the outflow increased with time, but its depth decreased (Table. 4.2).

4.3.6   Profile Variations on 11, 28 and 29 December, 2008

The Hα line profile on 11 December 2008 was of an inverse P Cygni type with a narrow absorption centered at $\sim$30 km s^{-1} (Fig. 4.4). It was one of the few profiles where the red component almost matched the photospheric component. During 28 December and 29 December 2008 the Hα line profiles were also of the inverse P Cygni type. We observed the emergence of an infall event on 28 December and followed its evolution for several hours and until the next night. The depth of the RAC was less than the depth of the central absorption component, which became red-shifted and wider compared to its counter part on 11 December. The nightly variations of the maximum velocity of the blue wings were between –250 to –300 km s^{-1}, and that of the red absorption wings was 300 km s^{-1} and it did not vary much throughout the night. On 29 December 2008 we observed both prominent infall and weak outflow events simultaneously (Fig. 4.4(a) MHJD 830.100 to 830.280). The RAC that emerged on 28 December became deeper and its center was separated from the central absorption component, as a result of which the width of the central absorption component reduced (Fig. 4.9). The maximum velocity at the blue wings did not change, but the average maximum velocity at the red wings shifted to $\sim$380 km s^{-1} on 29 December. The depth of the RAC varied throughout the observations on 28 and 29 December. We show the
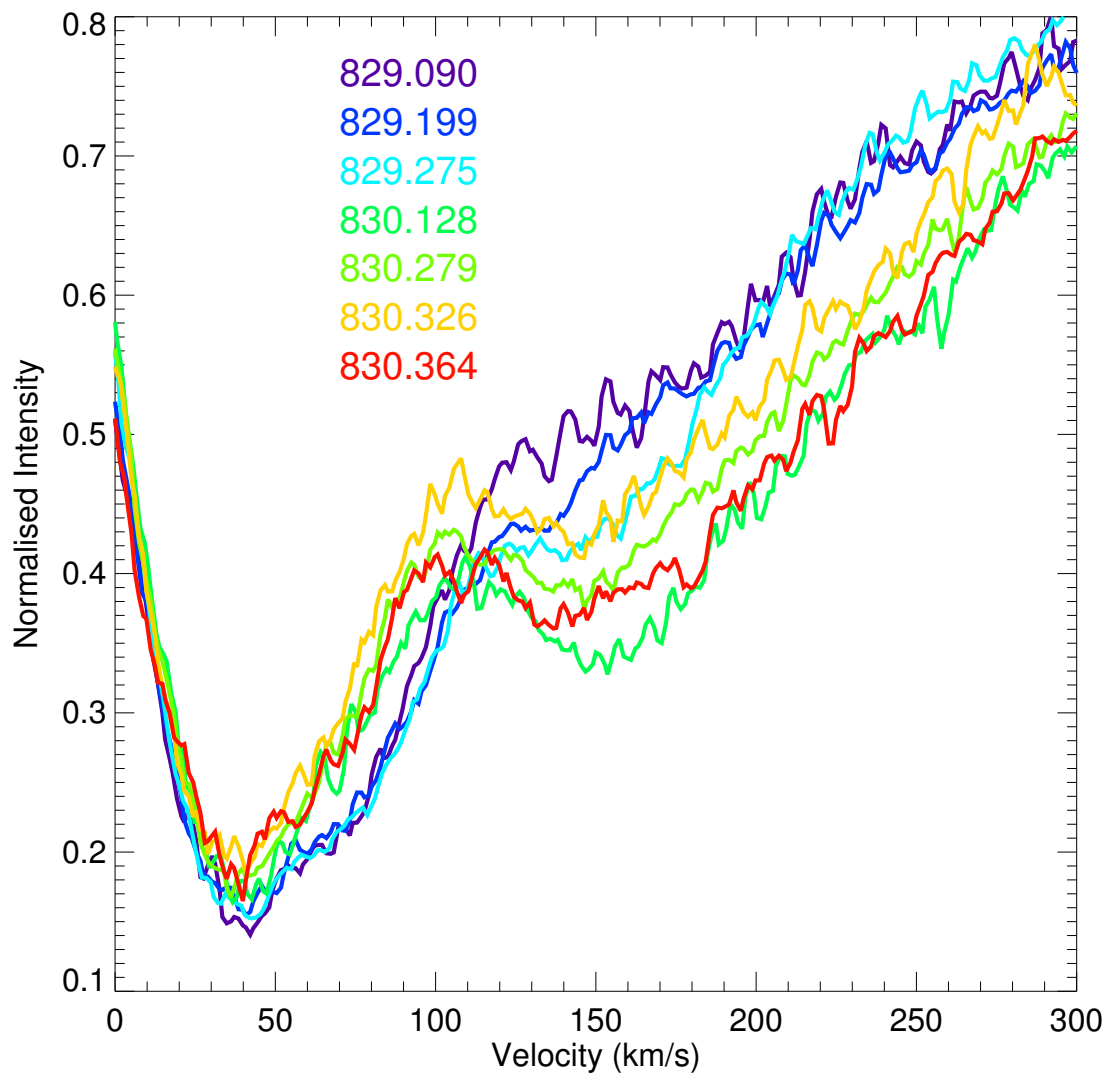
Figure 4.9 Selected Hα emission line profiles on 28 and 29 December 2008 in the rest frame velocity of V351 Ori are overplotted. MHJD of the respective profiles are displayed using the same colours as of the profiles.

emergence and evolution of the RAC in Fig. 4.9. The velocity of the RAC was decelerated within a few hours from its starting point and then became constant at MHJD 830.21, where it remained until the end of the observation on 29 December (Table. 4.2). All observed line profiles of 28 and 29 December showed a blue-shifted emission component whose strength increased after MHJD 829.1. We detected the outflow on top of the blue-shifted emission at MJHD 830.100 and could identify it clearly before MHJD 830.330. It gradually moved towards the central absorption features so the probable reason for its non-detection after MHJD 830.330 might be because the BAC came in the same line of sight of the central absorption.

4.3.7 Profile Variations on 17 to 20 January, 2009

The Hα emission line profiles observed during 17 to 20 January 2009 are mostly dominated by both blue- and red-shifted emission components, i.e. mostly Type II and Type III profiles (Fig. 4.5). The strength of both emission components varied during our observation, e.g. one of the component was always weaker compared to the other component and thus the shapes of the profiles also changed from one type to another. The average maximum velocities at the wings were $\sim$ –250 km s^{-1} and $\sim$250 km s^{-1} in the blue and red sides respectively. We also detected a strong outflow, which was clearly detectable from 17 to 19 January. The central narrow absorption component at $\sim$20 km s^{-1} remained constant throughout the observations. We display the time evolution of the outflow in Fig. 4.10. The
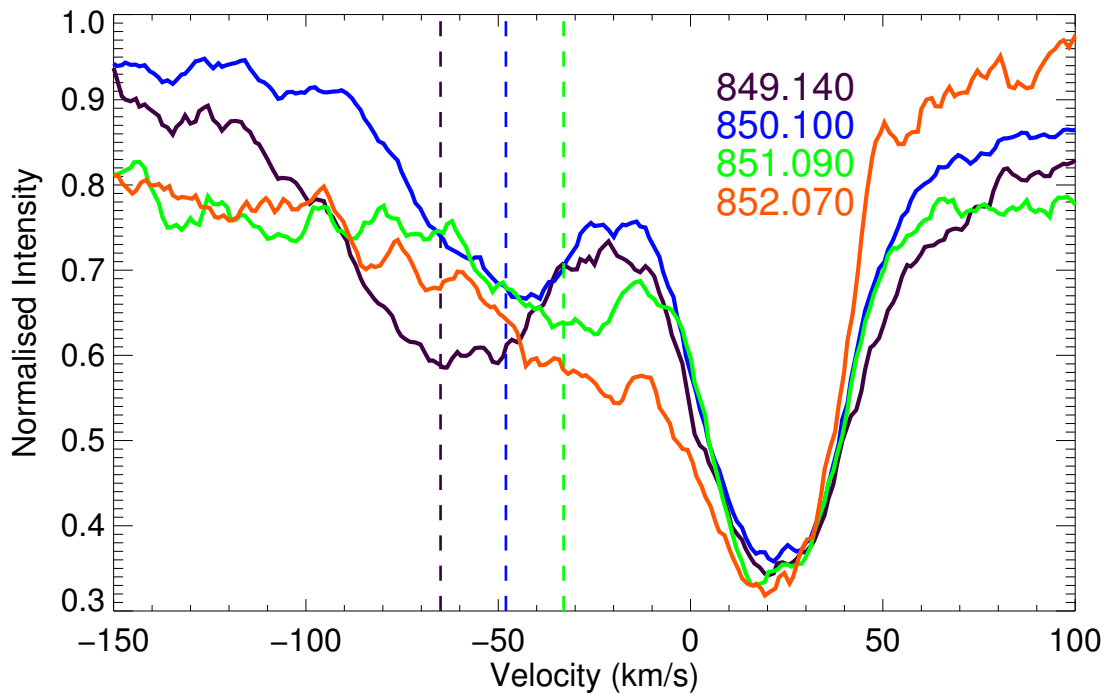
Figure 4.10 Selected Hα emission line profiles on 17 to 20 January 2009 in the rest frame velocity of V351 Ori are overplotted. MHJD of the respective profiles are displayed using the same colours as of the profiles. Vertical dashed lines of different colours represent the centers of the BACs estimated by eye on the respective MHJDs. Red-shifted emission increased on MHJD 852.070 after the apparent disappearance of the outflow event.

outflow gradually became wider as it continuously moved towards the central absorption. It is also worth to mention that the width of the central absorption was at its minimum among our observed spectra. The non-detection of the outflow on 20 January at MHJD 852.070 was most probably caused by the superposition of its line of sight with the central absorption. As a result, the central absorption became wider and asymmetric, e.g. it became elongated

toward blue side and the red-shifted emission reached its maximum strength compared to the other spectra observed during 17 to 19 January, 2009.

4.3.8 Profile Variations in March and April, 2009

Most of the profiles we observed on several days in March and April were double-peaked profiles (Fig. 4.6(a)). On 2 and 3 March 2009, there was a change in the slope of the blue-shifted emission. The red-shifted emission gradually gained strength and the profile evolved from type III-R to type II-R. The average maximum velocity at the blue wing was ~ -250 km s^{-1} and ~ 300 km s^{-1} at the red wing. We did not find any red-shifted emission on 29 March 2009 (MHJD 920.160). The profile showed a blue-shifted emission and the central absorption component. On the next day, we observed a strong red-shifted emission comparable to the blue one, and thus the profile was changed into a type II-R. The red-shifted emission was again considerably reduced on 31 March and we observed a type III-R profile. We detected a blue-shifted absorption component at ~ 71 km s^{-1} on 26 April 2009. The absorption component shifted towards the deep minima on 27 April. There was no signature of outflow in the spectra on 28 April. The red-shifted emission became gradually stronger from 26 to 28 April and became comparable to the blue-shifted emission. These changes are similar to those observed on 28 and 29 December 2008 (Fig. 4.4), but the central absorption features were different, e.g. in April 2009 the central absorption component was board and asymmetric and extended towards the red region compared to the narrow and nearly symmetric central absorption in December 2008.

4.3.9 Line Profiles of $H\beta$, $NaD1$, and $NaD2$

We obtained simultaneous spectra containing the $H\beta$, $NaD1$, and $NaD2$ profiles along with Hα emission line profiles. Due to the poor signal-to-noise ratio, we could not analyze the individual $H\beta$ profiles. Instead, we plot the nightly average profiles of $H\beta$ in the rest frame velocity of V351 Ori and overplot the synthetic spectra in Fig. 4.11(a). The shape of the $H\beta$ profiles also showed variations over the timescales of month. We did not find any emission components in the $H\beta$ profiles within the noise level of our observed spectra. However, the prominent infall event occurred during 28 and 29 December, can be easily seen also in the $H\beta$ line profiles. The $NaD1$ and $NaD2$ profiles displayed in Fig. 4.11(b) consist of a broad and a narrow absorption component. We did not find any elongated absorption at the wings in the broad line profiles. We measured the velocity of the narrow component and found that it was showing an almost constant velocity of $\sim +22$ km s^{-1}, i.e. red-shifted by ~ 11 km s^{-1}, compared to the star.
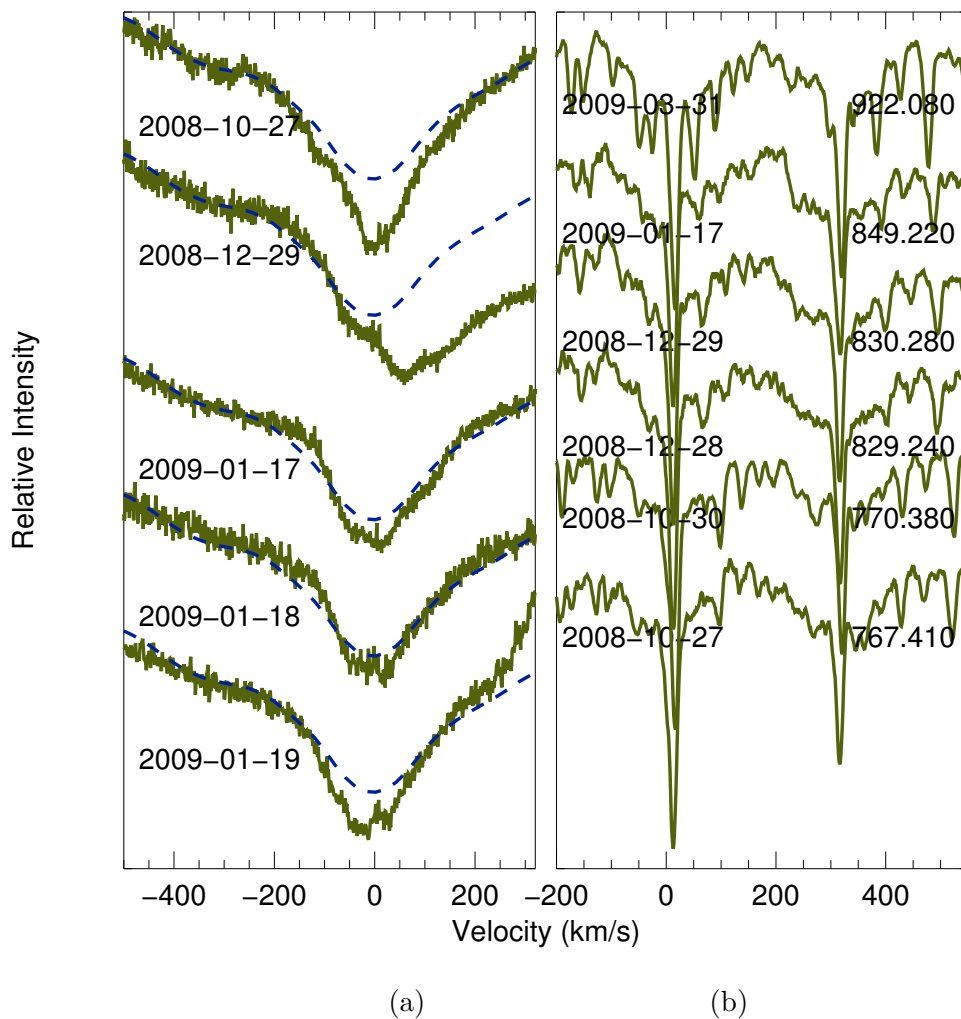
Figure 4.11 **(a)** Nightly average $H\beta$ profiles of V351 Ori on several days. **(b)** Sample $NaD1$ and $NaD2$ profiles of V351 Ori on a few epochs. Velocities are in the rest frame of V351 Ori.

4.4 Discussion

HAeBe stars show photometric variabilities on timescales of days to years. van den Ancker et al. (1996) analyzed the long-term optical photometric behavior of V351 Ori and found that the star showed a large variation of >2 mag before 1985. van den Ancker et al. also reported that the visual magnitude of V351 Ori varied by 0.16 mag between 1985 to 1990, i.e. over timescale of years. During 1990 to 1995, the visual magnitude of the star became almost constant without any significant variation. Balona et al. (2002) obtained the optical magnitudes (e.g. V~8.92, $B-V$ ~0.37, $V-R$ ~0.22 and $V-I$ ~0.46 mag) over timescales of minutes to weeks and did not find any significant variation within 0.05 mag. We obtained optical $BVRI$ photometry of the star on 11 November, 2009 and obtained the magnitudes V~8.89, $B-V$ ~0.38, $V-R$ ~0.19, and $V-I$ ~0.41 mag, which indicates that there are no significant changes in the long-term photometric behavior of V351 Ori. However, it is

also noteworthy that our photometric observation did not coincide with the spectroscopic observation. Unlike the variations in visual magnitudes, which reflect the variable stellar photosphere, near infrared (NIR) variability can account for changes in both the stellar photosphere and the circumstellar environments. Balona et al. (2002) compared the NIR magnitudes of V351 Ori and found that $H - K$ excess of V351 Ori (which serves as a proxy for the inner disk materials) decreased continuously over the period from 1982 to 2002. van den Ancker et al. (1996) and Balona et al. (2002) suggested that the systematic NIR variability of V351 Ori is caused by the clearing of dust around the star, which indicates a variable circumstellar environment around V351 Ori.

Our high-resolution spectroscopic observations revealed the variable circumstellar environment and presences of TACs in the weak Hα emission line of the Herbig Ae star V351 Ori. As mentioned earlier, TACs in higher Balmer lines and in a few metallic lines have been detected in Herbig Ae stars such as BF Orionis, SV Cephei, WW Vulpeculae, XY Persei, and UX Orionis (Mora et al., 2002, 2004). All these Herbig Ae stars show prominent Hα emission profiles with equivalent widths ranging from -2.3 Å (for UX Ori) to -30.0 Å (for WW Vul) (Manoj et al., 2006). These stars also show optical photometric and polarimetric variabilities over timescales of months (Oudmaijer et al., 2001). XY Per, UX Ori, BF Ori, and WW Vul also show NIR variability over timescales of months (Eiroa et al., 2001). The characteristics of V351 Ori do not match the trend of the Herbig Ae stars mentioned above, because V351 Ori shows nearly constant optical magnitudes over years and a low Hα emission equivalent width (≤1 Å). Moreover, V351 Ori is also comparatively older (∼6.5 Myr) than the mentioned group of Herbig Ae stars with ages ranging from 2.5 to 5.2 Myr (Manoj et al., 2006; Montesinos et al., 2009). These differences make V351 Ori an interesting target to study the interaction of intermediate PMS stars (contracting towards the main sequence) with their circumstellar environment.

V351 Ori is known as an isolated HAeBe star without any associated nebulosity in its immediate vicinity. However, (Hernández et al., 2005) suggested its association with the Ori OB1bc region located at a distance of 400 to 450 pc. The estimated ages of V351 Ori available in the literature vary from 1 to 6.5 Myr (van den Ancker et al., 1996; Ripepi et al., 2003). The main sources of uncertainty to estimate the age from the HR diagram is the distance to the star. The lower limit of the distance is ∼210 pc (van Leeuwen, 2007) and the upper limit is ∼450 pc, which comes from the assumption of its association with the *Ori OB1bc* region (Hernández et al., 2005). Ripepi et al. (2003) analyzed the pulsating behavior of V351 Ori and suggested an intermediate value for the distance between the upper and lower limit, which leads to an estimate of the age of ∼6.5 Myr. The Hα emission from HAeBes, which is a proxy for active accretion, are found to decrease significantly beyond 3 Myr e.g. Manoj et al. (2006). There are some HAeBe stars older than ∼6 Myr with significant Hα emission (Manoj et al., 2006; Montesinos et al., 2009). However, the proposed age of V351 Ori i.e. 6.5 Myr seems to be consistent with the common trend

of weak Hα emission from stars with ages > 3 Myr. We also consider that the mass of V351 Ori is 2 M$_\odot$ as estimated by Ripepi et al. (2003).

4.4.1   Kinematics of Transient Absorption Components (TACs)

Blue-shifted absorption components (BACs) and red-shifted absorption components (RACs) detected in Hα emission line profiles of V351 Ori showed variation in the velocity centers, depths and widths of the profiles. We show the evolution of a RAC and BAC in Figs. 4.9 and 4.10 respectively. We tried to reproduce the observed Hα profiles by fitting a multiple number of Gaussian components but we also noticed that the fitted Gaussians were not unique. When we tried to fit some profiles, e.g. the observed profiles of 29 to 31 March, 2009, we found that we got a good fit when we fitted two separate Gaussians to the blue-shifted and red-shifted emission components rather than a single Gaussian for the whole emission component. The fitting of these complicated and variable profiles for all observed spectra in a consistent way demands a complete knowledge of the geometry of line-forming regions and their distribution with respect to the central star, which is beyond the scope of this work. Accordingly we measured the velocity centers and depths of the TACs' profiles by fitting Gaussian profiles to the individual TACs of the normalized spectra over the baseline of unity (obtained by the normalization of the observed spectra by synthetic photospheric spectra). In this way, we estimated the velocity centers and depths of the individual component confidently, however, we could not estimate the FWHM of the individual TACs, which requires the fitting of the entire profile. As a result we discuss the kinematics of the observed TACs and not the physical conditions of the infalling and outgoing materials, because that partly depends on the values of the FWHM as well. It is also worth to mention that the detection and analysis of TACs in other Balmer lines such as $H\beta$, $H\gamma$ etc. provides additional information. Because of the poor signal-to-noise ratio at $H\beta$ we could not detect the TACs as observed in the Hα profiles. However, good temporal coverage of the spectroscopic observations helped to make an unambiguous detection of the TACs in the Hα line profiles, and thus the kinematics of the TACs estimated from Hα profiles only are also highly reliable. We list the velocity centers and depths of the TACs from the normalized continuum level in Table 4.2. We plot the time evolution of the velocities of TACs in Fig. 4.12. All detected TACs in the Hα line profiles showed deceleration of the gas at various rates. The rate of deceleration of the outflow event on 27 October 2008 was ∼2 m s^{-2}, for the infall event on 29 December 2008 it was ∼1.7 m s^{-2}, for outflow event it was ∼2.2 m s^{-2}, and for the outflow event during the 17 to 19 January 2009 it was fraction of m s^{-2}. Neither the magnetospheric accretion model nor the wind model provide any detailed explanation about the deceleration of the TACs. A detailed calculation of a time-dependent model considering accretion and wind models and including the observed results is very important to understand the variable star-disk interactions. Broad red-shifted absorption wings at high velocities are supposed to originate from the free fall

Table 4.2 Transient Absorption Components appeared in the Hα line profiles of V351 Ori

Date yy-mm-dd	HJD (-2,454,000)	Cent. km s^{-1}	Depth	Cent. km s^{-1}	Depth
2008-10-27	767.32	-117.36	0.76	...	...
2008-10-27	767.36	-117.83	0.81	...	...
2008-10-27	767.41	-107.07	0.84	...	...
2008-12-29	830.10	157.50	0.34	-72.90	0.78
2008-12-29	830.13	150.07	0.34	-72.43	0.77
2008-12-29	830.17	148.40	0.33	-72.92	0.75
2008-12-29	830.21	139.74	0.37	-73.03	0.78
2008-12-29	830.25	140.74	0.38	-65.49	0.78
2008-12-29	830.28	138.41	0.39	...	...
2008-12-29	830.33	138.94	0.42	...	...
2009-01-17	849.11	-59.20	0.60	...	...
2009-01-17	849.14	-59.24	0.61	...	...
2009-01-17	849.18	-58.20	0.64	...	...
2009-01-17	849.22	-59.82	0.62	...	...
2009-01-18	850.10	-44.66	0.68	...	...
2009-01-18	850.13	-44.30	0.65	...	...
2009-01-18	850.29	-44.18	0.63	...	...
2009-01-18	850.32	-44.30	0.62	...	...
2009-01-19	851.09	-33.94	0.63	...	...
2009-01-19	851.13	-32.02	0.65	...	...
2009-01-19	851.23	-35.34	0.61	...	...
2009-01-19	851.27	-34.44	0.60	...	...
2009-01-19	851.35	-31.84	0.59	-103.79	0.73
2009-04-26	948.07	-55.88	0.61	...	...

of the surrounding material onto the star. The cool outflowing gas is supposed to originate farther away from the star than the accretion-dominated emission, but still within about $\sim$10 $R_\odot$(Edwards et al., 2003). We found that the average maximum velocity of the red-shifted emission wings was $\sim$250 to $\sim$300 km s^{-1}. We detected an enhanced red-shifted absorption wing extending up to $\sim$380 km s^{-1}on 29 December, 2009. Assuming the free-fall velocity condition, we estimate the extent of the region involved in the accretion processes as $\sim$5 $R_\odot$, which indicates that the changes are taking place within a radius of $\sim$0.02 AU. Monnier & Millan-Gabet (2002) studied the dust sublimation radius of the PMS stars with a stellar radiation field. They discussed the relation between the size of the inner dusty disks and the luminosity of the central stars in the context of different disk models including the paradigm of both optically thick and thin inner disks. Considering the uncertainties such as the distance and thus the luminosity, and the model for optically thin/thick disks, the typical dust sublimation radius of V351 Ori would be in the range of $\sim$ 0.07 to .2 AU. A comparison between the region of the gas accretion and the dust sublimation radius hint towards the presence of gaseous material in the inner disk cavity of V351 Ori. Further investigation of the inner disk properties of PMS stars such as V351 Ori will be helpful to understand the disk-dissipation processes and the associated timescales.
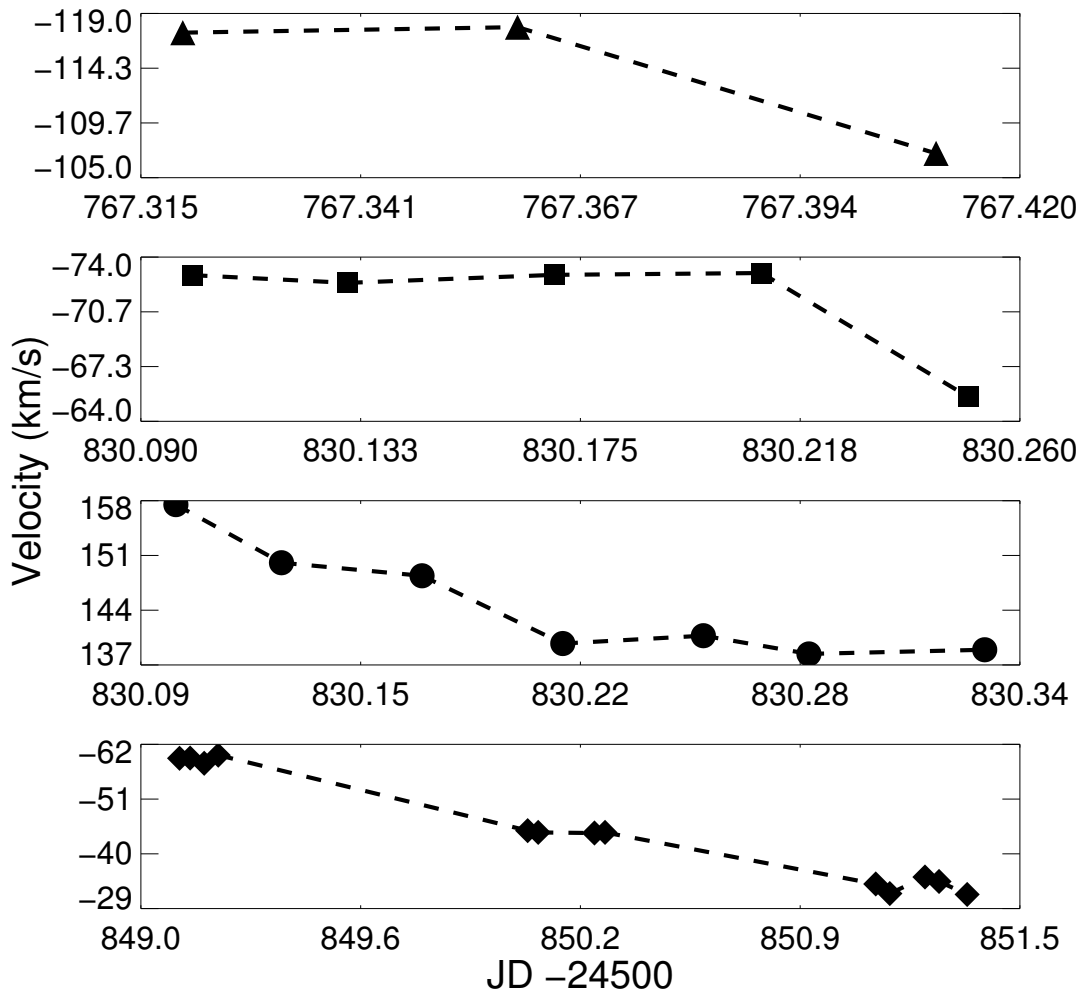
Figure 4.12 Time evolution of the TACs as they appeared in the Hα line profiles. *Triangles* represent the outflow event on 27 October 2008, *squares* and *circles* represent the outflow and infall events respectively on 29 December 2008, and *diamonds* represent the outflow event during 17 to 19 January 2009.

4.4.2   Dust Mass Estimates using IRAS Fluxes

The detection of red-shifted absorption wings that extend beyond 300 km s^{-1} supports a scenario of the accretion of surrounding materials onto the star. However, as V351 Ori also shows weak Hα emission, so it will be interesting to investigate whether the left-over gas in the circumstellar environment of the star is sufficient to continue the accretion. We estimate the dust mass and thus the gas mass in the circumstellar disk of V351 Ori using the Infrared Astronomical Satellite (IRAS) fluxes.

Dust grains present in the circumstellar environment absorb and scatter varying fractions

of the incident photons ($\lambda \leq 1\mu$m) and re-emit part of the absorbed energy in the infrared band. Far infrared emission properties of the dust grains can be used to derive estimates on the amount of dust of the disks of PMS stars, assuming the emission at these wavelengths is optically thin. As suggested by Hildebrand (1983), the disk dust mass M_d can be computed using the relation

$$M_d = \frac{4\pi}{3} \frac{a\,\rho_d}{Q_\nu(T_d, a)} \frac{d^2 F_\nu(T_d)}{\pi B_\nu(T_d)},$$

where a, ρ_d and d are the grain radius, specific grain mass density, and distance to the source, respectively. F_ν, $Q_\nu(T_d, a)$, and $B_\nu(T_d)$ are the observed flux density, grain emissivity and the Planck function of temperature T_d at frequency ν. van den Ancker et al. (1996) analyzed the Spectral Energy Distribution (SED) of V351 Ori and estimated that the dust temperature corresponds to the far infrared (FIR) IRAS fluxes as 80 K. The FIR SED of V351 Ori peaks between 25 and 60 μm and drops gradually between 60 and 100 μm, which suggests that most of the emission arises beyond 25 μm. In that case the calculation of dust grain temperature using 60 and 100 μm flux densities (G. Helou & D. W. Walker, 1988) would be a better estimate. Using the following relation, $T_d = 49 \left(\frac{S_{60}}{S_{100}} \right)^{0.4}$ (Young et al., 1989), we estimated the dust grain temperature as 53 K. We adopted $\rho_d = 3$ g cm^{-3}, $a = 0.1\,\mu$m and $\frac{4a\,\rho_d}{3Q_\nu} = 0.024$ and 0.04 g cm^{-2} at 60 and 100 μm respectively (Hildebrand, 1983). The estimated dust masses at 60 and 100 μm are 9.5×10^{-5} and 9.2×10^{-5} $M_\odot$ respectively at an adopted distance of 450 pc and 2.07×10^{-5}, and 2.01×10^{-5} $M_\odot$ at 210 pc. Assuming a gas-to-dust ratio of 100, the estimated disk mass (dust+gas) would be in the range of 0.002 to 0.009 $M_\odot$. The estimated values of the disk mass of V351 Ori are lower compared to the disk mass of actively accreting Herbig Ae type stars such as AB Aur (0.01 $M_\odot$), HD 163296 (0.028 $M_\odot$) derived from millimeter observations (Mannings & Sargent, 1997). This is consistent with the relatively evolved circumstellar environment of V351 Ori.

4.4.3   Accretion and Wind Models

The Hα emission line serves as one of the most important empirical signatures of accretion of the circumstellar material onto the central PMS stars. Magnetospheric accretion models are quite successful in explaining the observed spectral characteristics such as broad asymmetric line profiles etc. of accreting classical T Tauri stars (CTTS) i.e. the lower mass counterparts of HAeBe (Hartmann et al., 1994; Muzerolle et al., 1998a, 2001). According to magnetospheric accretion models, the stellar magnetic field disrupts the circumstellar disk at several stellar radii and the accreting material falls onto the stellar surface along the magnetic field lines (Koenigl, 1991). The results of magnetospheric accretion models suggest that the hydrogen emission lines form in the infall zone, so that the blue-shifted asymmetric emission-line profiles arise due to partial obscuration of the flow by the inner

part of the accretion disk and the red-shifted absorption profiles result from infalling material at near free-fall velocities onto the stellar surface (Muzerolle et al., 1998a). Muzerolle et al. (2004a) also demonstrated the magnetically channelled disk accretion in the Herbig Ae star UX Ori and partly reproduced the double-peak Hα profile of UX Ori. Several studies e.g. Alencar et al. (2005); Kurosawa et al. (2006) found that disk wind also play an important role in the formation of double-peak profiles in CTTS.

V351 Ori showed a variety of Hα line profiles throughout our observation. The shape of the profiles contains information about the geometrical orientation and physical processes involved in the interaction of the star with its circumstellar environment. The common trends in all spectra are the slightly red-shifted central absorption and the elongated blue-shifted emission components. The width of the central absorption changed within a day. Though the strength of the blue-shifted emission component varied with time, but there was no significant variation in the maximum velocity at the wings. On the contrary, the red-shifted component showed drastic variations in shape, strength, and velocity. The strength of the red-shifted emission, if present, was less than the blue-shifted emission, which can be attributed to the selective absorption of the red-shifted flux due to the asymmetric distribution of the star-disk system with respect to our line of sight.

Kurosawa et al. (2006) investigated the formation of Hα emission line profiles around CTTS combining the magnetospheric accretion and disk-wind models (hybrid model). Though the Hα emission line profiles are calculated with typical parameters of CTTS, but it has also been suggested that the model can be used for other PMS stars such as HAeBe stars and for Brown dwarfs (BDs). In order to understand the relative importance of the accretion and wind on the formation of the line profile Kurosawa et al. calculated the Hα line profiles for three cases e.g. the magnetospheric accretion, the disk wind, and a combination of magnetospheric accretion and disk wind models. With the use of this hybrid model Kurosawa et al. were able to reproduce the variety of the Hα emission line profiles reported by Reipurth et al. (1996). Kurosawa et al. also discussed the degeneracy in the line profiles which mostly emerged from the disk wind and the hybrid model. For example, the double peak Hα emission line profiles can be reproduced using the disk-wind model only. It is somewhat difficult to distinguish the contribution of magnetospheric accretion and disk winds in the emission line profiles . Alencar et al. (2005) reported the line profile variability of CTTS RW Aur and found significant variations in the intensity of the blue- and red-shifted emission components similar to V351 Ori. Alencar et al. tried to reproduce the double-peaked Hα emission line profiles with the magnetospheric accretion model and the disk wind model. The Hα, Hα, and $NaD1$ profiles calculated using the disk wind models provided a better fit to the observed spectra. These studies reveal the importance of disk wind in the emission line profiles of the PMS stars. While the magnetospheric accretion model produces double-peak profile under certain conditions such as accretion rates etc., the wind model produces double-peak profiles in usual conditions (e.g. Alencar et al. (2005);

Kurosawa et al. (2006)). So it is possible that the disk wind contributes significantly in the Hα emission of V351 Ori, which showed a double-peak profile most of the time during our observation. However, we did not detect [O I] λ6300 Å emission in our observed spectra, which according to several authors forms in the disk wind (Hartigan et al., 1995). However, Acke et al. (2005) proposed that [O I] λ6300 Å emission arises in the surface layers of the protoplanetary disks surrounding HAeBe stars due to the the photodissociation of OH molecules. The maximum equivalent width of the Hα emission in our observed spectra is < 1 Å, which is less than the typical minimum equivalent width of the Hα emission, of ∼4 Å of the observed samples of HAeBe stars studied by Acke et al. (2005). Considering the discrepancy regrading a thermal or non-thermal origin of the [O I] λ6300 Å emission and the low Hα emission, the absence of the line may not contradict with the presence of a disk wind. However, considering the rapid variation in the Hα emission on timescale of a day, which can be attribute to the variation of wind acceleration rate (Kurosawa et al., 2006), we propose that the disk wind may be responsible for most of the Hα emission of V351 Ori. However, the degeneracy of accretion and disk-wind models cannot be explored completely with our observed spectra.

We try to interpret the behavior of V351 Ori in the context of hybrid model, i.e. by considering the effect of magnetospheric accretion as well as the disk-wind. The central absorption that was present in most of the spectra seemed to arise because of the geometrical configuration of the star-disk system which is viewed nearly edge-on. The changes in the shapes of the central absorption component, for most of the epochs, seemed to arise from the superposition of infall or outflow events in the same line of sight. On 27 October 2008, the Hα emission line profile may have been powered by a disk wind with the simultaneous presence of infall and outflow. The infall was quite prominent and it obscured the red-shifted emission component. Before 30 October 2008, the infall event ended and the central absorption returned to the normal shape with a nearly symmetric double-peak profile. On 28 and 29 December 2008, the Hα emission line profiles were dominated by the infall event. During 17 to 20 January 2009, the Hα emission line profiles were dominated by the disk wind but the blue-shifted emission was partially obscured by the prominent outflow event. The Hα emission line profiles observed during March and April 2009 also probably dominated by the disk wind. The Hα emission from V351 Ori seems to originate in disk wind and at the same time sporadic infall of matter moderated by a magnetic field, and the outflow of cool gas occurs quite frequently.

4.5 Conclusion

Spectral analysis of 45 high-resolution spectra reveals that the line profile variability of V351 Ori is ubiquitous. The line profile variations are caused by changes in disk wind, wind acceleration, rate of accretion, and outflow of cool gaseous material. These signatures

support the complex and dynamical interaction of the circumstellar material with V351 Ori. The circumstellar environment of the Herbig Ae star V351 Ori most probably consists of an inner cavity with gaseous material, a dusty disk and disk wind. The interaction processes are highly time-dependent from one hour for the changes in TACs to one day and longer timescales of the order of months for the changes in the overall characteristics of the broad Hα profiles. Owing to the extensive time coverage of the observation down to timescales of hours we could follow the time evolution of the individual TACs unambiguously. The long term monitoring of the star at timescales of months confirmed the deviation of the Hα emission line profiles from inverse P Cygni types. Accretion and outflow events are not continuous in nature, and the profiles of the TACs seem to be created by obscuration due to gaseous blobs, which indicate that the circumstellar environment of V351 Ori is inhomogeneous and clumpy in nature. Detectable changes in the TACs showed a deceleration of the order of a fraction to a few m s^{-2}. Variation in the blue- and red-shifted emission components also occurred frequently on the shortest timescale of hours, which suggests the rate of the wind acceleration is also time-dependent. Finally, the presence of emission in the absence of veiling emphasizes the importance of the disk wind in V351 Ori. Models containing dynamic and non-axysymmetric magnetospheric accretion with the disk wind may be able to provide a satisfactory explanation of the complex circumstellar activities of PMS stars.

Summary & Future Perspectives

Chapter 5

Summary & Future Perspectives

5.1 Summary

In this work, we have investigated some aspects of interaction of young massive- and low-mass stars with their environment. Massive stars interact with their parent Giant Molecular Clouds (GMCs) and also affect the large scale structure of the galaxies. Low- and intermediate mass stars strongly interact with their circumstellar environment and affect their ambient interstellar medium up to a few pc, through the energetic outflows known as Herbig-Haro objects. Observational evidences of radiative and mechanical feedbacks of massive stars, (e.g. *Radiation Driven Implosion (RDI)*, *Rocket Effects*, supernova explosion etc.) on their parent GMCs have been studied. As we have discussed in Chapter 1, Bright-Rimmed Clouds (BRCs) and Cometary Globules (CGs) are produced by the effect of RDI on the pre-existing globules in the GMCs. Some of the BRCs and CGs of two well-known and prominent Galactic H II regions, namely IC 1396 and Gum Nebula, were selected for this study. To study the interaction of Pre-Main Sequence (PMS) stars with their circumstellar environment, Herbig Ae star V351 Ori was selected. Low- and intermediate mass stars mainly build up their masses through accretion from their circumstellar disks. Circumstellar disks play an important role to moderate the accretion processes. Accretion rates seem to decrease with the age of the PMS stars. But there is no specific timescale at which accretion generally get stopped for most of the PMS stars. Rather the rate of accretion depends on the available circumstellar material. Low accretion rates of the PMS stars are diagnosed by their weak Hα emission. V351 Ori is a weak Hα emission line star with significant infrared excesses in near infrared wavelengths. An extensive study of its spectroscopic behavior over timescales of hours, days and months has been carried out as part of this work. In this chapter, we briefly summarize the methods and main results of this study.

H II region IC 1396 is associated with Cep OB2 association and contains 11 BRCs which are distributed in a circular pattern around the O type star HD 206267. The northern massive globule SFO 38 has been studied extensively to examine the observational signatures of

triggered star formation. In Chapter 2, we have presented multiwavelength photometric study of SFO 38 from optical *BVRI* to *Spitzer* IRAC and MIPS observations along with optical spectroscopy of the selected objects. A total of 40 Young Stellar Objects (YSOs) (Classes 0/I/II) and 13 YSO candidates are identified based on mid infrared (MIR) color indices and we also confirm Hα emission from 2 YSOs which are not known in the literature. We further identify 4 additional YSOs based on Hα emission and thus we find 44 YSOs in and around SFO 38. We find that Hα emission line YSOs are mostly K–M type stars with an age spread of 1-8 Myr and mass range of 0.3-2.2 $M_\odot$. Some of the YSOs show photometric variation in optical and near infrared (NIR) bands and variable Hα emission in the medium resolution spectra. Mass accretion rates estimated form broad Hα line profiles are of the order of 10^{-8} to 10^{-10} $M_\odot$ yr^{-1}. Mass, luminosity and age of the different components of the protostellar cluster at IRAS 21391+5802, have been estimated by fitting the Spectral Energy Distribution (SED). Continuum subtracted Hα line image of SFO 38 shows asymmetric Hα emission at the bright-rim. Two OB type stars e.g. HD 206267 (O6.5) and HD 206773 (B0V) are proposed as the potential ionizing sources for the globule. We also find that Class II to Class 0/I objects are distributed, in a systematic pattern, from the rim to the core part of the globule respectively. We also identify at least two different axes of elongation of the YSO distribution. The spatial gap between the two different classes of YSOs is consistent with the difference in the arrival time of a shock wave propagating into the globule. The spatio-temporal gradient in the distribution of YSOs along two different axes that are aligned with either of the ionizing stars indicates triggered star formation due to Radiation Driven Implosion.

Galactic H II region, Gum Nebula is associated with two OB associations i.e. Vela OB2 and Tr 10 and contains ∼30 CGs. Signatures of ongoing star formation are found in some of the globules. In Chapter 3, we have discussed the known YSOs and their proper motion measurements, associated with the CGs. Two YSOs, NX Pup and PHa 92, are found to be embedded in their parent CGs i.e. CG 1 and CG 22. We traced back the proper motions of NX Pup and PHa 92 back in time to determine their trajectories. The relative spatial positions of these two YSOs in past, lead us to discard the supernova explosion of the companion of ζ Pup, about 1.5 Myr ago being the cause of the expansion of the system of the CGs. We also compared the relative proper motion of these two YSOs with respect to the O-type star ζ Pup and Vela OB2 association. We argued that this relative velocity can be used as a proxy for the velocity due to the Rocket Effect. We also extended this analysis for the YSOs with proper motion measurements, in at least one component, greater than the given error . Almost null values of the relative proper motions within the error-bar, do not support the value of Rocket Effect velocity of ∼ 40 km/s, and indicate a lower value of the velocity less than 5 km/s. We suggest that the nearly circular distribution of CGs with an average radius of ∼ 70 pc is created due to the photoevaporation by massive stars of the nearest OB associations.

Temporal variation in Hα line profiles of V351 Ori has been presented in Chapter 4. High resolution echelle spectra of V351 Ori spanning over timescales of ∼1 hour to 7 months have been used for this study. Most of the Hα line profiles were asymmetric with the rest frame velocity of the star and significant night to night variations of Hα line profiles were observed. One of the important features of the spectra was the simultaneous presence of infall and outflow processes represented by the red-shifted and blue-shifted components of the spectra. Synthetic photospheric line profiles are calculated using model stellar atmospheres. Synthetic profiles were subtracted from the observed profiles to estimate the total emission from the star which otherwise were suppressed by the circumstellar material. The average Hα emission line profile obtained from subtracted Hα emission line profile is inverse P Cygni type in nature which originates due the infall of the circumstellar material onto the central star. We also detected a number of Transient Absorption Components (TACs) in Hα emission line profiles on several epochs. TACs originate due the infall or outflow of the clumpy circumstellar gaseous material close to the star. We tabulated the velocity of the TACs at different epochs and from this data we estimated the rate of change in velocity of the TACs. Both infalling and outflowing materials detected in our observations are found to be decelerated with a rate of a few to fractions of m s^{-2}. The depth and width of the TACs were also changing with time. The presence of elongated red-shifted components at some epochs supports the episodic nature of accretion. Variable emission and absorption components detected in Hα line profiles show the dynamic nature of interaction between V351 Ori and its circumstellar environment. The Hα non-photospheric profiles of the star most probably originate in the disk wind. Episodic accretion of gaseous material at a slow rate and outflow of clumpy gaseous material are still occurring in V351 Ori at an age of 6.5 Myr. Dynamic magnetospheric accretion and disk wind emerge as the most satisfactory model for interpreting the observed line profile variations of V351 Ori.

5.2 Future Plans

We used various properties of the YSOs in this study to understand their environment . We want to pursue our investigation further in this direction to unserstand the following issues

5.2.1 Disk Evolution of Young Stellar Objects in OB association

It has been found that the mass accretion rates on stars of the Trapezium cluster (Orion nebula) are systematically lower than those of similar stars in the Taurus-Auriga association. The probable reason for this discrepancy can be due to the premature disk evaporation of low mass stars in a rich cluster by the influence of nearby OB association. We are planning

to investigate this environmental effect by a detailed study of the young stellar population in nearby OB associations.

5.2.2   Impact of Triggered Star Formation on Initial Mass Function

It has been found that triggered star formation in BRCs and CGs favored low to intermediate mass star formation. But at the same time low mass stars which are situated closer to the ionizing sources may terminate their pre-main sequence growth with masses lower than the mass that would have reached if disk accretion could have proceeded undisturbed until the final disk consumption. For isolated star formation, i.e less influenced by external environment, the final stellar mass is fixed in the early stages of protostar formation through fragmentation and accretion phenomena regulated by magnetic fields or supersonic turbulence. YSOs build-up most of their masses through accretion from the circumstellar disks at a rate that decreases with stellar ages. However, for young stars in OB association, envelope and especially disk evaporation will eventually abort the star formation process. Low mass objects, therefore, remain less massive in a OB association, resulting in a relative overabundance of low mass stars. If this scenario is true, then there should be a systematic difference between the IMF of isolated star forming regions and young clusters near OB association. Our aim is to find observational evidence of the feedback mechanism that may affect the IMF in different star formation environments.

Resources

Bibliography

Acke, B., van den Ancker, M. E., & Dullemond, C. P. 2005, A&A, 436, 209

Adams, F. C., Lada, C. J., & Shu, F. H. 1987, ApJ, 312, 788

Alencar, S. H. P., Basri, G., Hartmann, L., & Calvet, N. 2005, A&A, 440, 595

Allen, L. E., et al. 2004, ApJS, 154, 363

Andre, P., & Montmerle, T. 1994, ApJ, 420, 837

Andreani, P., & Wilson, T. 2006, The Messenger, 123, 59

Balog, Z., Muzerolle, J., Rieke, G. H., Su, K. Y. L., Young, E. T., & Megeath, S. T. 2007, ApJ, 660, 1532

Balona, L. A., Koen, C., & van Wyk, F. 2002, MNRAS, 333, 923

Barnard, E. E. 1919, ApJ, 49, 1

Beltrán, M. T., Girart, J. M., Estalella, R., & Ho, P. T. P. 2004, A&A, 426, 941

Beltrán, M. T., Girart, J. M., Estalella, R., Ho, P. T. P., & Palau, A. 2002, ApJ, 573, 246

Beltrán, M. T., Massi, F., López, R., Girart, J. M., & Estalella, R. 2009, A&A, 504, 97

Bertoldi, F. 1989, ApJ, 346, 735

Bertoldi, F., & McKee, C. F. 1990, ApJ, 354, 529

Bessell, M. S., & Brett, J. M. 1988, PASP, 100, 1134

Beuther, H., Churchwell, E. B., McKee, C. F., & Tan, J. C. 2007, Protostars and Planets V, 165

Bhatt, H. C., & Gorti, U. 1993, Bulletin of the Astronomical Society of India, 21, 541

Blitz, L. 1993, in Protostars and Planets III, ed. E. H. Levy & J. I. Lunine, 125–161

Bok, B. J., & Reilly, E. F. 1947, ApJ, 105, 255

Brand, P. W. J. L., Hawarden, T. G., Longmore, A. J., Williams, P. M., & Caldwell, J. A. R. 1983, MNRAS, 203, 215

Caratti o Garatti, A., Giannini, T., Nisini, B., & Lorenzetti, D. 2006, A&A, 449, 1077

Carpenter, J. M. 2001, AJ, 121, 2851

Chanot, A., & Sivan, J. P. 1983, A&A, 121, 19

Codella, C., Bachiller, R., Nisini, B., Saraceno, P., & Testi, L. 2001, A&A, 376, 271

Contreras, M. E., Sicilia-Aguilar, A., Muzerolle, J., Calvet, N., Berlind, P., & Hartmann, L. 2002, AJ, 124, 1585

Cutri, R. M., et al. 2003, 2MASS All Sky Catalog of point sources. (NASA/IPAC Infrared Science Archive.)

de Winter, D., Grady, C. A., van den Ancker, M. E., Pérez, M. R., & Eiroa, C. 1999, A&A, 343, 137

de Zeeuw, P. T., Hoogerwerf, R., de Bruijne, J. H. J., Brown, A. G. A., & Blaauw, A. 1999, AJ, 117, 354

Deharveng, L., Lefloch, B., Zavagno, A., Caplan, J., Whitworth, A. P., Nadeau, D., & Martín, S. 2003, A&A, 408, L25

Deharveng, L., Zavagno, A., Schuller, F., Caplan, J., Pomarès, M., & De Breuck, C. 2009, A&A, 496, 177

Desai, K. M., et al. 2010, AJ, 140, 584

Ducourant, C., Teixeira, R., Périé, J. P., Lecampion, J. F., Guibert, J., & Sartori, M. J. 2005, A&A, 438, 769

Dunkin, S. K., Barlow, M. J., & Ryan, S. G. 1997, MNRAS, 286, 604

Edwards, S., Fischer, W., Kwan, J., Hillenbrand, L., & Dupree, A. K. 2003, ApJ, 599, L41

Eiroa, C., et al. 2001, A&A, 365, 110

—. 2002, A&A, 384, 1038

Elmegreen, B. G., & Lada, C. J. 1977, ApJ, 214, 725

Elmergreen, B. G. 1976, ApJ, 205, 405

Fang, M., van Boekel, R., Wang, W., Carmona, A., Sicilia-Aguilar, A., & Henning, T. 2009, A&A, 504, 461

G. Helou & D. W. Walker, ed. 1988, Infrared astronomical satellite (IRAS) catalogs and atlases. Volume 7: The small scale structure catalog, Vol. 7

Getman, K. V., Feigelson, E. D., Garmire, G., Broos, P., & Wang, J. 2007, ApJ, 654, 316

Gorti, U., & Bhatt, H. C. 1996, MNRAS, 278, 611

Grady, C. A., et al. 1996, A&AS, 120, 157

Gray, R. O., & Corbally, J. C. 2009, Stellar Spectral Classification (Princeton University Press)

Grinin, V. P., Kozlova, O. V., Natta, A., Ilyin, I., Tuominen, I., Rostopchina, A. N., & Shakhovskoy, D. N. 2001, A&A, 379, 482

Grinin, V. P., The, P. S., de Winter, D., Giampapa, M., Rostopchina, A. N., Tambovtseva, L. V., & van den Ancker, M. E. 1994, A&A, 292, 165

Guimarães, M. M., Alencar, S. H. P., Corradi, W. J. B., & Vieira, S. L. A. 2006, A&A, 457, 581

Gum, C. S. 1952, The Observatory, 72, 151

Gutermuth, R. A., Megeath, S. T., Myers, P. C., Allen, L. E., Pipher, J. L., & Fazio, G. G. 2009, ApJS, 184, 18

Hamann, F. 1994, ApJS, 93, 485

Hamann, F., & Persson, S. E. 1992, ApJS, 82, 285

Hartigan, P., Edwards, S., & Ghandour, L. 1995, ApJ, 452, 736

Hartmann, L. 2009, Accretion Processes in Star Formation: Second Edition (Cambridge University Press)

Hartmann, L., Hewett, R., & Calvet, N. 1994, ApJ, 426, 669

Hartmann, L., Megeath, S. T., Allen, L., Luhman, K., Calvet, N., D'Alessio, P., Franco-Hernandez, R., & Fazio, G. 2005, ApJ, 629, 881

Hernández, J., Calvet, N., Briceño, C., Hartmann, L., & Berlind, P. 2004, AJ, 127, 1682

Hernández, J., Calvet, N., Hartmann, L., Briceño, C., Sicilia-Aguilar, A., & Berlind, P. 2005, AJ, 129, 856

Hernández, J., Calvet, N., Hartmann, L., Muzerolle, J., Gutermuth, R., & Stauffer, J. 2009, ApJ, 707, 705

Hernández, J., Hartmann, L., Calvet, N., Jeffries, R. D., Gutermuth, R., Muzerolle, J., & Stauffer, J. 2008, ApJ, 686, 1195

Hester, J. J., & Desch, S. J. 2005, in Astronomical Society of the Pacific Conference Series, Vol. 341, Chondrites and the Protoplanetary Disk, ed. A. N. Krot, E. R. D. Scott, & B. Reipurth, 107–+

Hildebrand, R. H. 1983, QJRAS, 24, 267

Hillenbrand, L. A., Bauermeister, A., & White, R. J. 2008, in Astronomical Society of the Pacific Conference Series, Vol. 384, 14th Cambridge Workshop on Cool Stars, Stellar Systems, and the Sun, ed. G. van Belle, 200

Hillenbrand, L. A., Strom, S. E., Vrba, F. J., & Keene, J. 1992, ApJ, 397, 613

Høg, E., et al. 2000, A&A, 355, L27

Hosokawa, T., & Inutsuka, S. 2006, ApJ, 648, L131

Hubeny, I., & Lanz, T. 2000, Synspec User's Guides, Version 43, http://nova.astro.umd.edu/Tlusty2002/pdf/syn43guide.pdf

Ikeda, H., et al. 2008, AJ, 135, 2323

Indebetouw, R., et al. 2005, ApJ, 619, 931

Jacoby, G. H., Hunter, D. A., & Christian, C. A. 1984, ApJS, 56, 257

Jaschek, M., & Egret, D. 1982, in IAU Symposium, Vol. 98, Be Stars, ed. M. Jaschek & H.-G. Groth, 261

Johns, C. M., & Basri, G. 1995, AJ, 109, 2800

Jørgensen, J. K., Johnstone, D., Kirk, H., & Myers, P. C. 2007, ApJ, 656, 293

Joy, A. H. 1945, ApJ, 102, 168

Kenyon, S. J., & Hartmann, L. 1995, ApJS, 101, 117

Kim, J. S., Walter, F. M., & Wolk, S. J. 2005, AJ, 129, 1564

Kirkpatrick, J. D., Henry, T. J., & McCarthy, J. D. W. 1991, ApJS, 77, 417

Klein, R. I., Sandford, II, M. T., & Whitaker, R. W. 1980, Space Sci. Rev., 27, 275

Koenigl, A. 1991, ApJ, 370, L39

Kun, M., Kiss, Z. T., & Balog, Z. 2008, Star Forming Regions in Cepheus (Astronomical Society of the Pacific Monograph Publications), 136–+

Kurosawa, R., Harries, T. J., & Symington, N. H. 2006, MNRAS, 370, 580

Landolt, A. U. 1992, AJ, 104, 340

Lee, H., Chen, W. P., Zhang, Z., & Hu, J. 2005, ApJ, 624, 808

Lefloch, B., & Lazareff, B. 1994, A&A, 289, 559

Maheswar, G., Manoj, P., & Bhatt, H. C. 2002, A&A, 387, 1003

Mannings, V., & Sargent, A. I. 1997, ApJ, 490, 792

Manoj, P., Bhatt, H. C., Maheswar, G., & Muneer, S. 2006, ApJ, 653, 657

Marconi, M., Ripepi, V., Alcalá, J. M., Covino, E., Palla, F., & Terranegra, L. 2000, A&A, 355, L35

Matthews, H. I. 1979, A&A, 75, 345

McKee, C. F., & Ostriker, J. P. 1977, ApJ, 218, 148

Mdzinarishvili, T. G., & Chargeishvili, K. B. 2005, A&A, 431, L1

Megeath, S. T., et al. 2004, ApJS, 154, 367

Mercer, E. P., Miller, J. M., Calvet, N., Hartmann, L., Hernandez, J., Sicilia-Aguilar, A., & Gutermuth, R. 2009, AJ, 138, 7

Meyer, M. R., Calvet, N., & Hillenbrand, L. A. 1997, AJ, 114, 288

Miao, J., White, G. J., Nelson, R., Thompson, M., & Morgan, L. 2006, MNRAS, 369, 143

Miao, J., White, G. J., Thompson, M. A., & Nelson, R. P. 2009, ApJ, 692, 382

Monnier, J. D., & Millan-Gabet, R. 2002, ApJ, 579, 694

Montesinos, B., Eiroa, C., Mora, A., & Merín, B. 2009, A&A, 495, 901

Mookerjea, B., Sandell, G., Jarrett, T. H., & McMullin, J. P. 2009, A&A, 507, 1485

Mora, A., et al. 2002, A&A, 393, 259

—. 2004, A&A, 419, 225

Morgan, L. K., Thompson, M. A., Urquhart, J. S., & White, G. J. 2008, A&A, 477, 557

Muzerolle, J., Calvet, N., & Hartmann, L. 1998a, ApJ, 492, 743

—. 2001, ApJ, 550, 944

Muzerolle, J., D'Alessio, P., Calvet, N., & Hartmann, L. 2004a, ApJ, 617, 406

Muzerolle, J., Hartmann, L., & Calvet, N. 1998b, AJ, 116, 455

Muzerolle, J., et al. 2004b, ApJS, 154, 379

Natta, A., Grinin, V. P., & Tambovtseva, L. V. 2000, ApJ, 542, 421

Natta, A., Testi, L., Muzerolle, J., Randich, S., Comerón, F., & Persi, P. 2004, A&A, 424, 603

Neri, R., et al. 2007, A&A, 468, L33

Nisini, B., et al. 2001, A&A, 376, 553

Ogura, K., Sugitani, K., & Pickles, A. 2002, AJ, 123, 2597

Oort, J. H., & Spitzer, L. J. 1955, ApJ, 121, 6

Otrupcek, R. E., Hartley, M., & Wang, J. 2000, Publications of the Astronomical Society of Australia, 17, 92

Oudmaijer, R. D., et al. 2001, A&A, 379, 564

Patel, N. A., Goldsmith, P. F., Heyer, M. H., Snell, R. L., & Pratap, P. 1998, ApJ, 507, 241

Patel, N. A., Goldsmith, P. F., Snell, R. L., Hezel, T., & Xie, T. 1995, ApJ, 447, 721

Pettersson, B. 1987, A&A, 171, 101

Pozzo, M., Jeffries, R. D., Naylor, T., Totten, E. J., Harmer, S., & Kenyon, M. 2000, MNRAS, 313, L23

Rao, N. K., Sriram, S., Jayakumar, K., & Gabriel, F. 2005, JApA, 26, 331

Reipurth, B. 1983, A&A, 117, 183

—. 2000, AJ, 120, 3177

Reipurth, B., Armond, T., Raga, A., & Bally, J. 2003, ApJ, 593, L47

Reipurth, B., Pedrosa, A., & Lago, M. T. V. T. 1996, A&AS, 120, 229

Reipurth, B., & Pettersson, B. 1993, A&A, 267, 439

Rieke, G. H., & Lebofsky, M. J. 1985, ApJ, 288, 618

Ripepi, V., et al. 2003, A&A, 408, 1047

Robitaille, T. P., Whitney, B. A., Indebetouw, R., & Wood, K. 2007, ApJS, 169, 328

Robitaille, T. P., Whitney, B. A., Indebetouw, R., Wood, K., & Denzmore, P. 2006, ApJS, 167, 256

Sahu, M., & Sahu, K. C. 1992, A&A, 259, 265

Saraceno, P., et al. 1996, A&A, 315, L293

Shu, F. H., Adams, F. C., & Lizano, S. 1987, ARA&A, 25, 23

Siess, L., Dufour, E., & Forestini, M. 2000, A&A, 358, 593

Spitzer, L. 1948, Physics Today, 1, 6

Sridharan, T. K. 1992, Journal of Astrophysics and Astronomy, 13, 217

Stern, D., et al. 2005, ApJ, 631, 163

Sternberg, A., Hoffmann, T. L., & Pauldrach, A. W. A. 2003, ApJ, 599, 1333

Sterzik, M. F., & Durisen, R. H. 1995, A&A, 304, L9+

Stickland, D. J. 1995, The Observatory, 115, 180

Sugitani, K., Fukui, Y., Mizuni, A., & Ohashi, N. 1989, ApJ, 342, L87

Sugitani, K., Fukui, Y., & Ogura, K. 1991, ApJS, 77, 59

Sugitani, K., Matsuo, H., Nakano, M., Tamura, M., & Ogura, K. 2000, AJ, 119, 323

Sugitani, K., & Ogura, K. 1994, ApJS, 92, 163

Sugitani, K., Tamura, M., & Ogura, K. 1999, in Star Formation 1999, Proceedings of Star Formation 1999, held in Nagoya, Japan, June 21 - 25, 1999, Editor: T. Nakamoto, Nobeyama Radio Observatory, p. 358-364, ed. T. Nakamoto, 358–364

Sugitani, K., et al. 2002, in 8th Asian-Pacific Regional Meeting, Volume II, ed. S. Ikeuchi, J. Hearnshaw, & T. Hanawa, 213–214

Tapia, M. 1981, MNRAS, 197, 949

Valdes, F., Gupta, R., Rose, J. A., Singh, H. P., & Bell, D. J. 2004, ApJS, 152, 251

Valdettaro, R., Palla, F., Brand, J., & Cesaroni, R. 2005, A&A, 443, 535

van den Ancker, M. E., The, P. S., & de Winter, D. 1996, A&A, 309, 809

van der Hucht, K. A., et al. 1997, New Astronomy, 2, 245

van Leeuwen, F. 2007, A&A, 474, 653

Vieira, S. L. A., Corradi, W. J. B., Alencar, S. H. P., Mendes, L. T. S., Torres, C. A. O., Quast, G. R., Guimarães, M. M., & da Silva, L. 2003, AJ, 126, 2971

Waller, W. H. 1990, PASP, 102, 1217

Werner, M. W., et al. 2004, ApJS, 154, 1

Whipple, F. L. 1946, ApJ, 104, 1

White, R. J., & Basri, G. 2003, ApJ, 582, 1109

Witham, A. R., Knigge, C., Drew, J. E., Greimel, R., Steeghs, D., Gänsicke, B. T., Groot, P. J., & Mampaso, A. 2008, MNRAS, 384, 1277

Woermann, B., Gaylard, M. J., & Otrupcek, R. 2001, MNRAS, 325, 1213

Yamaguchi, N., Mizuno, N., Moriguchi, Y., Yonekura, Y., Mizuno, A., & Fukui, Y. 1999, PASJ, 51, 765

Young, J. S., Xie, S., Kenney, J. D. P., & Rice, W. L. 1989, ApJS, 70, 699

Zacharias, N., Monet, D. G., Levine, S. E., Urban, S. E., Gaume, R., & Wycoff, G. L. 2004, in Bulletin of the American Astronomical Society, Vol. 36, Bulletin of the American Astronomical Society, 1418–+

Zavagno, A., Deharveng, L., Comerón, F., Brand, J., Massi, F., Caplan, J., & Russeil, D. 2006, A&A, 446, 171

Zavagno, A., Pomarès, M., Deharveng, L., Hosokawa, T., Russeil, D., & Caplan, J. 2007, A&A, 472, 835

Zealey, W. J., Ninkov, Z., Rice, E., Hartley, M., & Tritton, S. B. 1983, Astrophys. Lett., 23, 119

Zinnecker, H., & Yorke, H. W. 2007, ARA&A, 45, 481